

UCLA

UCLA Electronic Theses and Dissertations

Title

Machine Learning-enabled Electrical Impedance Tomography for Single-cell Imaging

Permalink

<https://escholarship.org/uc/item/6j67t4tf>

Author

Akhazhanov, Ablaihan

Publication Date

2020

Peer reviewed|Thesis/dissertation

UNIVERSITY OF CALIFORNIA
Los Angeles

Machine Learning-enabled Electrical Impedance Tomography for Single-cell Imaging

A dissertation submitted in partial satisfaction
of the requirements for the degree
Doctor of Philosophy in Electrical and Computer Engineering

by

Ablaikhan Akhazhanov

2020

© Copyright by
Ablaikhan Akhazhanov
2020

ABSTRACT OF THE DISSERTATION

Machine Learning-enabled Electrical Impedance Tomography for Single-cell Imaging

by

Ablaikhan Akhazhanov

Doctor of Philosophy in Electrical and Computer Engineering

University of California, Los Angeles, 2020

Professor Wentai Liu, Co-Chair

Professor Chi On Chui, Co-Chair

A biological cell is the elementary unit of life. Despite being actively studied for the last three centuries, many details of how cells are organized remain mysterious. One of the reasons in conventionally accepted optical microscopy that imposes high costs on experimental studies, limits scalability, and slows down the progress. In order to address this, numerous label-free imaging techniques were proposed by the biomedical engineering community. Among them is electrical impedance tomography (EIT), a low-cost and label-free imaging method based on electrical stimulations. Mathematically, EIT is ill-posed which severely limits its applications. Moreover, it was initially developed for human thorax imaging and its micro-scale version is yet to be established. In this dissertation, we shrink EIT for single-cell applications and demonstrate how to image a cell and its interior organelles using only a few microelectrodes.

We start by studying electrical properties of cells and build a scalable model of cellular electrical response. The proposed method mimics biodiversity among four common cell types and accurately represents complex three-dimensional geometries. By combining it with modern shape optimization methods and a customized microelectrode array we extend EIT to single-cell imaging. Along the way, we provide solutions to several well-known EIT problems such as low contrast images and numerical instability. To further expand cellular EIT to nucleus imaging we take a data-driven approach. We explore a variety of machine

learning methods previously applied to inverse imaging problems and discuss their pros and cons. We then propose a novel deep learning model specifically adjusted for EIT. Finally, we evaluate and experimentally demonstrate live cell nucleus imaging, driven by pure electrical excitations and the proposed deep neural network.

The dissertation of Ablaihan Akhazhanov is approved.

Chad Hazlett

Xiaochun Li

Yuanxun Wang

Chi On Chui, Committee Co-Chair

Wentai Liu, Committee Co-Chair

University of California, Los Angeles

2020

To my parents

TABLE OF CONTENTS

1	Introduction	1
1.1	Non-invasive electrical methods	3
1.2	Electrical response of biological cells	7
1.3	Deep learning-based EIT	9
1.4	Outline of this work	11
2	Diversity in cellular response to electrical stimulations	14
2.1	Electrical properties of biological cells	15
2.1.1	Cell membrane	17
2.1.2	Cytoplasm	18
2.1.3	Cell nucleus	18
2.1.4	Culture medium	20
2.1.5	Dielectric dispersion	20
2.2	Numerical simulations	23
2.2.1	Cell geometry	24
2.2.2	Electrodes-solution interface	26
2.2.3	Importance of cell geometry	29
2.3	Adherent cell simulations	34
2.4	Results and discussion	37
2.4.1	Electrical properties of cells	37
2.4.2	Electrical impedance spectroscopy of HeLa cell line	38
3	Electrical impedance tomography	39
3.1	EIT problem statement	42

3.2	Image reconstruction	46
3.3	Applications	49
4	Cell imaging with electrical impedance tomography	51
4.1	Problem statement	53
4.2	Image reconstruction	55
4.2.1	<i>A priori</i> electrical cellular properties	56
4.2.2	Maximum <i>a posteriori</i> estimation	56
4.2.3	Shape optimization	57
4.2.4	Cellular EIT reconstruction	58
4.2.5	Complex admittivity	59
4.2.6	Equally-spaced microelectrode array	60
4.3	Numerical evaluation	61
4.3.1	Evaluation of the proposed MEA design	61
4.3.2	Simulated cellular impedance tomography	61
4.4	Experimental verification	67
4.4.1	Single-cell imaging of HeLa cell line	68
4.4.2	Discussion	74
5	Deep learning in inverse problems	75
5.1	The elements of deep learning	75
5.1.1	Core building blocks	76
5.1.2	Importance of network architecture	79
5.1.3	Geometrical neural networks	83
5.2	Inverse problems	85
5.2.1	Deep prior	86

5.2.2	Deep approximation	87
5.2.3	Deep representation	90
6	Machine learning-enabled cellular impedance tomography	92
6.1	Training and model selection	93
6.1.1	ENINet architecture	97
6.2	Numerical results	100
6.3	Experimental results	104
6.3.1	Imaging cell nucleus	104
6.3.2	Early detection of cancer drug response	108
7	Concluding remarks	113
7.1	Electrical properties of biological cells	113
7.2	Cellular imaging using a few electrodes	114
7.3	Future directions	115
	References	117

LIST OF FIGURES

1.1	A live cell microscope. Live cell microscopes are generally inverted. To keep cells alive during observation, the microscopes are commonly enclosed in a micro cell incubator (the transparent box).	2
1.2	ECIS measurement system. The green lines represent cells attached to an active electrode, blue dashed curves show low-frequency current flow and red dashed curves show high-frequency current flow. The drawings are not to scale.	5
1.3	Single-cell EIT measurement system. The red node represents electrical current stimulations, the blue nodes are sequential voltage measurements. The drawing is not to scale.	6
1.4	Internal structure of eukaryotic cell. The drawing is not to scale.	8
1.5	Machine leaning-enabled EIT: non-invasive electrical measurements are mapped to the reconstructed image using a deep neural network	11
2.1	Electrical properties by cell type: adherent cells, non-adherent (suspended) cells, yeast cells, bacteria and other (tissues and membranes). Data was collected from the previously reported works [1, 2, 3, 4, 5, 6, 7, 8, 9, 10, 11, 12, 13, 14, 15, 16, 17, 18, 19, 20, 21, 22, 23, 24, 25, 26, 27, 28, 29]	19
2.2	Pseudocode for cell geometry generation	26
2.3	Pseudocode of optimization subroutine used in cell geometry generation	27
2.4	Examples of the cell geometries: (A) isotropic spreading, (B-C) anisotropic spreading, (D) assembly of cells, (E) cell structure schematic, (F) finite-element mesh	27
2.5	Electrical Double Layer (EDL): (A) physical structure and (B) its lumped-element model	28

2.6	Top view and side view of a BON cell. (A-B) Experimental 3D reconstruction generated by serial sectioning TEM and segmentation of the cell outline (brown) and (C-D) its smooth approximation. The experimental 3D reconstruction is based on data from Villinger C. et al. (2014) Three-dimensional imaging of adherent cells using FIB/SEM and STEM. In: Kuo J. (eds) Electron Microscopy. Methods in Molecular Biology (Methods and Protocols), vol 1117. Humana Press, Totowa, NJ. Copyright Springer Science+Business Media, New York 2014. The data was provided by authors of the study[30]	30
2.7	Level of detail in cell geometries: (A) 3D view, (B) top view, and (C) cross section of a human lung cancer cell at different levels of detail (1 - highest (realistic), 2 - moderate (proposed), 3 - lowest (naive)); (C) cross sections include schematic sketches of the active electrode placement underneath the cell	32
2.8	Testing fidelity of the cell geometries against (A) varying electrode size and (B-C) electrode displacement	33
2.9	Electric current flow: underneath (A) proposed cell geometry and (B) naive cell geometry as well as the cross-sections (C) and (D) at the edges of the proposed geometry shown by the dashed lines	33
2.10	Experimental verification of the model with EIS measurements and FEM simulations of a HeLa cell on 8-electrode array	35
2.11	Translation of the fluorescent microscopy image into finite-element mesh	36
2.12	Electrical impedance spectroscopy of a single HeLa cell and FEM simulations	38
3.1	Steps in EIT image reconstruction: data collection with electrical measurements and mapping from voltage measurements to an image	40
3.2	A solution to the forward problem based on FEM: admittivity distribution, space discretization using finite elements of adaptive size, response due to an excitation	44
3.3	An illustration of how non-linear, linear, and regularized non-linear methods differ in a simplest case of fitting a function based on noisy samples	47

4.1	Electrical Impedance Tomography: forward and inverse problems	53
4.2	Sample of the MEA evaluation scheme: (A) simulated single cell (outlined with green) placed on equally-spaced 8- and 12-electrode MEAs (blue) and equivalent circular MEAs (red); (B) the corresponding reconstruction results	62
4.3	Evaluation of the proposed reconstruction algorithm on simulated data: (A) data generation and performance estimation; (B) reconstruction metrics at individual frequencies	65
4.4	Diagrams of (A) the measurements system and (B) experimental methodology .	70
4.5	Cellular EIT of HeLa cells compared against fluorescently labeled cell membrane: (A) partial coverage, (B) almost complete coverage, and (C) gold MEA	71
5.1	Feed-forward neural network	76
5.2	Convolutional neural network	78
5.3	Famous computer vision building blocks: (A) inception block, (B) residual block, (C) dense block, and (D) U-Net	80
5.4	Data representation and generative modeling: (A) autoencoder and (B) generative adversarial network (GAN)	82
5.5	Example of a forward and the corresponding inverse problems: image distortion (F) and image restoration (F^{-1})	85
5.6	Deep prior approach	87
5.7	Deep approximation approach	88
5.8	An invertible neural network built using affine coupling layer: (A) forward pass and (B) inverse pass	89
5.9	Deep representation approach	90
6.1	Examples of 3D cell geometries used in training dataset generation	94
6.2	2D mesh convolution with a few possible kernel window sizes (kw). Arrows represent sliding directions for a regular triangular mesh (shown in pink)	98

6.3	ENINet: super-resolution building block	99
6.4	ENINet hybrid training approach: (A) growing network architecture and (B) corresponding mesh for 12-MEA, and (C) training on multi-frequency measurements data	101
6.5	Electrically-driven imaging of cell nucleus on four samples shown in A-D. We used 8-MEA device with pitch of $11 \mu m$ (schematic arrangement is shown in the first column). To verify the reconstruction results we stained nucleus (shown in red) and membrane (shown in green). The white box represents the MEA area (field of view of the device). The third column shows an overlay of the nucleus reconstruction (ML-EIT) on top of the fluorescent images. The last three columns are the reconstructed images of the cell nucleus $\Phi(x)$. The red color represents area when the reconstruction algorithm predicts cell nucleus with greater confidence, while the blue regions are likely to have no nucleus	106
6.6	Detecting early effect of chemotherapy treatment with ML-EIT: (A) ENINet reconstruction of nuclei of a sample treated with $0.3 \mu g/mL$ of Doxorubicin; (B) fluorescent microscopy images of cells treated with $0.3 \mu g/mL$ of Doxorubicin; (C) relative changes in cell count (fluorescent microscopy) and nucleus size (ML-EIT) during the experiment; (D) relative changes in cell count compared to the baseline (control group) and nucleus size (ML-EIT). As a measure of relative cell nucleus change we used average number of visible cell nuclei on fluorescent images shown in (B) and the area of the red regions ($\Phi(x) > 0.5$) on the ML-EIT reconstructed images shown in (A)	110

LIST OF TABLES

2.1	Electrical properties of cell components	21
2.2	Dielectric dispersion parameters estimation	23
2.3	Computational complexity associated with levels of detail of cell geometry	34
4.1	Image reconstruction error (mean \pm std) for different MEA arrangements	62
4.2	Electrical properties of cell components used in the dataset generation	63
4.3	Image reconstruction error (mean \pm std) with 12 equally-spaced MEA and noiseless data	64
4.4	Image reconstruction error (mean \pm std) with 12 equally-spaced MEA and 20 <i>dB</i> data	66
6.1	Geometrical transformations used in dataset generation	95
6.2	Out-of-sample mean average ROC AUC of deep learning models	102

ACKNOWLEDGMENTS

I would like to thank my advisor, Professor Chi On Chui for supporting my every endeavor and patiently guiding me through the world of science and engineering. The lessons on conducting research and personal life that I learned from him influenced me the most. Besides providing all the resources and making sure I have everything I need, Professor Chui gave me a unique chance to explore different opportunities even loosely relevant to work, but within a broad spectrum of my interests. I am sincerely grateful to him for believing in me and catalyzing my growth. My brilliant committee members, Professors Wentai Liu, Ethan Wang, Xiaochun Li, and Chad Hazlett, gave me valuable and kind feedback. They offered help and genuinely supported me even beyond my research and professional activities. I truly appreciate the opportunity to work with all my committee members and hope to continue learning from them in the years to come.

This work would not be accomplished without my collaborators. Professor Huan Meng, Xiangsheng Liu, and Jianqin Lu of UC CEIN were instrumental in conducting biological experiments. Huan not only shared his expertise and wisdom, but truly supported my interest in biological studies and equipped me with a diverse set of necessary skills and tools. I am very grateful to the members of Professor Pei-Yu Chiou's Optofluidics Systems Laboratory and particularly to Tingyi Liu, who shared his world-class experience in building microfluidic systems and microfabrication, trained me on his marvelous cell manipulation system, and was always eager to share and help.

I feel lucky for working with my colleagues in Nanostructure Devices and Technology Laboratory. Senior members Andrew, Greg, Hyung Suk, Kaveh, and Yufei were always kind to me, but yet sincerely criticized and smashed up many of my ideas in the early stage, which eventually helped me to choose the right targets and plan ahead. I am particularly grateful to Andrew for mentorship that was exceptionally import to me. Our discussions, that sometimes evolved into long lectures, played a vital role in my research. Kaveh and Yufei taught me nuts and bolts of real-world engineering and Wuran and Xin never let me deal with problems alone and were always here to help. People outside the lab made this

journey fun and entertaining. I will never forget time spent with Alim, Luigi, Jeff, Mathew, Xiaoqiang, Muhammed, and many others. These moments honestly mean a lot to me.

I would also like to thank faculty and staff of ECE department for being excellent and making lives of graduate students fun and easy. I owe my teaching passion to Professor Mike Briggs and Professor Greg Pottie who were inspirational and granted the privilege to teach with them. Deeona, Mandy, Ryo, and Julio were somehow always able to accommodate my wild requests and navigated me through these six years. Although my studies were primarily funded by UCLA and NSF, I would not be able to make it without support from Assel Tasmagambetova and Kenes Rakishev, whose philanthropic projects truly change people's fates.

Finally, I would like to deeply thank my family. My mom, perhaps, did not dream about her son becoming an engineer, but her love, our open-hearted conversations, and her wisdom built my life-navigating system and kept me afloat. My dad will always be an example of courage, altruism, and integrity. His advise made me choose graduate school over other opportunities and I never regretted about it. I would not be able to make it without my sister, Akmaral, who spent so much time looking after me despite the continuous stream of my stupid jokes. My wife, Assel, waited for this work to be finished longer than myself and selflessly kept supporting me during the ups and downs in our lives.

VITA

- 2012 B.S. (Electrical Engineering), Almaty University of Power Engineering and Telecommunications, Kazakhstan.
- 2012 B.S. (Economics), Moscow Power Engineering Institute, Russia.
- 2012–2014 Quantitative Analyst, Kcell JSC, Kazakhstan
- 2015 M.S. (Electrical Engineering), UCLA.
- 2015–2017 Teaching Assistant, Electrical and Computer Engineering department, UCLA.
- 2018 M.S. (Statistics), UCLA.
- 2018 Research Intern, Visa Inc., Palo Alto, CA.
- 2014–present Graduate Student Researcher, NanoDTL, UCLA.
- 2017–present Teaching Fellow, Electrical and Computer Engineering department, UCLA.

CHAPTER 1

Introduction

Theories pass. The frog remains

Jean Rostand

Discovery of biological cells in XVII century caused a fundamental shift in the way we think about living beings. It brought to life cell biology and enabled us to engineer new drugs and therapies. The discovery was made possible through the continual improvements in magnification technologies. More than two thousands year ago, Romans started making glass and used it to look at small objects. Beginning from XII century, lenses in eyeglasses became a common tool in European nations. It took a few more centuries to combine an objective lens with an eyepiece into a compound microscope that was later used to observe specimen with cells for the first time. Nowadays, optical microscopes (also called light microscopes) remain dominant in a variety of biomedical applications. Combined with digital cameras, lasers, fluorescent dyes, and advanced lenses, microscopes became imperative to every laboratory space. The technological complexity and associated expenses of even basic microscopy analysis (see Figure 1.1) sometimes imposes additional challenges and significantly slows down research efforts.

Besides high maintenance and operation costs, optical microscopy has another drawback - it requires labeling. To image biological cells, one needs to stain them with fluorescent dyes - specifically engineered chemicals that emit light upon ultraviolet (UV) or infrared (IR) excitation. These molecules penetrate the cells, bind to a targeted organelle, and, when exposed, emit a light of a specific wavelength. To image the entire cell, one needs to use several collectively-compatible dyes, which may impose significant costs on empirical studies and makes nearly impossible *in vivo* experiments, long-term cell imaging, and assays

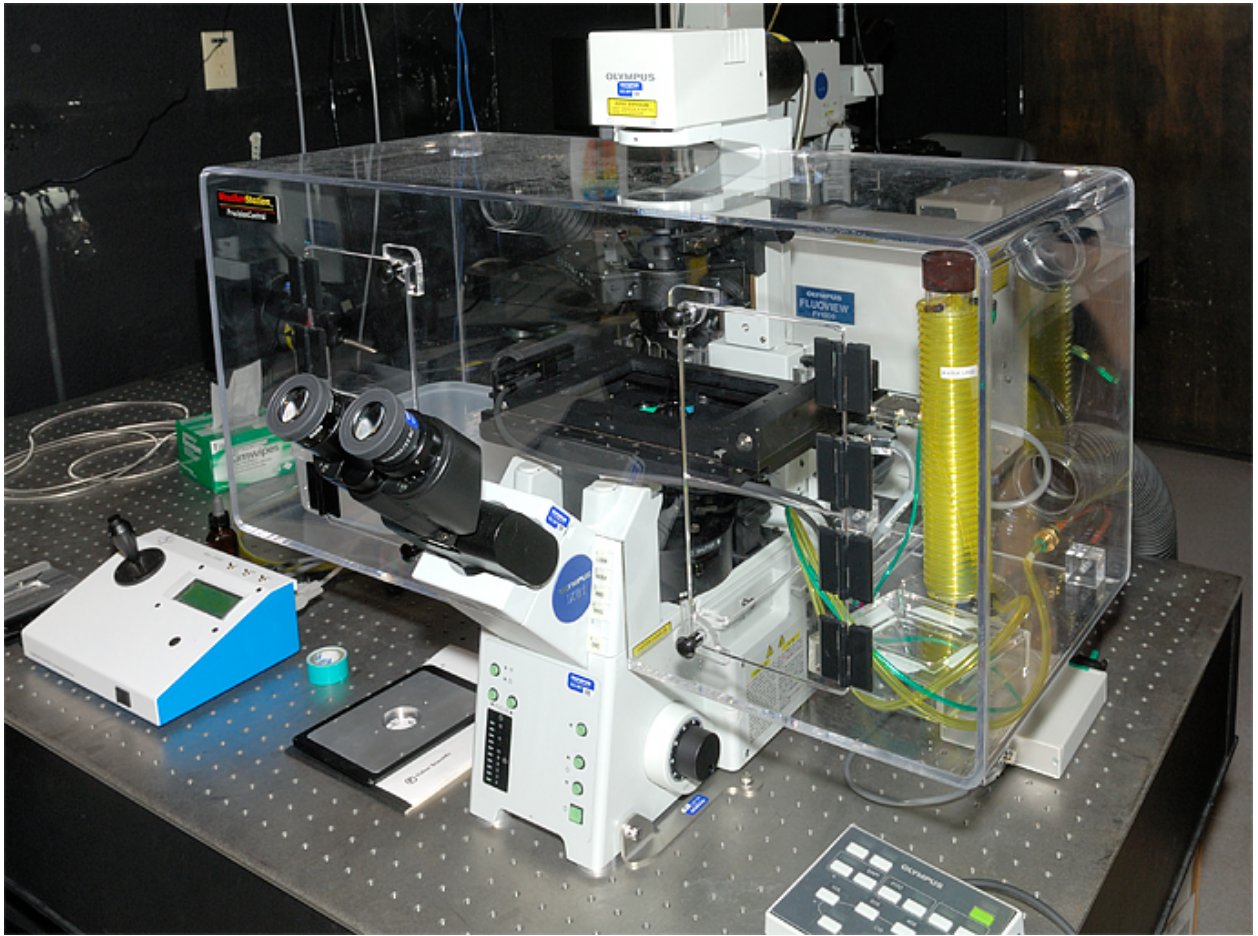


Figure 1.1: A live cell microscope. Live cell microscopes are generally inverted. To keep cells alive during observation, the microscopes are commonly enclosed in a micro cell incubator (the transparent box).

Photo credit: Jacopo Werther

(https://en.wikipedia.org/wiki/Live_cell_imaging#/media/File:Olympus_FluoView_FV1000_Confocal_Microscope_-_NCMIR.jpg). Licensed under CC BY-SA 3.0 (<https://creativecommons.org/licenses/by-sa/3.0>).

beyond the laboratory. Moreover, high-power UV and IR light can damage DNA, raise cellular temperatures, and cause other photo-toxic effects [31, 32], while fluorescent dyes are frequently cytotoxic and can interact with other chemicals affecting the experimental results [33, 34].

A number of advanced optical techniques have been developed including coherence tomography [35] and projection tomography [36], but they suffer from poor penetration depth, high cost, and are difficult to scale down to a cell level. Micro-scale magnetic resonance imaging (MRI), on the other hand, requires very strong permanent magnets or additional injection of potentially toxic particles into the cells [37]. As a result, long-term studies with live cells are hardly feasible with these conventional methods.

The emerging global viral disease episodes such as Coronavirus Disease 2019, Ebola, or Middle East respiratory syndrome, on the other hand, bring new challenges to cell biology and require more scalable, fast, and cheap cellular imaging techniques that can accelerate drug and vaccine development. Hence, invention of novel non-invasive cellular imaging techniques are of the utmost importance to biomedical and engineering communities.

1.1 Non-invasive electrical methods

Electrically-driven techniques is a promising direction that could bring a new realm of label-free imaging and sensing. Several methods based on electrical stimulations have been shown to be suitable for real-time and scalable cell studies. With a single pair of electrodes Giaver and Keese developed electrical cell-substrate impedance sensing (ECIS) [38], a robust *in vitro* technique based on changes in electrical impedance between the cells and the underlying electrode. Cellular behaviors that can be detected by ECIS include, but not limited to 1) cell adhesion, 2) micromotion, 3) mitosis, 4) spreading, and 5) drug response [39, 40]. In the past three decades, an incredible growth in the field of ECIS has not only resulted in a large amount of academic research, but also brought commercial companies such as Applied Biophysics and ACEA Biosciences. ECIS measurement system is sketched out in Figure 1.2. During the measurements, a small alternating current (AC) is applied across

the electrodes, which results in electric potential across the electrodes. As cells grow and cover the electrodes, the current is impeded proportionally to the number of cells covering the electrode, the morphology of the cells and the nature of the cell attachment. When cells get additional treatment, the accompanying changes in cell morphology alter the impedance. At relatively low frequencies (below 2 kHz), the measurements strongly respond to changes in the spaces either under or between the cells since most of the electric current flows there (blue dashed curves in Figure 1.2). At higher frequencies current easier penetrates the cells and the measurements are more affected by the cell coverage. By continuously monitoring the impedance, ECIS allows detection and quantification of morphology changes in the sub-nanometer to micrometer range. Although this method only gives a point estimate and falls behind optical imaging in applicability, it serves as a demonstration of the power behind electrical probing of the cell morphology.

With a few additional electrodes, a more sophisticated analysis can be done. Proposed by Webster [41] and practically realized by Barber and Brown [42], electrical impedance tomography (EIT) deals with the reconstruction of the spatial distribution of electrical admittivity or conductivity. Assuming that different biological materials can be identified and characterized by their electrical properties, EIT delivers high penetration imaging for medical and biological applications. In contrast to other tomographic imaging techniques, EIT does not employ hazardous ionizing radiation. Instead, it uses electric currents that are relatively small and do not cause significant nerve stimulation. The AC frequency of the applied stimulations is sufficiently high not to give rise to electrolytic effects in the body and is easily handled by the patient's body. Non-invasive properties, high mobility, and low cost make EIT systems particularly useful in intensive care.

In EIT the conducting electrodes are attached around the object being examined (e.g. human thorax or a tissue). A small AC current is applied between a chosen electrode pair that results in equi-potentials being recorded from the remaining electrodes (see Figure 1.3). This process is repeated for numerous different electrode pairs and finally results in a set of recorded voltages. The changes in conductivity due to presence of objects being examined causes bending of the equi-potential lines and encodes that in measured voltages. Finally, a

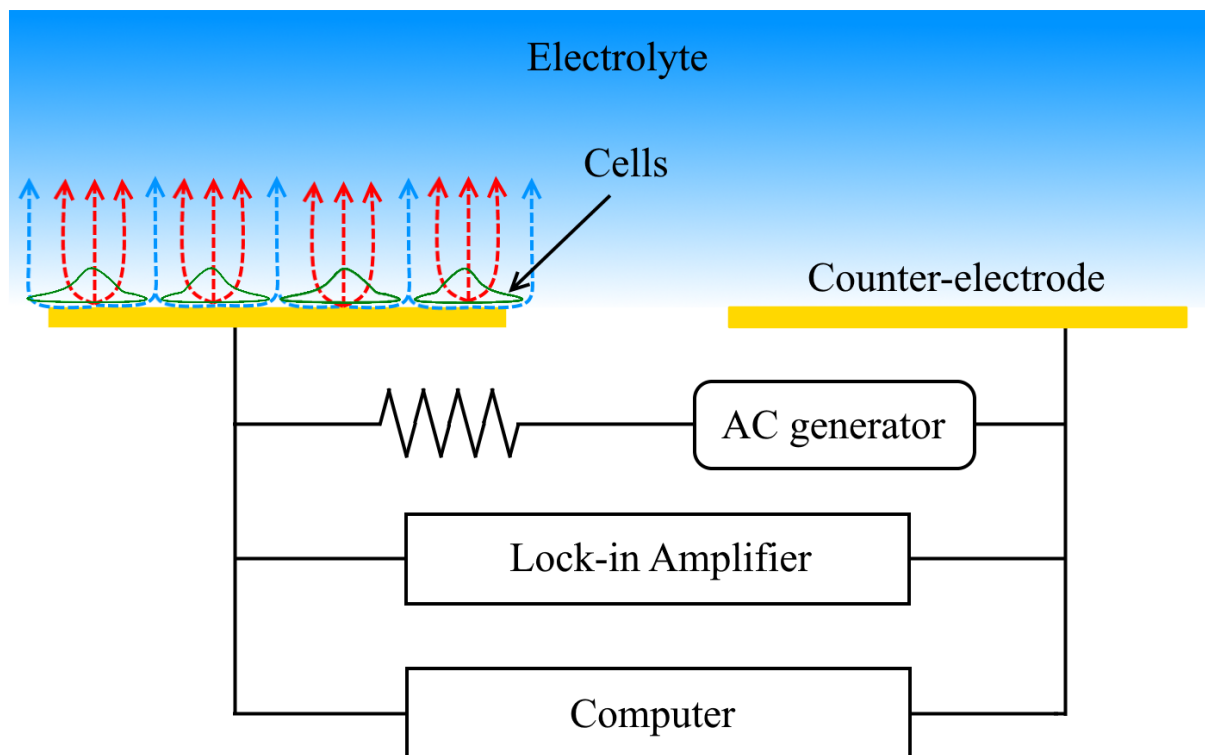


Figure 1.2: ECIS measurement system. The green lines represent cells attached to an active electrode, blue dashed curves show low-frequency current flow and red dashed curves show high-frequency current flow. The drawings are not to scale.

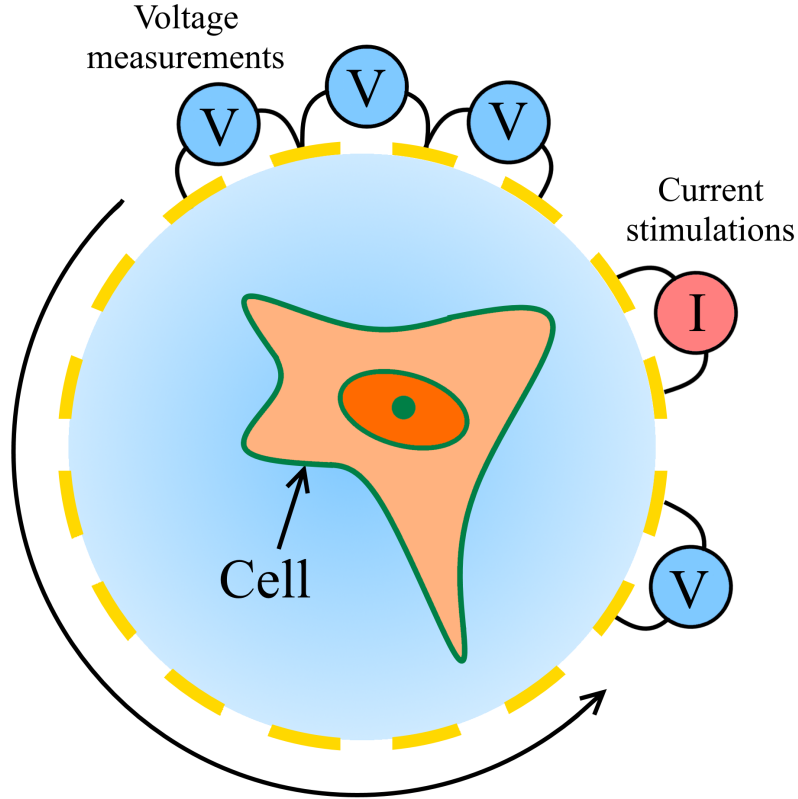


Figure 1.3: Single-cell EIT measurement system. The red node represents electrical current stimulations, the blue nodes are sequential voltage measurements. The drawing is not to scale.

two-dimensional (2D) tomogram is obtained using one or several reconstruction algorithms. Given that electrical properties of biological materials often have a strong dependency on frequency of the external electric field, multifrequency-EIT (MF-EIT) or electrical impedance spectroscopy (EIS) systems became popular in detecting or locating abnormal tissue such as precancerous lesions or cancer.

On the other hand, EIT has its own well-known problems. Being notoriously difficult, the image reconstruction remains the main bottleneck of the technology. Mathematically, it is severely ill-posed and requires additional simplifications that eventually deteriorate image resolution. From its inception researchers struggled with the development of reliable and inexpensive reconstruction algorithms. For instance, the commonly accepted approaches such

as backprojection method [43] and Gauss-Newton algorithm [44] fail to deliver high resolution and may suffer from undesirable artifacts in the images, despite strong assumptions such as linearity of the problem. Nonetheless, EIT attracts research interests and new developments in image reconstruction, measurements methodology, and applications are presented every year. Particularly intriguing is micro-scale EIT that was previously applied to *ex vivo* tissue electroporation imaging [45], cell culture imaging [46, 47], and even single cell studies [48, 49]. Further efforts led to three-dimensional (3D) and real-time cell imaging systems combined with microfluidic devices [50, 51]. Recently, electrically-driven cell imaging was also integrated with complementary metal-oxide-semiconductor (CMOS) technology [52, 53] demonstrating how it could be further scaled to a larger number of sensing electrodes and expand into lab-on-a-chip platform.

1.2 Electrical response of biological cells

Electrical properties of biological cells and tissues play a critical role in multiple sensing and imaging applications including ECIS, EIT, EIS, electroporation, dielectrophoretic (DEP) cell trapping and manipulation, cytometry, and electrical cell lysis. The key underlying foundation behind these techniques is an accurate model of electrical response of individual sub-cellular components, the entire cell, and multicellular systems. In a simple view, cell consists of cytoplasm enclosed by a thin membrane made of regular lipid bilayer with embedded proteins. Cytoplasm additionally contains membrane-bound organelles that are associated with specific living activities such as nucleus, mitochondria, ribosomes, and others (see Figure 1.4). The most conspicuous among these is cell nucleus, which houses almost all DNA replication and RNA synthesis. Nucleus is a sphere or ellipsoid containing viscous nucleoplasm enclosed within a porous nuclear envelope. Electrical properties of entire cell depend on the properties of each cell component.

The history of active experimental studies of electrical cellular response starts in 1960s with early efforts by Pauly *et al.* [54, 1], Loewenstein *et al.* [2], Carstensen *et al.* [55, 3] and Miyamoto *et al.* [4]. Numerous empirical and theoretical works were presented in subsequent

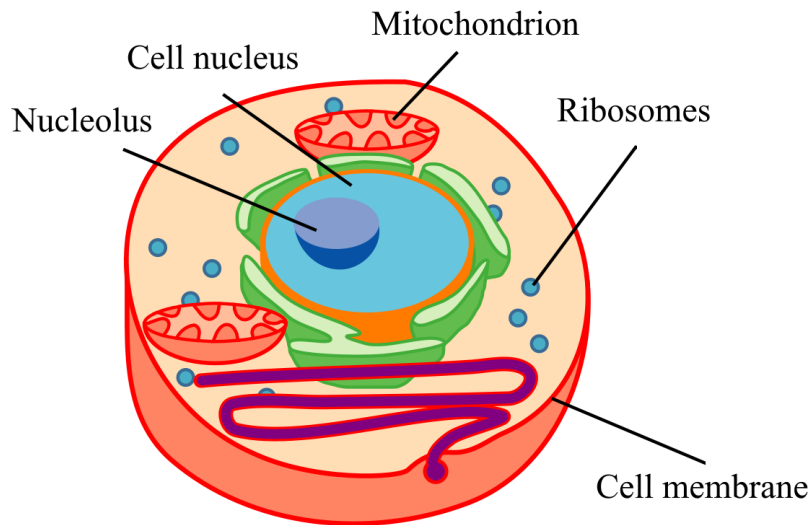


Figure 1.4: Internal structure of eukaryotic cell. The drawing is not to scale.

Adapted from Science Primer (National Center for Biotechnology Information, NIH)

years by Schwan, Asami, Pethig, Becker, Holzel, Gimsa, and many others [56, 6, 7, 12, 22, 24].

For many year the dominating method in electrical modelling of cells and tissues was the equivalent circuit model. Giaever and Keese approached modelling of a confluent layer of adherent cells with a lumped element circuit in their pioneering work on ECIS [38]. Their *et al.* described an equivalent circuit of an individual cell and the cell-electrode interface [57] revealing mechanisms behind electrical responses of a single cell and optimal parameters for the sensing applications. Gowrishankar and Weaver [58] introduced a sophisticated network of lumped elements called Cartesian transport lattice (CTL) that was inherently dependent on the cell geometry. Ren and Chui recently presented another 3D model of a cell in their work on the fundamental feasibility of tracking changes of multiple cellular properties [59]. The later work particularly demonstrated frequency response of different cell components and showed how they may be distinguished.

An alternative approach based on finite element method (FEM) was proposed by Huang *et al.* [60]. They reported a model that took into account frequency-dependent nature of the electrical properties of a single cell while trying to accurately depict the geometry of the at-

tached cell. Generally, the geometry of adherent cells can vary drastically. During life-cycle, adherent cells undergo significant shape deformations due to spreading, crawling, division and apoptosis. Deformations can involve simple electrostatic interactions and sophisticated protein polymerization mechanisms. Steady isotropic and stochastic anisotropic spreading dominate in many adherent cells. Cell membrane and cytoplasm experience stronger deformations compared to cell organelles, which leads to heterogeneous electrical properties throughout the cell body [61].

The most important property of a numerical model is its ability to describe and predict behaviour under diverse set of conditions. Driven by biological diversity fluctuations in electrical properties often cause discrepancies between real samples and naive deterministic models. A recent statistical study on diversity among animal cells, yeast cell and bacteria has shown that simple parametric models are well-suited for this problem [62]. Moreover, the study proposed a method for generation of realistic 3D geometries of adherent cells and their organelles that enabled precise modelling of individual cell components, whole cells, and small tissues. Stochastically modelled electrical properties and cell geometries serve as a great prior for EIT reconstruction problem. As was mentioned before, image reconstruction suffers from ill-posed conditions, but if supplied with a proper prior information, the problem becomes numerically stable and a lot easier. Finally, the model is well suited for generating a large training dataset and subsequent development of machine learning-based reconstruction algorithms. In fact, high quality data generation process is quintessential in data-driven methods.

1.3 Deep learning-based EIT

Machine learning and, particularly, deep learning is a great example of a data-driven approach. A typical deep learning model is based on an artificial neural network (ANN), a weighted directed graph whose nodes perform simple mathematical operations on their inputs. Relying on large amount of data, deep learning methods are often presented as vague black boxes that approximate a mathematical function of interest by fitting the dataset.

Particularly, due to lack of a comprehensive understanding of the learning dynamics, design choices are often driven by heuristics and intuition. The exact form of the ANN graph is, however, one of the major areas of research because it defines network capacity and directly affects results. It becomes clear when different ANN becomes particularly suitable for certain tasks.

Despite being an art, rather than science, deep learning is widely applied to a variety of numerical problems and demonstrates superior performance in medical imaging, natural language understanding, astronomy, finance, and many other fields, which is, at least, impressive. Recently, due to increased availability of scalable and reliable simulation methods, deep learning gained popularity in inverse problems [63, 64], a class of very difficult mathematical problems. Particularly promising are applications in image restoration and image reconstruction of biomedical data [65, 66, 67, 68].

Apparently, for a forward mapping $F : X \mapsto Y$ a deep ANN can be trained to help approximating the corresponding inverse mapping $F^{-1} : Y \mapsto X$. Known deep learning-based inverse solvers can be classified into deep approximation, deep prior, and deep representation. In deep approximation a model directly learns F^{-1} from the training dataset. Similarly, an invertible ANN can be trained to fit the forward mapping F and then its inverse can be used to approximate F^{-1} . Deep prior, on the other hand, does not solve the inverse problem of interest, but rather improves image reconstruction results by removing noise and artifacts. In that case, an ANN is trained on a custom dataset to learn *a priori* information, so that the model would be able to impose that prior on the reconstructed images. Deep representation models do not solve the inverse problem either, but extract semantic features from the data that can be used in subsequent analytical methods. Often, deep representation models are specifically trained to include information about the underlying analytical methods, while deep prior are completely decoupled from the image reconstruction.

Several machine learning-enabled EIT (ML-EIT) schemes were recently proposed. Most of the early works that used deep-learning methods for EIT took a naive end-to-end learning approach (see Figure 1.5), where a predefined artificial neural network is trained on a synthetic dataset generated using an underlying simulation model [69]. This approach is still

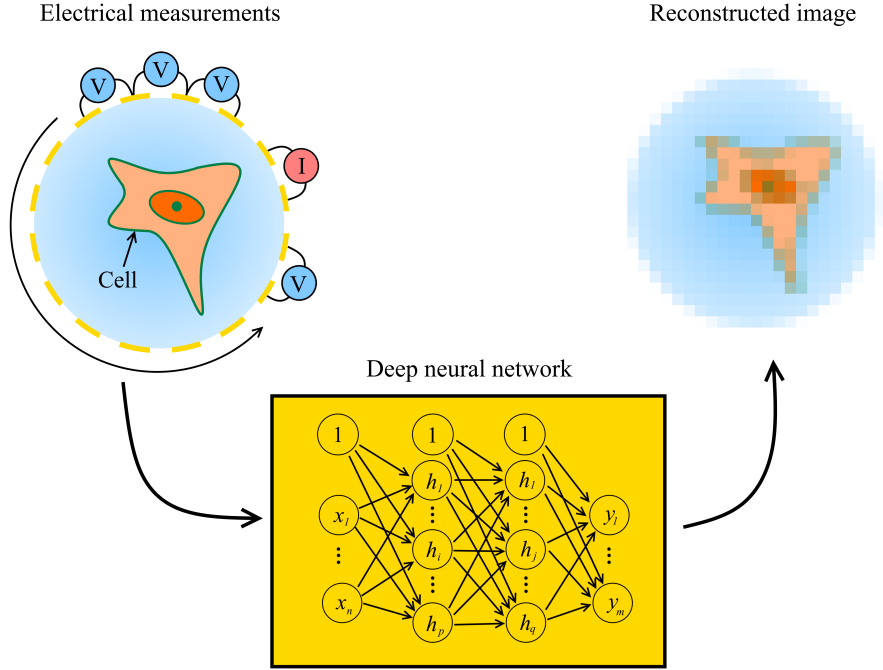


Figure 1.5: Machine learning-enabled EIT: non-invasive electrical measurements are mapped to the reconstructed image using a deep neural network

dominant in EIT, but more advanced neural architectures are proposed including ensemble of models [70], non-standard wavelet form of a neural network [71], and U-Net [72]. While ML-EIT demonstrated superior performance, the trade-offs of the blind end-to-end approach are yet to be discovered. Because EIT is a small niche with its own fundamental advantages and limitations we believe that a more elaborate analysis is necessary. For instance, prior knowledge on electrical response of biological cells could be embedded in the newly developed methodologies.

1.4 Outline of this work

Despite enormous growth of the field and ever increasing number of novel techniques, label-free cellular imaging still imposes significant limitations on researchers in biology and medicine. The topic of this dissertation addresses this challenge at the scale of a single cell. Driven by benign and simple electrical stimulations the proposed scheme for cellular electrical

impedance tomography targets non-invasive and scalable applications including drug development, cell phenotyping and motility, as well as studies on sub-cellular organelles. We hope to raise active interest among academic and industry communities that would promote diverse applications across biological and biomedical fields.

In Chapter 2 we question how biological cells respond to an external electric field. By collecting previously published experimental data and applying statistical analysis we show the importance of biological diversity and develop a precise numerical model. The purpose of the model is three-fold: 1) to explore the feasibility of probing the underlying structure of a single cell using AC electric stimulations, 2) to precisely model electrical cellular response and provide a reliable prior knowledge to electrically-driven techniques, and 3) to enable data-driven methods in cellular sensing, imaging, and manipulation.

General settings of electrical impedance tomography are discussed in Chapter 3. We particularly show the pros and cons of this electrically-driven non-invasive technique and discuss important steps towards single-cell applications. We take an ambitious task of cellular imaging and demonstrate how to improve the current paradigm by adopting the latest developments in image reconstruction and microelectrode fabrication in Chapter 4. It turned out that fascinating results can be achieved using pure electrical measurements and a few planar electrodes.

Stemming from statistics and inspired by biological neural networks, deep learning went through an explosive growth in the last two decades that eventually led to unprecedented advances in the field of artificial intelligence. Influenced by these developments, this work discusses modern deep learning methods in Chapter 5. Besides giving a brief introduction to the core elements of deep learning, we show how to apply them to inverse problems. We analyze the most promising deep neural architectures and training methodologies and discuss their pros and cons.

In Chapter 6 we further extend deep learning to EIT. Despite several successful instances of solving various inverse problems, ML-EIT did not gain enough momentum and major challenges remain unsolved. Inspired by the insights from numerical simulations we develop

a novel approach to image cell nucleus without labeling. We explore several deep learning methods and show their strengths and weaknesses. Our approach provides a scalable solution for non-invasive single-cell imaging, a long-standing challenge in biology and raises a fundamental question of sensing inner cellular organelles with purely electrical AC field. We hope that the results demonstrated in this dissertation will reignite research efforts towards electrically-driven cellular imaging and tomography and bring new ideas that will end up in the development of a new realm of label-free cellular and sub-cellular imaging.

Finally, in Chapter 7 we summarize the major findings of this work and discuss possible directions of the future developments.

CHAPTER 2

Diversity in cellular response to electrical stimulations

Long-standing interest in electrical properties of biological cells and tissues gave birth to multiple sensing and imaging applications. Among them are ECIS, EIT, EIS, electroporation, DEP cell trapping and manipulation, cytometry, and electrical cell lysis. Low cost, non-invasiveness, and label-free nature of electrical stimulations make them attractive for cell biology research. The key underlying foundation behind these techniques is an accurate model of electrical properties of individual sub-cellular components, the entire cell, and multicellular systems. To build such model, one needs reliable empirical estimation of material properties of the cells, but physical size and biological diversity among cells challenged precise theoretical modelling for decades. With increased amount of collected experimental data, however, it became feasible to build a strong data-driven model.

Active experimental studies on cell properties began in 1960s with early efforts by Pauly *et al.* [54, 1], Loewenstein *et al.* [2], Carstensen *et al.* [55, 3] and Miyamoto *et al.* [4]. Numerous empirical and theoretical works were presented in subsequent years by Schwan, Asami, Pethig, Becker, Holzel, Gimsa, and many others [5, 6, 7, 8, 9, 10, 11, 12, 13, 14, 15, 16, 17, 18, 19, 20, 21, 22, 23, 24, 25, 26, 27, 28, 29]. The dominating method in electrical modelling of cells and tissues was the equivalent circuit model. Giaever and Keese approached modelling of a confluent layer of adherent cells with a lumped element circuit in their pioneering work on ECIS [38]. Their *et al.* described an equivalent circuit of an individual cell and the cell-electrode interface [57] revealing mechanisms behind electrical responses of a single cell and optimal parameters for the sensing applications. Huang *et al.* [60] reported a model based on Finite Element Method (FEM) and took into account frequency-dependent nature of the electrical properties of a single cell. Ren and Chui recently presented another 3D

model of a cell in their work on the fundamental feasibility of tracking changes of multiple cellular properties [59]. However, the aforementioned efforts ignore sub-cellular organelles and biological diversity.

Another important aspect is geometrical shape of the cells. During life-cycle, adherent cells undergo significant shape deformations due to spreading, crawling, division and apoptosis. Deformations can involve simple electrostatic interactions and sophisticated protein polymerization mechanisms. Steady isotropic and stochastic anisotropic spreading dominate in many adherent cells. Cell membrane and cytoplasm experience stronger deformations compared to cell organelles, which leads to heterogeneous electrical properties throughout the cell body [61]. Although being of significant importance, there was little progress towards engaging more realistic cell geometries in numerical modelling of electrical cellular response. Gowrishankar and Weaver[58] introduced a sophisticated network of lumped elements called Cartesian transport lattice (CTL) that was inherently dependent on the cell geometry. Huang *et al.* attempted to mimic a specific shape of a single adherent cell [60], but had to make a strong assumption on the symmetry of the geometry.

In this chapter, we describe a novel approach to simulate electrical cellular response [62]. The proposed model is the first to capture biodiversity across animal cells, yeast cell and bacteria; and the first to represent more realistic 3D shapes of adherent cells. The model is of relevance to a number of medical diagnostic and therapeutic applications that involve biological effects arising from the exposure to electric and magnetic fields, such as EIT, EIS, DEP, electroporation, and others. To verify robustness of the model we conduct impedance spectroscopy measurements on a single human cervical carcinoma (HeLa) cell.

2.1 Electrical properties of biological cells

We collected previously published experimental data and grouped them into five categories: adherent animal cells, non-adherent animal cells, yeast cells, bacteria, and other (tissues and bio-membranes). To visualize the entire dataset, we plot it in Figure 2.1, which shows that electrical properties tend to form small clusters and sometimes have a significant overlap

between different cell types. Given clustered structure of the data shown in Figure 2.1 and knowing that biological diversity in cellular electrical response is driven by complex unobservable processes inside the cell, parametric modelling is a natural choice. Moreover, parametric models have physical interpretations, generalize better with small training datasets, and provide sufficient power when mixed together. To mitigate inherent constraints on functional forms of the parametric approach, we employ a comprehensive list of distribution families. Note that a larger dataset is necessary for further investigation with more sophisticated models, as they simply overfit the dataset presented in this work.

Correlation analysis. Although correlation between cytoplasm and culture medium is frequently reported in the literature, we did not find a strong evidence of consistent linear relationship between the variables. Moreover, no strong relationship between conductivity and permittivity (as well as conductance and capacitance) within any cell component was found. We, therefore, proceed with univariate analysis of each dielectric property of individual cell components.

Univariate analysis. In our analysis, each electrical property is modelled as a random variable. We choose candidate models as the closest to the observations on Cullen and Frey graph [73] constructed using non-parametric bootstrap with 2000 iterations. To mitigate inherent constraints on functional forms of the parametric approach, we employ a comprehensive list of distributions including log-normal, normal, gamma, exponential, Weibull, t-distribution, inverse Gaussian (Wald), inverse normal, and inverse log-normal. Although more sophisticated statistical models were expected to produce a superior fit of biological diversity, they tend to overfit the data and result in poor generalization measured by cross-validation.

For each candidate distribution, we fit a mixture model by applying Expectation-Maximization (EM) algorithm[74]. At E-step, we estimate weights of the mixture components by maximizing the weighted log-likelihood for given model parameters. At M-step, we maximize the weighted log-likelihood to get new parameter estimates. To choose a proper number of

mixture components without overfitting, we use 5-fold cross validation and pick the one with the largest out-of-sample log-likelihood. As an alternative to cross-validation, we use the gap statistics [75] of complete-linkage hierarchical clustering. Interestingly, both methods always suggested the same number of mixture components. To ensure global convergence, we run each optimization 50 times with different weights initialization and take the best performing models. In each run, we initialize the mixture weights with either K-Means, hierarchical clustering, or random uniform (continuous and discrete) assignment.

When the data is insufficient for EM algorithm to converge in 1000 iterations, we use hard cluster assignment of each data point. Similarly to the previous procedure, we use K-Means, hierarchical clustering and random uniform (discrete) cluster assignment. We, then, fit a parametric model with Maximum Likelihood Estimation (MLE) for each cluster.

To reject the models we conduct non-parametric Kolmogorov-Smirnov (KS) test, and calculate the corresponding p-values (confidence level of 0.1) of the simulated bootstrapping of the KS-statistics as was suggested in literature [76]. To choose the best performing model, we carefully analyze the quantile-quantile (Q-Q) plots and compare Bayesian information criterion (BIC).

2.1.1 Cell membrane

The basic electrical model of cell membrane is an insulator made of a phospholipid bilayer of 4 - 10 nanometers (nm) thick. Presence of the ion channels and pores, however, significantly increases its electrical conductance per area, reaching $15 Sm/cm^2$. Combination of the active and passive transport mechanisms of the cell membrane can maintain different amounts of charge inside and outside the cell, which leads to significant electrical capacitance per unit area[77] of 1 - 10 $\mu F/cm^2$. Electrical properties of cell membrane are akin to those of a non-ideal capacitor with small leakage conductance.

It is well known that physical size of living tissues follows log-normal distribution. Given that capacitance (C_m) is inversely proportional to membrane's thickness, it is not surprising that it follows log-normal distribution across all cell types (see Table 2.1). Fundamentally,

such a relationship could be associated with multiplicative effects between random sequential events such as synthesis of proteins, formation of a phospholipid bilayer, and further assembly. Note, that the observed mixture components may describe distinct sub-populations within each cell type. Conductance of the cell membrane (G_m) follows gamma distribution. Since the average conductance per area of the membrane is proportional to the density of open ion channels and pores, one can presume the existence of exponentially distributed random processes of creating and destroying conductive paths in the membrane. For example, the time periods between the switching of the ion channels can be represented by such process with a specific rate.

2.1.2 Cytoplasm

Cytoplasm is a viscous liquid solution that fills the cell and comprises every organelle but nucleus. It is mainly composed of water, salts, and proteins that makes its conductivity reach 1 - 3 $S\text{m}/m$. Due to the presence of the bio-molecules and small organelles, dielectric constant of cytoplasm can be between 50 and 100.

We observe gamma and log-normal distributions of the conductivity (σ_{cyt}) and permittivity (ϵ_{cyt}) in cytoplasm respectively. One of the factors affecting cytoplasm's conductivity is modulating permeability of the cell membrane. Membrane channels, that adjust ion concentration inside the cell, can be modelled as stochastic pumps switching between "open" and "closed" states. The process of incremental change of the ionic concentration in cytoplasm could be causing gamma distributed conductivity. On the other hand, permittivity of the cytoplasm is dominated by the presence of polarizable organelles, membranes, proteins, and nucleic acids. It therefore follows log-normal distribution, which indicates a complex multiplicative process of biomolecule synthesis.

2.1.3 Cell nucleus

The largest organelle inside animal cells is nucleus, which occupies about 10% of the total cell volume and reaches 6 - 10 micrometers (μm) in diameter. The nuclear envelope (mem-

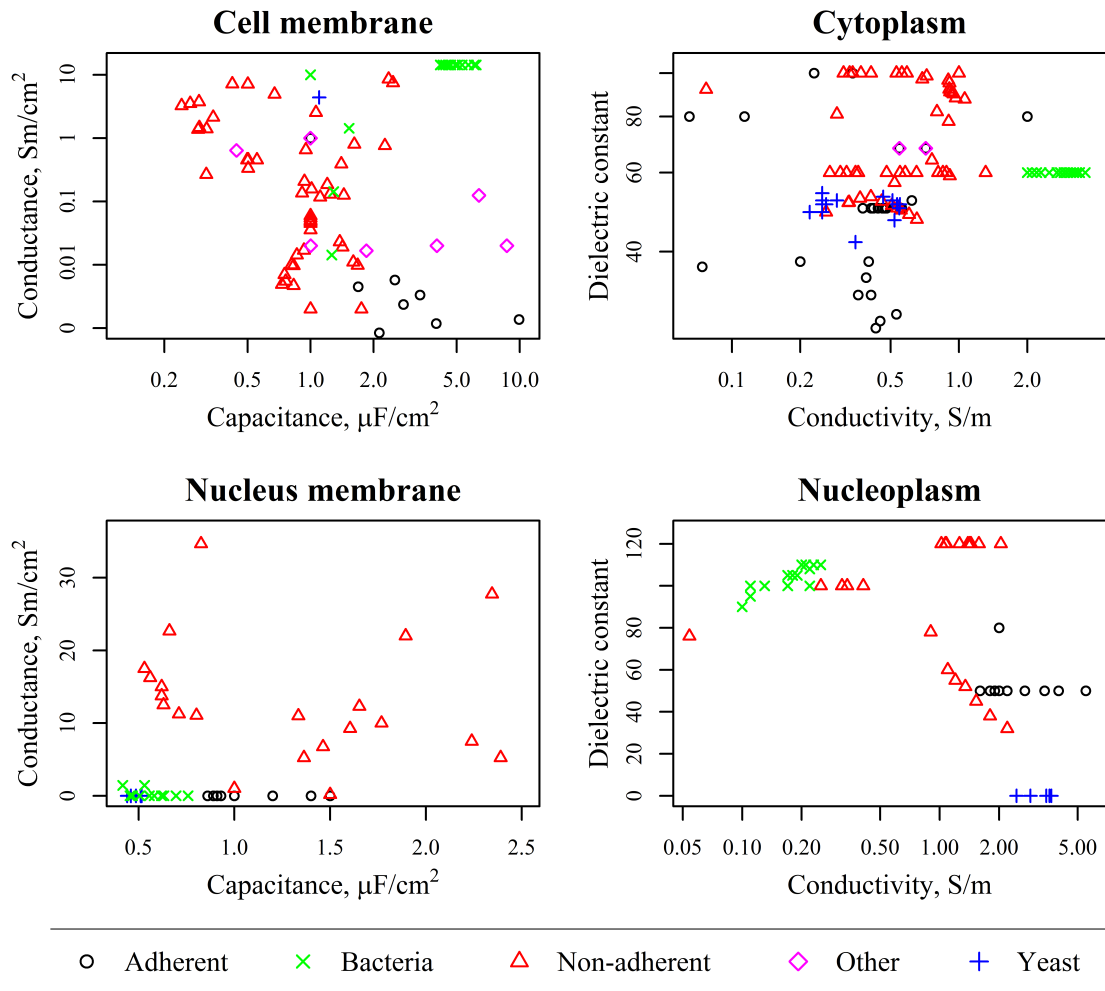


Figure 2.1: Electrical properties by cell type: adherent cells, non-adherent (suspended) cells, yeast cells, bacteria and other (tissues and membranes). Data was collected from the previously reported works [1, 2, 3, 4, 5, 6, 7, 8, 9, 10, 11, 12, 13, 14, 15, 16, 17, 18, 19, 20, 21, 22, 23, 24, 25, 26, 27, 28, 29]

brane) consists of two porous layers of total thickness of 20 - 50 *nm*. Small water-soluble molecules can freely penetrate the membrane through the pores, which increases its electrical conductivity.

We omit yeast cells and bacteria due to insufficient observed data, and summarize animal cells in Table 2.1. Electrical properties of the nucleus in animal cells (adherent and non-adherent cells combined) have the same nature as the cell membrane and cytoplasm. Driven by the biomolecule polarization, nucleus membrane capacitance (C_{nm}) and nucleoplasm permittivity (ϵ_{np}) follow log-normal distribution. On the other hand, the envelope conductance (G_{nm}) and nucleoplasm conductivity (σ_{np}) are dominated by regularly distributed pores in the envelope and follow gamma distribution.

2.1.4 Culture medium

Culture medium supports the growth of the cells. It is usually in a form of a salt solution containing high concentration of amino acids and vitamins, as well as additional supplementary components. Most commonly used ones include Dulbecco's Modified Eagle Medium (DMEM), Roswell Park Memorial Institute medium (RPMI), Minimum Essential Media (MEM), and Iscove's Modified Dulbecco's Medium (IMDM). Industry-level control over their chemical content minimizes variance in their electrical properties. As a result, experimental data is well modelled with uniform and normal distributions:

$$\begin{aligned}\sigma_{medium} &\sim Unif(0.1, 2.0) \quad [Sm/m] \\ \epsilon_{medium} &\sim \mathcal{N}(79.7224, 1.8949)\end{aligned}\tag{2.1}$$

2.1.5 Dielectric dispersion

So far, we have discussed electrical properties of the cells regardless of the frequency of the applied electric field. Because of unusual dispersion phenomenon, frequency-dependent characteristics are of a bigger practical importance. Dielectric dispersion, also called relaxation, is the response of a dielectric material to an external, oscillating (AC) electric field. Caused by the delay in polarization at higher frequencies, it leads to frequency-dependent complex

Table 2.1: Electrical properties of cell components

Property	Cell type	Family	Components	Parameters	Test statistic
C_m , $\mu F/cm^2$	Adherent	Lnorm	$\pi = \{0.6249, 0.3751\}$	$\mu_{log} = \{0.9430, -0.3745\}$ $\sigma_{log} = \{0.3713, 0.1833\}$	$KS = 0.0729$ $p-val = 0.9988$
	Non-adh	Lnorm	$\pi = \{0.6710, 0.3290\}$	$\mu_{log} = \{0.0753, 0.0958\}$ $\sigma_{log} = \{0.7332, 0.3140\}$	$KS = 0.0831$ $p-val = 0.9507$
	Bacteria	Lnorm	$\pi = \{0.4602, 0.5398\}$	$\mu_{log} = \{-0.2412, 1.5514\}$ $\sigma_{log} = \{0.9473, 0.1176\}$	$KS = 0.1878$ $p-val = 0.7644$
	Yeast	Lnorm	$\pi = \{0.3571, 0.6429\}$	$\mu_{log} = \{-0.3522, 0.1261\}$ $\sigma_{log} = \{0.0153, 0.0626\}$	$KS = 0.1014$ $p-val = 0.9860$
G_m , Sm/cm^2	Adherent	Gamma	$\pi = \{1\}$	$shape = 0.1641$ $rate = 2.8960$	$KS = 0.3966$ $p-val = 0.5591$
	Non-adh	Gamma	$\pi = \{1\}$	$shape = 0.3138$ $rate = 0.2869$	$KS = 0.1542$ $p-val = 0.8264$
	Bacteria	Insufficient data. Takes values from 0.01 to 14.3 Sm/cm^2			
	Yeast	Usually reported as non-conductive			
ϵ_{cyt}	Adherent	Lnorm	$\pi = \{1\}$	$\mu_{log} = 3.9857$ $\sigma_{log} = 0.3790$	$KS = 0.1848$ $p-val = 0.8261$
	Non-adh	Lnorm	$\pi = \{0.5460, 0.4540\}$	$\mu_{log} = \{4.0248, 4.5445\}$ $\sigma_{log} = \{0.0898, 0.0737\}$	$KS = 0.1729$ $p-val = 0.6828$
	Bacteria	Insufficient data			
	Yeast	Lnorm	$\pi = \{1\}$	$\mu_{log} = 3.9160$ $\sigma_{log} = 0.0600$	$KS = 0.2460$ $p-val = 0.7807$
σ_{cyt} , Sm/m	Adherent	Gamma	$\pi = \{1\}$	$shape = 4.0489$ $rate = 10.0158$	$KS = 0.1015$ $p-val = 0.6518$
	Non-adh	Gamma	$\pi = \{1\}$	$shape = 4.7512$ $rate = 7.8888$	$KS = 0.1014$ $p-val = 0.9650$
	Bacteria	Weibull	$\pi = \{1\}$	$shape = 8.7034$ $scale = 3.0522$	$KS = 0.1703$ $p-val = 0.8634$
	Yeast	Gamma	$\pi = \{0.5714, 0.4286\}$	$shape = \{57.502, 280.000\}$ $rate = \{216.987, 537.772\}$	$KS = 0.1663$ $p-val = 0.9484$
C_{nm} , $\mu F/cm^2$	Adherent & Non-adh	Lnorm	$\pi = \{1\}$	$\mu_{log} = 0.0969$ $\sigma_{log} = 0.4330$	$KS = 0.1228$ $p-val = 0.9657$
G_{nm} , Sm/cm^2	Adherent & Non-adh	Gamma	$\pi = \{1\}$	$shape = 1.5337$ $rate = 0.1180$	$KS = 0.1684$ $p-val = 0.9847$
ϵ_{np}	Adherent & Non-adh	Lnorm	$\pi = \{1\}$	$\mu_{log} = 4.1114$ $\sigma_{log} = 0.3756$	$KS = 0.1372$ $p-val = 0.9937$
σ_{np} , Sm/m	Adherent & Non-adh	Gamma	$\pi = \{1\}$	$shape = 2.3099$ $rate = 1.3536$	$KS = 0.1632$ $p-val = 0.5132$

permittivity. Schwan and Cole pioneered the field with analysis of the dispersion observed in tissues and cell suspensions [56, 78, 79]. Dielectric properties of such systems change in distinct steps called alpha (α), beta (β), and gamma (γ) dispersion. A thorough review of underlying mechanisms was presented by Pethig [7]. Some authors also distinguish delta (δ) dispersion between 0.1 and 3 GHz , but due to lack of clear mechanisms, its interpretation is complicated.

Extraordinarily large permittivity below 100 kHz is the main result of α -dispersion. It is believed to be caused by the counter ion diffusion in response to the charged cell surface. Frequency-dependent conductance of the cell membrane proteins and charging of the interior organelle membranes can also contribute to α -dispersion. Between 0.1 MHz and 100 MHz , β -dispersion takes place. It primarily arises from Maxwell-Wagner interfacial polarization of the cell membrane. Relaxation effects in the proteins, amino acids and inner organelle membranes also contribute to the tail of β -dispersion. In contrast with α -dispersion, fluid conductivity noticeably raises in β -dispersion band. The main cause of γ -dispersion is dipolar relaxation of water, which accounts for about 80% of the cell body. Gamma-dispersion happens around 1 - 50 GHz and results in a significant jump of conductivity and relatively small changes in permittivity.

Relaxation of an ideal, non-interacting population of dipoles under an AC external electric field is described by Debye equation. However, a commonly accepted model for cell suspension from 1 kHz to 1 GHz is based on Cole-Cole equation, describing relative dielectric constant:

$$\epsilon^*(f) = \epsilon'(f) + i\epsilon''(f) = \epsilon_{HF} + \frac{\epsilon_{LF} - \epsilon_{HF}}{1 + (i2\pi f\tau)^{1-\alpha}} \quad (2.2)$$

where ϵ^* , ϵ' , ϵ'' are complex dielectric constant and its real and imaginary parts respectively; ϵ_{LF} , ϵ_{HF} are the static and high-frequency dielectric constants; f is frequency; τ , α are a time constant and a shape parameter that define a range of frequencies of the dispersion. When $\alpha = 0$, Cole-Cole equation 2.2 simplifies to Debye equation. If we take $\Delta\epsilon = 1 - \epsilon_{HF}/\epsilon_{LF}$ and $\omega = 2\pi f$, equation 2.2 can be further split into equations 2.3 and 2.4. Note, that the static

Table 2.2: Dielectric dispersion parameters estimation

Material	$\tilde{\alpha}$	$\tilde{\Delta\epsilon}$	$\tilde{\tau}$, sec
Cell membrane	$\mu = 0.5302; \sigma = 0.2157$	$\mu = 0.6717; \sigma = 0.2390$	$\mu = 8.0189 \cdot 10^{-7}; \sigma = 1.3514 \cdot 10^{-7}$
Cytoplasm	$\mu = 0.1385; \sigma = 0.0416$	$\mu = 0.7979; \sigma = 0.1454$	$\mu = 1.3860 \cdot 10^{-7}; \sigma = 4.5010 \cdot 10^{-8}$
Organelle membr	$\mu = 0.4199; \sigma = 0.2103$	$\mu = 0.7783; \sigma = 0.2199$	$\mu = 2.5042 \cdot 10^{-4}; \sigma = 1.2146 \cdot 10^{-5}$
Organelle interior	$\mu = 0.1982; \sigma = 0.0930$	$\mu = 0.7925; \sigma = 0.1058$	$\mu = 1.1757 \cdot 10^{-7}; \sigma = 6.4540 \cdot 10^{-8}$
Culture medium	$\mu = 0.2167; \sigma = 0.1000$	$\mu = 0.9208; \sigma = 0.2100$	$\mu = 5.00 \cdot 10^{-11}; \sigma = 3.41 \cdot 10^{-12}$

conductivity and permittivity correspond to the stochastic electrical properties described previously.

$$\epsilon'(f) = \epsilon_{LF} \left(1 - \Delta\epsilon \frac{(\omega\tau)^{1-\alpha} \sin \frac{\alpha\pi}{2} + (\omega\tau)^{2(1-\alpha)}}{1 + 2(\omega\tau)^{1-\alpha} \sin \frac{\alpha\pi}{2} + (\omega\tau)^{2(1-\alpha)}} \right) \quad (2.3)$$

$$\sigma(f) = \sigma_{LF} + \frac{\epsilon_{LF}\omega\epsilon_0\Delta\epsilon(\omega\tau)^{1-\alpha} \cos \frac{\alpha\pi}{2}}{1 + 2(\omega\tau)^{1-\alpha} \sin \frac{\alpha\pi}{2} + (\omega\tau)^{2(1-\alpha)}} \quad (2.4)$$

We collected previously reported data [54, 1, 3, 5, 6, 7, 8, 9, 10, 11, 12, 13, 14, 15, 16, 17, 18, 80, 81, 82, 83, 84, 85, 86, 87] and extracted the corresponding dispersion equations and their parameters to generate curves of complex dielectric constants against the original frequencies. For each generated curve, we applied Levenberg-Marquardt algorithm (also called damped least-squares) to fit them to equation 2.2. To rule out the local minimum estimates, we ran each optimization 10^3 times with different initial estimates and took parameters with the highest adjusted coefficient of determination. We then found the means and the standard deviations of the estimated $\tilde{\alpha}$, $\tilde{\tau}$, $\tilde{\Delta\epsilon}$ for each cell component (see Table 2.2).

2.2 Numerical simulations

FEM subdivides a large problem into smaller subdomains that are called finite elements. The systems of equations that model the finite elements are then combined into the entire model. FEM gives accurate representation of complex geometries, allows dissimilar material properties, and captures local effects. We employ COMSOL Multiphysics's AC/DC module in frequency domain to solve current conservation equation based on Ohm's law. Built-in discretization engine takes a randomly generated cell shape, places it onto a predefined array

of microelectrodes, and builds an appropriate mesh (see Figure 2.4 (F)). To numerically solve the corresponding partial differential equations (PDEs), we use flexible generalized minimal residual method (FGMRES), an iterative procedure that gives an efficient trade-off between computational cost and solution quality. Our approach is easily scaled up to thousands of concurrent simulations and provides high quality results.

2.2.1 Cell geometry

While non-adherent cells maintain almost the same shape throughout the life-cycle, the adherent cells substantially deform, which leads to a sophisticated electrical response. Minutes after an adherent cell encounters a surface, it starts passive isotropic adhesion (spreading). Isotropic spreading ends when the cell reaches the balance between the energy gained through the adhesion to the surface and the energy dissipated by the deformations in the cell's actin cortex. This process is characteristically similar to a liquid droplet spreading on a surface [88, 89]. Later crawling creates significant deformations driven by actin polymerization and myosin contraction [90]. It has been experimentally shown that cells migrate via short-lived extension and retraction events ($< 1 \text{ min}$) which, over the course of many minutes, result in a net movement of the cell's leading and trailing edges [91, 92]. Stochastic nature of protrusion initiation in the segments of the cell edge leads to an anisotropic mode of motility, the basis for other cell motility processes such as polarization and migration.

During the initial isotropic spreading elasticity of the cell membrane plays a central role. Among copious models describing deformations of the cell membrane, a commonly accepted one is fluid mosaic model that mimics it as a two-dimensional fluid-like lipid bilayer with partially or fully embedded proteins [93]. More recent geometric models [94, 95] produce more realistic shapes, but may lead to sharp local curvature of the membrane surface [96], which makes them inapplicable in finite-element simulations as it complicates meshing.

To guarantee high quality meshing and numerical convergence we approximate a vertical profile of the cell membrane with surface wetting equation that has similar nature [97]. In addition to it, the rigidity of the nucleus leads to a small knob-looking deformation of the cell

membrane around its origin, hence, we appropriately modify the surface wetting equation as follows:

$$z(\rho) = \sqrt{\frac{\rho_0^2}{\sin^2 \theta} - \rho^2} - \frac{\rho_0}{\tan \theta} + \Pi\left(\frac{\rho}{2a_n}\right) \left(c_n \sqrt{1 - \frac{\rho^2}{a_n^2}}\right) \quad (2.5)$$

where $0 \leq \rho \leq \rho_0$, θ are radius and contact angle of the droplet (cell) respectively, a_n, b_n, c_n are the principal semi-axes of the nucleus along x, y, z respectively, and $\Pi(\cdot)$ is a rectangular (pulse) function. Note, that this assumes that the height of the droplet at the origin satisfies $\rho_0 \frac{1 - \cos \theta}{\sin \theta} \geq c_n$

To ensure realistic changes in the cell membrane area and the cytoplasm volume, we introduce two more optimization constraints. Before the spreading, volume of the cytoplasm and area of the cell membrane are approximately equal to $V_{cyto} = V_{cell} - V_{nucleus} = 4/3\pi(R_{cell}^3 - a_n b_n c_n)$ and $A_m = 4\pi R_{cell}^2$ respectively. Therefore, we have:

$$\left| \frac{\sum_i \Delta z_i \sum_j \frac{\rho_{ij}^2 \Delta \phi_j}{2} - 4/3\pi(R_{cell}^3 - a_n b_n c_n)}{4/3\pi(R_{cell}^3 - a_n b_n c_n)} \right| \leq \Delta V \quad (2.6)$$

$$\left| \frac{\pi \rho_0^2 + \sum_i \Delta z_i \sum_j \rho_{ij} \Delta \phi_j - 4\pi R_{cell}^2}{4\pi R_{cell}^2} \right| \leq \Delta A$$

We can rewrite the volumetric constrain to derive a first-order approximation for ρ_0 :

$$\pi \int_0^{c_n} [z^{-1}(\rho)]^2 dz \leq \frac{4}{3}\pi(R_{cell}^3 - a_n b_n c_n)(1 + \Delta V), \quad (2.7)$$

$$\rho_0^2 - \rho_0 \frac{c_n}{\tan \theta} - \frac{c_n^2}{3} - \frac{4(R_{cell}^3 - a_n b_n c_n)(1 + \Delta V)}{3c_n} \leq 0. \quad (2.8)$$

Equilibrium shape of cell membrane is given by equation 2.9, where λ is surface tension, Δp is the difference in pressure outside and inside the cell, k_c is bending rigidity of the surface, c_0 is spontaneous curvature, and H, K are mean and Gaussian curvatures respectively. To solve it we apply iterative running-mean optimization procedure for each horizontal slice at z_i as depicted in the pseudocode in Figures 2.2 and 2.3. Few randomly generated shapes are shown in Figure 2.4 (A-D) including assembly of cells, which can be used to mimic complex cell networks and tissues.

```

1: procedure MAIN
2:   initialize  $\Delta p, k_c, \lambda, c_0, z, \epsilon, \theta, \Delta A, \Delta V, R_{cell}, a_n, b_n, c_n$ 
3:    $A_m \leftarrow 4\pi R_{cell}^2, V_{cyto} \leftarrow \frac{4}{3}\pi(R_{cell}^3 - a_n b_n c_n)$ 
4:    $\rho_0 \leftarrow \max\{x : x^2 - \frac{c_n}{\tan\theta}x - \frac{c_n^2}{3} - \frac{4(R_{cell}^3 - a_n b_n c_n)(1 + \Delta V)}{3c_n} = 0\}$ 
5:    $\phi \leftarrow [-\pi, \pi)$ 
6:   stochastically initialize protrusions  $\rho^*$  at angles  $\phi^*$ 
7:   for all  $z_i$  do
8:     for all  $\phi$  do
9:        $\rho(\phi) \leftarrow \left\{ x : \sqrt{\frac{\rho_0^2}{\sin^2\theta} - x^2} - \frac{\rho_0}{\tan\theta} + \Pi\left(\frac{x}{2a_n}\right) \cdot (c_n \sqrt{1 - \frac{x^2}{a_n^2}}) - z_i = 0 \right\}$ 
10:    end for
11:    for all  $\phi^*$  do
12:       $\rho(\phi) \leftarrow \rho^* \sqrt{\frac{\rho_0^2}{\sin^2\theta} - (z_i + \frac{\rho_0}{\tan\theta})^2}$ 
13:    end for
14:     $\rho_{OPT}(z_i) \leftarrow \text{OPT}(\rho(\phi), \phi^*)$ 
15:  end for
16:   $V \leftarrow \sum_j \Delta z_j \sum_i \frac{\rho_{ij}^2 \Delta \phi_i}{2}$ 
17:   $A \leftarrow \pi \rho_0^2 + \sum_j \Delta z_j \sum_i \rho_{ij} \Delta \phi_i$ 
18:  if  $\frac{|A - A_m|}{A_m} > \Delta A$  then
19:     $c_a \leftarrow \left(\frac{A_m + \Delta A}{A}\right)^{1/2}$ 
20:     $\rho_{OPT} \leftarrow \rho_{OPT} \cdot c_a$ 
21:  end if
22:  if  $\frac{|V - V_{cyto}|}{V_{cyto}} > \Delta V$  then
23:     $c_v \leftarrow \left(\frac{V_{cyto} + \Delta V}{V}\right)^{1/3}$ 
24:     $\rho_{OPT} \leftarrow \rho_{OPT} \cdot c_v$ 
25:  end if
26:   $surf \leftarrow$  transform  $\rho_{OPT}$  into a surface with cubic spline interpolation
27:   $obj \leftarrow$  convert  $surf$  into a solid return  $obj$ 
28: end procedure

```

Figure 2.2: Pseudocode for cell geometry generation

$$\Delta p - 2\lambda H + k_c(2H + c_0)(2H^2 - c_0H - 2K) + 2k_c \nabla^2 H = 0 \quad (2.9)$$

2.2.2 Electrodes-solution interface

When an electrode is exposed to electrolytic solution, electric double layer (EDL) forms at the interface. Gouy-Chapman-Stern is a commonly accepted model of EDL [98]. The first layer (inner Helmholtz plane, IHP), comprises of ions adsorbed onto the surface due to chemical interactions (see Figure 2.5). The second (diffuse) layer is composed of ions of the

```

1: procedure OPT( $\rho(\phi), \phi^*$ )
2:   for all  $\phi$  do
3:      $H(\phi) \leftarrow \frac{1}{\rho(\phi)}$ 
4:      $K(\phi) \leftarrow \frac{1}{\rho(\phi)}$ 
5:   end for
6:    $err \leftarrow \infty$ 
7:   while  $err > \epsilon$  do
8:     for all  $\phi_j \in \phi \setminus \phi^*$  do
9:        $\Delta\rho \leftarrow \left| 1 - \frac{mean(\rho(\phi_{j-1..j+1}))}{\rho(\phi_j)} \right| + c_0\mathcal{N}(0, 1)$ 
10:      if  $\left| \frac{\Delta\rho - \rho(\phi_j)}{\rho(\phi_j)} \right| > \gamma$  then
11:         $\Delta\rho \leftarrow \gamma$ 
12:      end if
13:       $\rho(\phi_j) \leftarrow \rho(\phi_j) \cdot (1 + \Delta\rho)$ 
14:    end for
15:    for all  $\phi$  do
16:       $H(\phi) \leftarrow \frac{1}{\rho(\phi)}$ 
17:       $K(\phi) \leftarrow \frac{1}{\rho(\phi)}$ 
18:    end for
19:     $err \leftarrow |\Delta p - 2\lambda H + k_c(2H + c_0)(2H^2 - c_0H - 2K) + 2k_c\nabla^2 H|$ 
20:  end while return  $\rho(\phi)$ 
21: end procedure

```

Figure 2.3: Pseudocode of optimization subroutine used in cell geometry generation

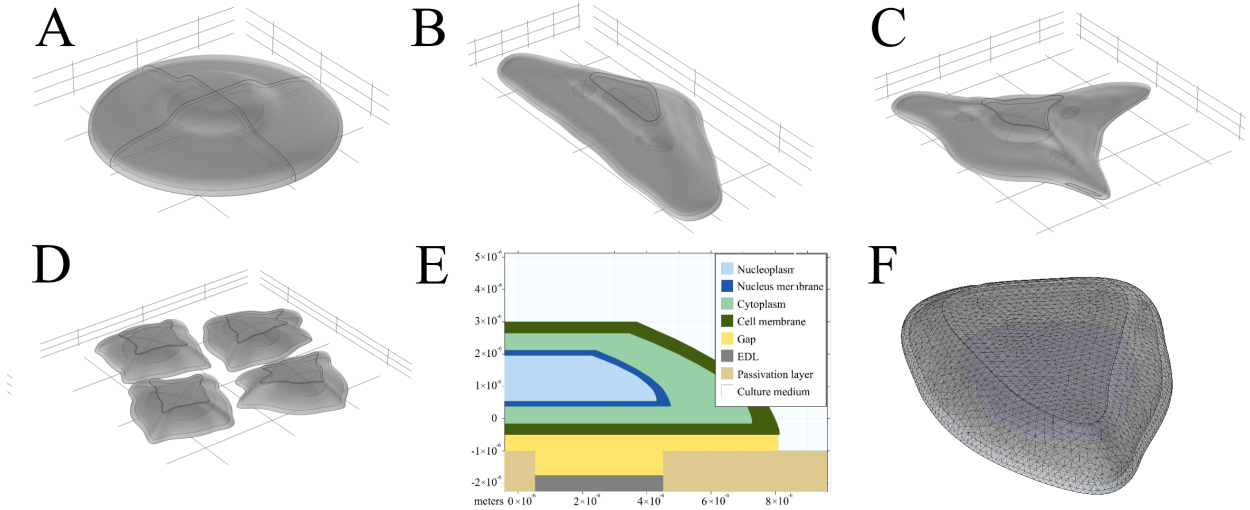


Figure 2.4: Examples of the cell geometries: (A) isotropic spreading, (B-C) anisotropic spreading, (D) assembly of cells, (E) cell structure schematic, (F) finite-element mesh

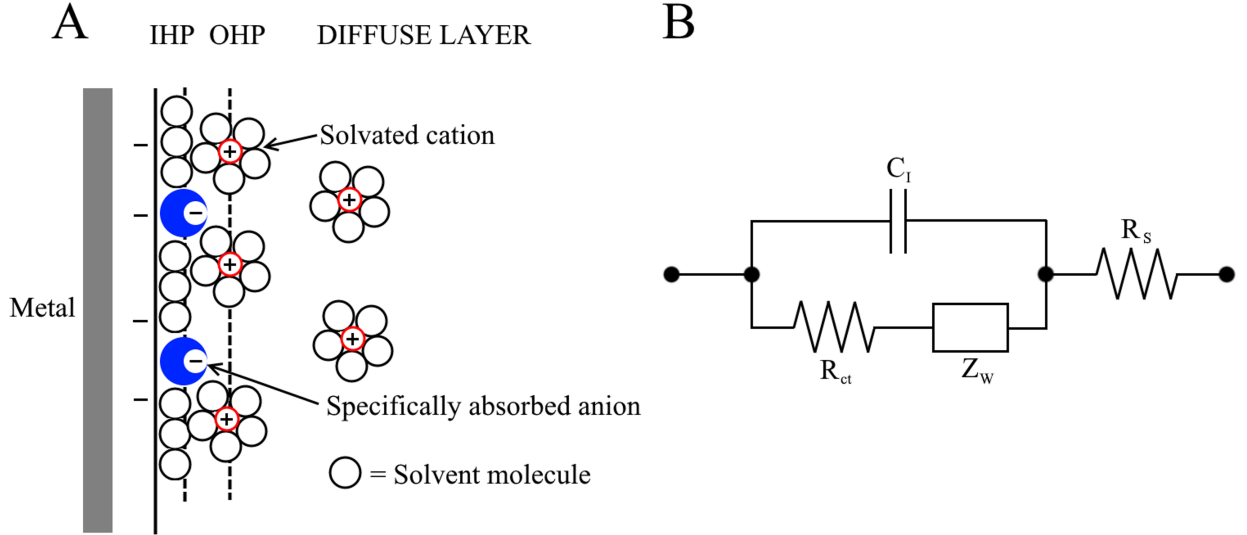


Figure 2.5: Electrical Double Layer (EDL): (A) physical structure and (B) its lumped-element model

opposite charge attracted to the surface by Coulomb force, which leads to a virtual capacitance at the interface (C_I). Faradaic processes are modelled as charge transfer resistance (R_{ct}) connected in series with Warburg impedance (Z_W), which mimics the ionic diffusion. Spreading resistance (R_S) represents the conduction path in the electrolyte.

Electric potential, applied to the electrode (against another counter electrode), causes a red-ox reaction at the interface and exponential growth in the net current flow. The charge transfer resistance R_{ct} is inversely proportional to the electric current density and has negligible effect in many practical scenarios. Diffusion-driven Warburg impedance, however, remains constant and is only limited by the ion mobility in the solution. In response to the applied AC voltage, Z_W decreases with frequency as $f^{-0.5}$. Interfacial capacitance C_I is commonly reported to be in the order of 4 - 20 $\mu F/cm^2$. The complete model for EDL under applied AC voltage can be described by its frequency-dependent conductivity (σ_{dl}) and permittivity (ϵ_{dl}):

$$\sigma_{dl} + i\omega\epsilon_{dl} = thickness_{dl} \left[\frac{\omega^{0.5}}{K_w} + i\frac{\omega^{0.5}}{K_w} + i\omega C_I \right] \quad (2.10)$$

where $\omega = 2\pi f$, K_w is interface-specific constant, that was reported to be around 2000 -

$5000 \Omega \cdot sec^{-0.5} \cdot cm^2$ for gold electrodes [60].

Beyond the EDL, the gap between the electrodes and an adherent cell is filled with culture medium. Depending on the strength of adhesion, the thickness of this gap can vary. We model this region with a fixed-thickness domain and modulate its conductivity and permittivity to take into account true varying thickness (equation 2.11). The schematic of the model is shown in Figure 2.7 (C).

$$\begin{cases} \sigma_{gap} = \frac{t_{real}}{t_{fixed}} \sigma_{media} \\ \epsilon_{gap} = \frac{t_{real}}{t_{fixed}} \epsilon_{media} \end{cases} \quad (2.11)$$

2.2.3 Importance of cell geometry

Conventional FEM models of electrical cellular response assume naive cell shapes. The proposed geometry generation procedure is intended to enhance the quality of the numerical modelling by introducing local cell protrusions. However, the resulting geometries are not naturally occurring cell shapes, but rather smooth efficient approximations. To illustrate the limitations of the proposed method, we compare previously published serial transmission electron microscopy (TEM) image of an inter-phase human pancreatic carcinoid cell line (BON) cell [30] and its smooth approximation, which we generated by averaging every 20 slices and using them as initial slices for the proposed procedure. As can be seen from Figure 2.6, the proposed method is unable to mimic cell morphology and results in monotonic vertical profile. On the other hand, the geometry catches the overall shape, area, and volume of the cell, which is more important for almost all applications involving electrical cellular response, as we show later. Moreover, while 3D TEM image has ultra-high resolution, its acquisition is often complicated and the resulting sliced image does not convert into mesh due to vast surface discontinuities seen in Figure 2.6 (A, B).

Our choice of cell's vertical profile, geometrical constraints, and other simplifications is driven by the trade-off between precision and practical considerations. To investigate the overall efficacy of the chosen approach we consider cell geometries of different levels

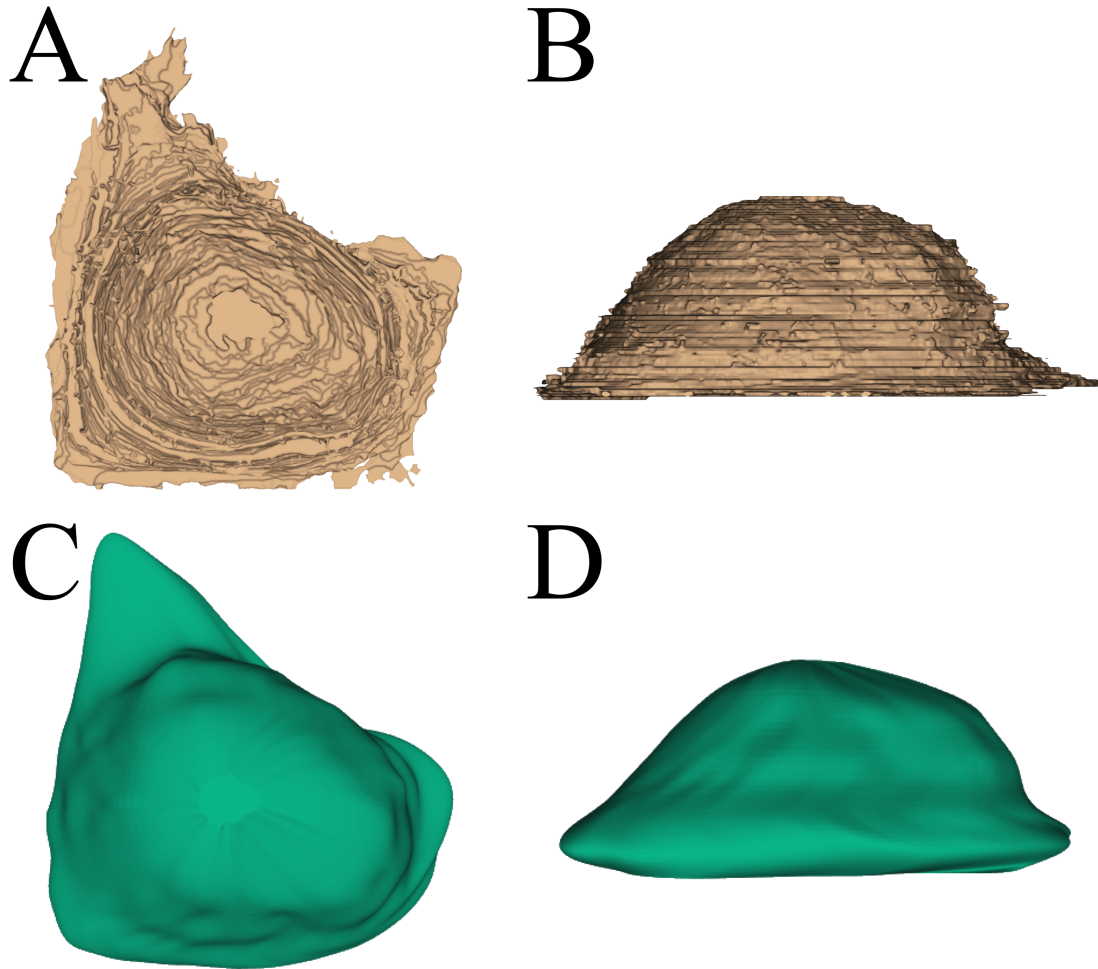


Figure 2.6: Top view and side view of a BON cell. (A-B) Experimental 3D reconstruction generated by serial sectioning TEM and segmentation of the cell outline (brown) and (C-D) its smooth approximation. The experimental 3D reconstruction is based on data from Villinger C. et al. (2014) Three-dimensional imaging of adherent cells using FIB/SEM and STEM. In: Kuo J. (eds) *Electron Microscopy. Methods in Molecular Biology (Methods and Protocols)*, vol 1117. Humana Press, Totowa, NJ. Copyright Springer Science+Business Media, New York 2014. The data was provided by authors of the study[30]

of detail as shown in Figure 2.7. A model with the highest level of detail (blue in the figure, purchased from CGTrader) represents realistic cell geometry that preserves natural local protrusions and cell morphology. Moderate level of detail (green) is achieved using the proposed procedure by initializing the bottom slice with the corresponding slice in the original image. The model with the lowest level of detail (yellow) is a frequently assumed naive ellipsoidal approximation. At the origin of each geometry we place ellipsoidal nucleus with major axes of $7 \times 7 \times 1 \mu m$. All geometries have total volume of around $2700 \mu m^3$, surface area of $2250 \mu m^2$, and cover $1000 \mu m^2$ on the bottom surface.

To evaluate the fidelity of the cell geometries, we simulate single cell electrical impedance measurement at $1 MHz$. In particular, we build a $200 \times 200 \times 200 \mu m$ solution domain placed on a dielectric passivation surface (silicone dioxide). We then insert a cell attached to the bottom surface and create an active electrode (circle of diameter d_{el}) underneath the cell located at δ_{el} from the center of the cell along the cross-section line as schematically shown in Figure 2.7 (C). Five grounding counter electrodes of size $200 \times 200 \mu m$ each are set at the external faces of the solution domain. We calculate the impedance as the ratio between the voltage applied at the active electrode and integral of the current density at the counter electrodes. Parameters and conditions were kept equal during testing of each cell geometry. To have equivalent mesh quality, we kept approximately the same mean and minimum values of skewness and volume versus circumradius of the mesh for all simulations. As an error metric we employed relative difference in the absolute impedance response $(|Z| - |Z_{real}|)/(|Z_{real}|) \cdot 100\%$, where Z_{real} is impedance response of the realistic cell geometry (blue in Figure 2.7).

In the first set of simulations (Figure 2.8 (A)) we had the active electrode aligned with the cell geometry ($\delta_{el} = 0$). We observed a significant error in naive geometry when d_{el} approaches the size of the cell. A closer look at the magnitude of the current density in the plane between the surface and the bottom of the cell (see Figure 2.9 (A-B)) discovered that the discrepancy is caused by difference in the covered electrode areas. Current density at the edges of the proposed cell geometry is depicted in Figure 2.9 (C-D) and shows dominant lateral flow in the cell gap region. Near the edge of the cell, however, current flow pattern

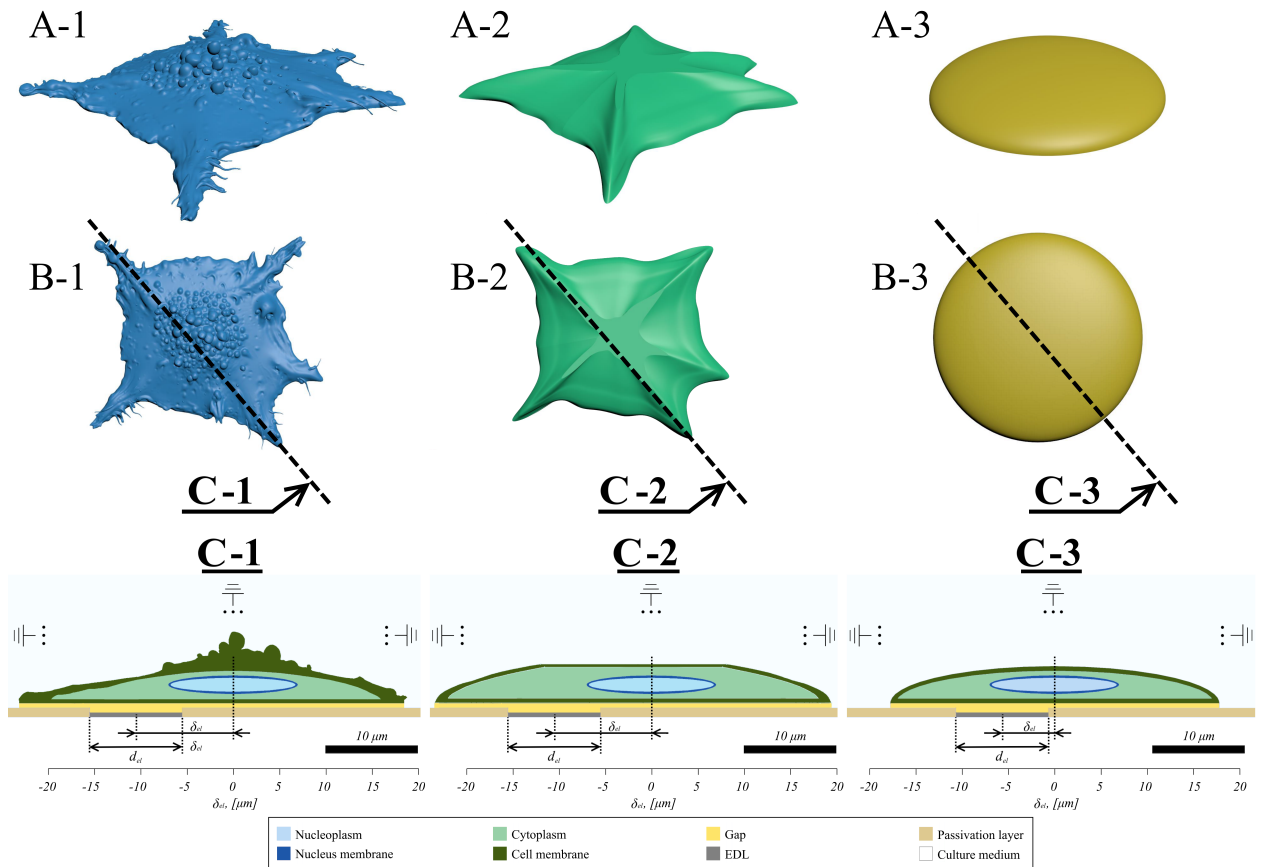


Figure 2.7: Level of detail in cell geometries: (A) 3D view, (B) top view, and (C) cross section of a human lung cancer cell at different levels of detail (1 - highest (realistic), 2 - moderate (proposed), 3 - lowest (naive)); (C) cross sections include schematic sketches of the active electrode placement underneath the cell

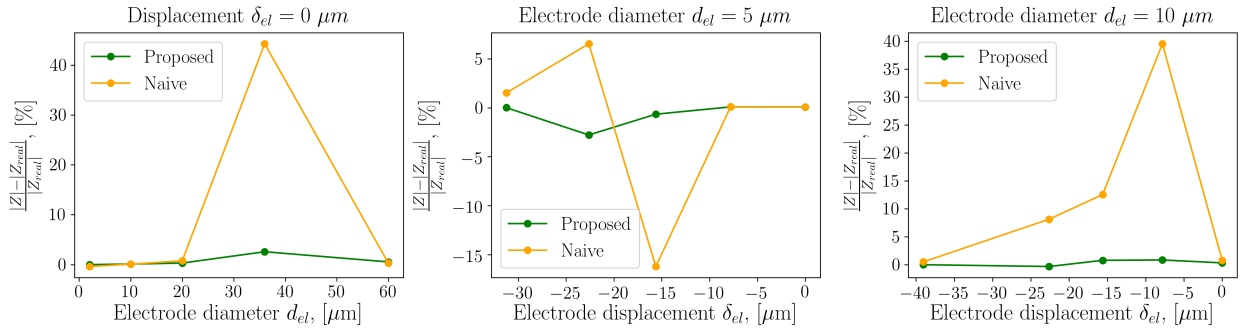


Figure 2.8: Testing fidelity of the cell geometries against (A) varying electrode size and (B-C) electrode displacement

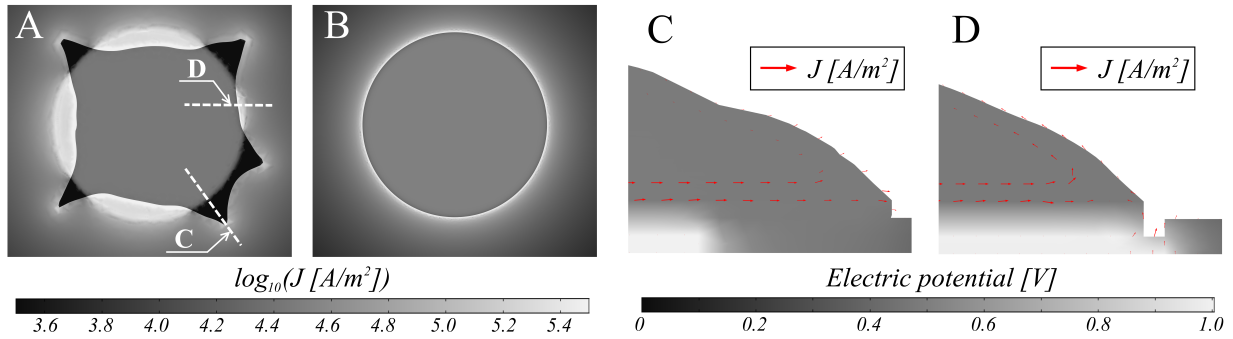


Figure 2.9: Electric current flow: underneath (A) proposed cell geometry and (B) naive cell geometry as well as the cross-sections (C) and (D) at the edges of the proposed geometry shown by the dashed lines

Table 2.3: Computational complexity associated with levels of detail of cell geometry

Metric	Realistic	Proposed	Naive
Average degrees of freedom (entire model)	1,119,844	237,525	118,062
Mesh size of the cell, elements	113,402	15,880	5,297
Time to solve [<i>min</i> , <i>max</i>], sec.	[570, 635]	[114, 127]	[54, 60]

is drastically different and highly depends on the extension of the cell membrane over the electrode, which emphasizes the importance of accurate cell shape representation. When we fixed electrode size d_{el} and introduced electrode displacement $\delta_{el} \neq 0$ (see Figure 2.8 (B-C)), we found another limitation of naive geometry. Impedance measurements with smaller electrodes at the vicinity of the cell edges become inaccurate due to presence of membrane protrusions. Interestingly, that naive geometry can lead to overestimated and underestimated results, while the proposed geometry consistently had small error. Both scenarios are common in biomedical engineering and demonstrate that the proposed simplified geometry is sufficient to enable accurate estimation of the electrical cellular response. Moreover, to show computational efficiency we report numerical complexity in Table 2.3. More sophisticated models describing adherent cell shape formation may bring higher precision, however they are not of a primary focus of this work. From practical perspective, such models can lead to numerical singularities during meshing, while being only useful for depicting micro-scale shape curvatures and associated local electrical potential changes.

2.3 Adherent cell simulations

To experimentally verify the entire approach of modelling adherent animal cells, we measured EIS response of a single human cervical carcinoma cell (see Figure 2.10). A small microelectrode array (MEA) was used to obtain independent electrical measurements. We imaged the sample with fluorescent microscopy and translated it into 3D mesh for FEM simulations. Experimental results were compared against the simulations.

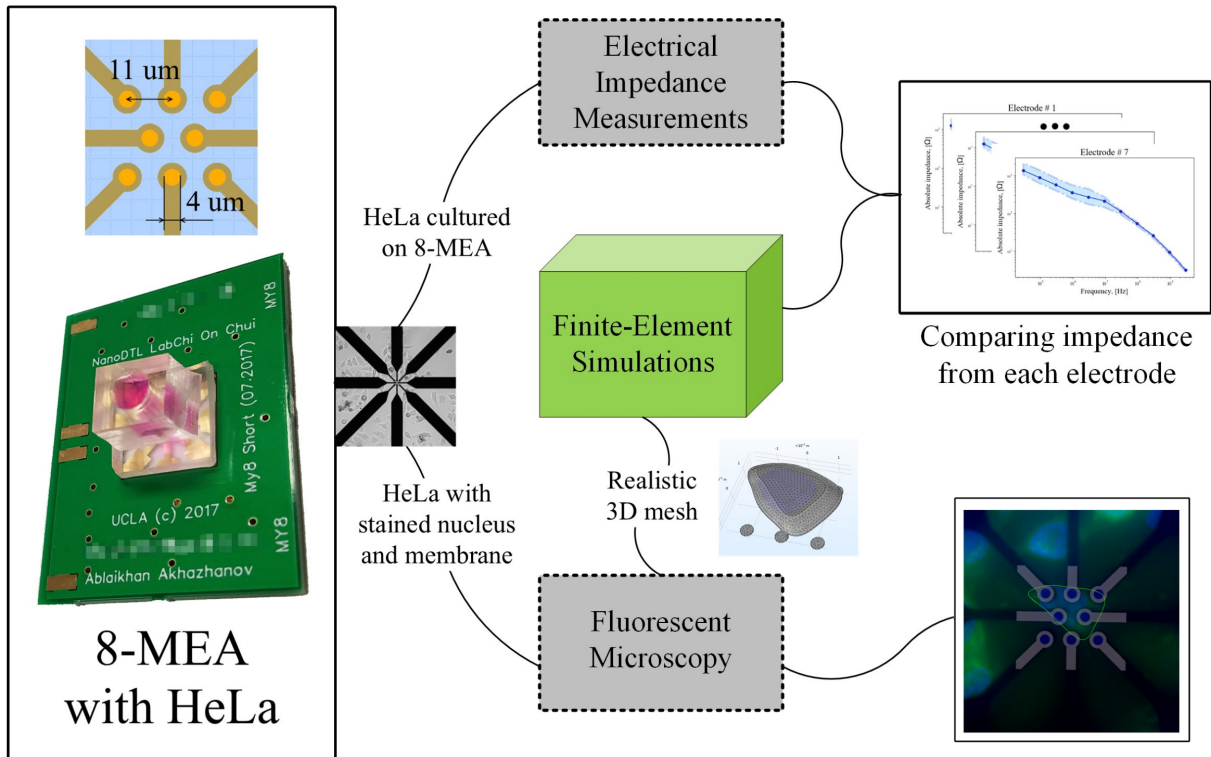


Figure 2.10: Experimental verification of the model with EIS measurements and FEM simulations of a HeLa cell on 8-electrode array

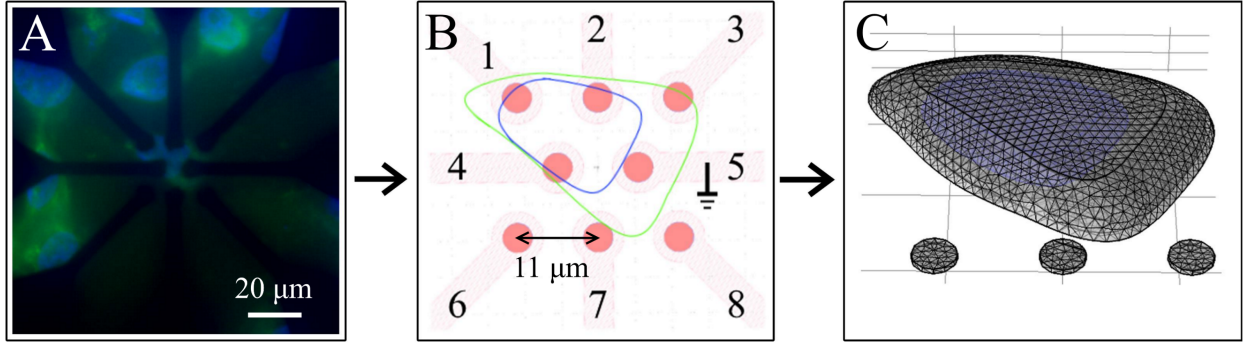


Figure 2.11: Translation of the fluorescent microscopy image into finite-element mesh

In Figure 2.11 (B), electrode 4 is located beneath the cell nucleus, electrode 3 is partially covered by the cell membrane, electrode 8 is intact by the cell, and electrode 5, the common ground, is fully covered by the membrane. We measured impedance between seven pairs of electrodes with the common ground at electrode 5. We performed two sets of measurements: before and after culturing HeLa cells on top of MEA. Each time we swept the frequencies from 100 kHz to 100 MHz . We also simulated the experimental measurements with the FEM model for adherent cells described earlier. We grounded electrode 5 by applying the appropriate boundary condition and swept the working electrodes by setting a constant normal current density at the corresponding boundaries. We then calculated the complex impedance as the ratio between voltage at the working electrode and the applied electric current.

To build an appropriate FEM mesh, we extracted outlines of the cell membrane and nucleus shown as green and blue curves in Figure 2.11 (B) respectively. We applied our proposed geometry generation procedure to create 3D finite-element mesh depicted in Figure 2.11 (C).

We used previously described statistical models of dielectric properties of adherent cells to independently generate 10^6 samples of each variable. We then found their means, 97.5th and 2.5th percentile values and ran five sets of FEM simulations with these dielectric properties: mean values and four combinations of high and low conductivity and permittivity. To control

for correctness and ensure numerical convergence of FEM, we keep the mesh skewness > 0.1 , volume versus circumradius of the mesh > 0.01 , and the total size of the mesh $< 10^7$ degrees of freedom.

2.4 Results and discussion

Electrical response of biological cells is fundamental to many bio-medical studies. Modern methods model it with deterministic material properties and assume naive cellular geometries. Both assumptions cause misleading results. We approximate the diversity among cells using mixture of parametric models, built upon the data from 60 years of empirical research. We verified the proposed modelling approach with impedance spectroscopy measurements of a single HeLa cell. We believe that our model establishes theoretical foundations for fundamental stochastic mechanisms inside cell that impact its electrical properties. The proposed model extends to numerous bio-medical applications as it mimics biological diversity across different cell types and eliminates necessity for empirical parameter fitting. Nonetheless, a larger dataset can enable further analysis that may discover intricate relationships between cell components and associated molecular processes, while additional experimental verification may also improve the model in the future.

2.4.1 Electrical properties of cells

Adherent and non-adherent animal cells tend to have similar properties, while yeast cells and bacteria have thicker non-conductive membranes, but more conductive cytoplasm. Fundamentally, capacitance of the membranes is driven by the synthesis of phospholipid bilayers and attached proteins, which explains its tendency to follow log-normal distribution. Membrane conductance, on the other hand, follows gamma distribution, which can be driven by stochastic formation of the ionic channels and pores in the membrane. Conductivity of cytoplasm and nucleoplasm is best modelled by gamma distribution. It corresponds to accumulation of ions inside the cell, driven by the switching ion channels in the membranes. Presence of various proteins and organelles in cytoplasm and nucleoplasm causes log-normal

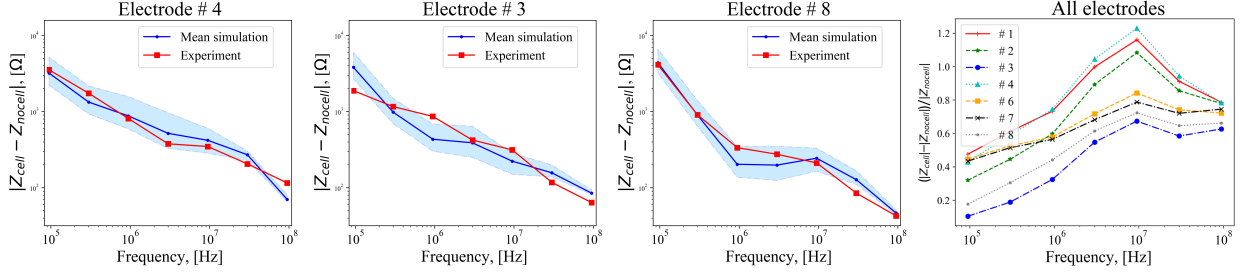


Figure 2.12: Electrical impedance spectroscopy of a single HeLa cell and FEM simulations distribution of their permittivity.

2.4.2 Electrical impedance spectroscopy of HeLa cell line

We plot measured electrical impedance difference $|Z_{cell} - Z_{nocell}|$ (red lines) versus frequency and analogous measures from FEM simulation with mean dielectric properties (blue line) in Figure 2.12. Empirical error bars extracted from measuring equipment specifications (worst-case uncertainty) were smaller than the markers on the plot, and, therefore, are omitted here. Shaded blue regions are bounded by simulations with 97.5th and 2.5th percentile values of the material properties. Comparing to the simulations, measured impedance had an identical decreasing trend. At frequencies below 1 MHz, when EDL dominates, we observed a rapid drop in impedance with a slope of $f^{-0.9 \leq slope \leq -0.5}$. In this regime, the major voltage drop is taking place at the double layer, which leads to horizontal current flow. With increase of the frequency, double layer becomes electrically transparent and β -dispersion takes place. This lets electric current to penetrate deeper inside the cell. The slope, therefore, continues dropping down and reaches $f^{-0.35}$ at 10 MHz. Region of 1 MHz to 50 MHz is of a particular interest as it brings Maxwell-Wagner effects. Primarily driven by the membrane polarization, normalized impedance peaks at 10 MHz. At the electrodes 1, 2, and 4, the effect is stronger, as they are located underneath the cell and its nucleus. At higher frequencies, a slope of $f^{-0.25}$ emerges implying the end of the β -dispersion region at 1 GHz.

CHAPTER 3

Electrical impedance tomography

Electrical impedance tomography (EIT) is a noninvasive imaging technique proposed by Webster in 1978 [41] and demonstrated by Barber and Brown in 1984 [42]. It was developed primarily for medical imaging in which the electrical properties (conductivity σ and permittivity ϵ) of a part of the body are inferred from the boundary measurements. Given that electrical properties vary considerably across biological tissues their spatial distribution defines shape and boundaries of the parts inside the body. Therefore, the reconstructed electrical properties form a tomographic image of the interior structure.

Compared to the conventional imaging techniques such as X-rays computed tomography (CT) or optical microscopy, EIT is entirely non-invasive and is based on a radiation-free "soft" excitation. In "hard" field imaging such as CT, pixels (or voxels) only locally affect the measurements. At softer X-rays, the effect of scattering needs to be taken into account leading to non-local effects. Non-locality makes image reconstruction in EIT particularly difficult as local changes in electrical properties may lead to global changes in measurements, which eventually results in lower imaging resolution. However, due to high portability, low-cost, and faster imaging capabilities EIT is being actively pursued.

A typical EIT measurement system contains a set of electrodes that are attached to the skin around the object being examined (see Figure 3.1). Then, a small alternating (AC) current is applied between a pair of electrodes, while the resulting potential distribution is captured by the voltage measurements on the remaining electrodes. Sometimes, a voltage stimulation and current measurements are used, which is fundamentally equivalent. This process is repeated for different pairs of electrodes to collect a set of electrical measurements that contains information about spatial distribution of the electrical properties. The goal of

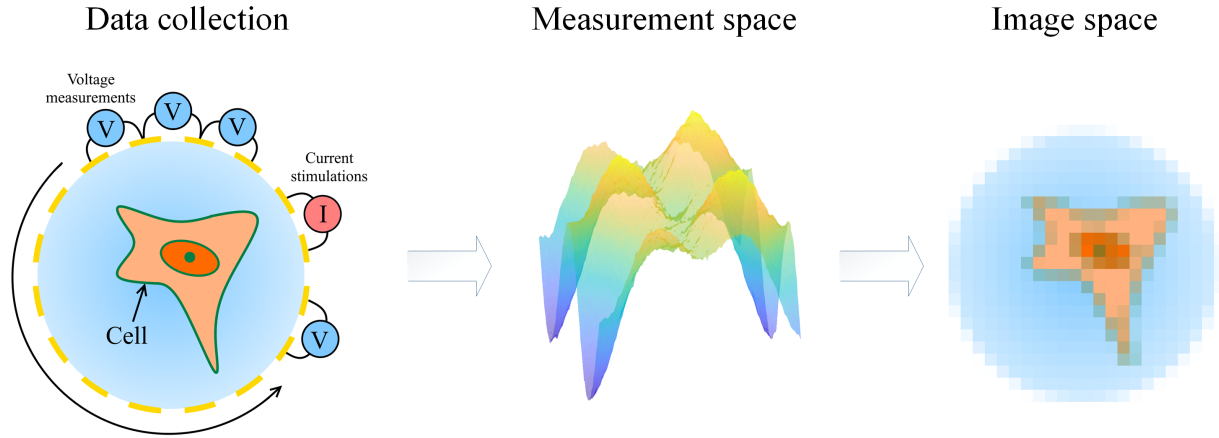


Figure 3.1: Steps in EIT image reconstruction: data collection with electrical measurements and mapping from voltage measurements to an image

image reconstruction is to find appropriate mapping between electrical measurements and the electrical properties that form an image.

The problem of recovering an admittivity distribution from measurement data, also called Calderon's problem, is non-linear and severely ill-posed. Specifically, for any measurement precision, there are arbitrarily large changes in the conductivity distribution that do not result in electric potential displacement. In other words, for a given set of measurements multiple possible solutions exist. To mitigate this, numerous methods were proposed, but most of them are aimed at including additional information about possible solutions. With sufficient *a priori* knowledge one can exclude meaningless solutions and separate the remaining ones so that the inverse problems could have a unique solution.

Mathematically, Calderon's problem was shown to have a unique solution if a complete relationship between voltages and the current is known. In practice, however, we can only have a finite number of electrodes of fixed sizes and, therefore, only an approximate solution is achievable. Another significant constraint stems from measurement noise and other sources of error. Given ill-posedness of the problem, a slight variation in the measurements heavily impacts image reconstruction. As a result, the inverse problem becomes numeri-

cally unstable. Popular algorithms such as backprojection, variational method, modified Newton-Raphson algorithm, Newton one-step error reconstruction (NOSER), and a maximum *a posteriori* (MAP) approach linearize the problem and introduce a regularization term to achieve numerical stability and convergence.

Practically, EIT imaging can be divided into three types: absolute imaging, frequency difference, and time difference. Absolute imaging simply maps measured signal to a spatial distribution of electrical properties. Often, however, a set of reference measurements is obtained before imaging an object. The relative changes between measurements of the body and the reference measurements are then mapped to an image, which is often called time difference imaging. When two sets of measurements are separated in frequency domain, frequency imaging takes places, which is particularly useful when electrical properties have a strong frequency dependence.

Originally, absolute and time difference EIT was proposed for human lung imaging. Particularly pulmonary emboli or blood clots detection in lungs raised interests in medical engineering community. Pulmonary emboli is a common serious complication of a surgery. In order to detect it, a sophisticated combination of conventional X-ray imaging with a preparation procedure was commonly practiced in hospitals. A patient was supposed to inhale radioactive gas followed by injection of a radio-opaque dye or a dissolved radioactive substance into a vein. Both procedures detrimentally affected patient's health and non-invasive methods were actively studied. In addition, EIT was proposed to detect accumulation of fluid in lungs, monitoring of heart function and blood flow, studying pelvic fluid, and enriching electrocardiograms and electroencephalograms. Later multi-frequency EIT found applications in cancer detection and localization in skin, breast, or cervix, as well as imaging of brain activity and gastrointestinal tract. Recently, micro-scale EIT applications emerged and several efforts on tissue and single-cell imaging were reported.

Although EIT is rather a niche imaging tool in medical practice, numerous measurement systems have been developed. The most widely used one is produced by Maltron International. It is a 16-electrode Mark system originally developed in Sheffield. Similar systems are the Goe MF II (16 electrodes) and Enlight 1800 (32 electrodes) developed at the University

of Gottingen and the University of Sao Paulo respectively. Such systems typically comply with medical safety standards and are primarily used by clinical research groups in hospitals and in intensive care.

3.1 EIT problem statement

To establish mathematical definition of the image reconstruction problem we first need to visit its first component - forward mapping $F : \Gamma \mapsto U$. The forward problem is used while solving the inverse problem by estimating the discrepancy between measurements V and predicted U due to error in γ . In addition, the forward mapping is used to estimate the Jacobian in several reconstruction algorithms.

Mathematical definition of the EIT problem is given by the Maxwell's equations:

$$\begin{cases} \nabla \times H = \gamma E \\ \nabla \times E = -i\omega\mu H \end{cases} \quad (3.1)$$

Given that the working angular frequency ω and the physical dimensions of the electrodes P are sufficiently small such that $\omega\mu |\gamma| P^2 \ll 1$, the curl of the electric field is usually ignored.

$$\begin{cases} \nabla \times H = \gamma E \\ \nabla \times E = 0 \end{cases} \quad (3.2)$$

Taking the Ohm's law $J = \gamma E$ and assuming the absence of the current sources and sinks in imaging domain Ω , we can yield:

$$\begin{cases} J = -\gamma \nabla u \\ \nabla^2 u = 0 \end{cases} \quad (3.3)$$

In practice, EIT usually employs a set of current excitations, which brings the corresponding Neumann boundary conditions:

$$\left\{ \begin{array}{ll} \gamma \frac{\delta u}{\delta n} = j, & \text{on electrodes } e_1 \dots e_L \\ \gamma \frac{\delta u}{\delta n} = 0, & \text{between electrodes} \\ \int_{e_l} \gamma(x, \omega) \frac{\partial u}{\partial n} ds = i_l, & \forall e_l, \\ \sum_{l=1}^L i_l = 0. \end{array} \right. \quad (3.4)$$

Electrode measurements V during the excitations I lead to additional Dirichlet boundary conditions. Note that the presence of the EDL at the electrode surfaces gives rise to contact impedance z_l for every electrode e_l , which leads to often called a complete EIT model [99].

$$\left\{ \begin{array}{l} u(x, \omega) + z_l \frac{\partial u}{\partial n} = v_l, \quad \forall e_l, \\ \sum_{l=1}^L v_l = 0, \end{array} \right. \quad (3.5)$$

Therefore, full mathematical formulation of EIT problem is given by 3.6:

$$\left\{ \begin{array}{ll} \nabla \cdot \gamma(x, \omega) \nabla u = 0, & \text{in } \Omega, \\ \gamma(x, \omega) \frac{\partial u}{\partial n} = j, & \text{on electrodes } e_1 \dots e_L, \\ \gamma(x, \omega) \frac{\partial u}{\partial n} = 0, & \text{between electrodes,} \\ \int_{e_l} \gamma(x, \omega) \frac{\partial u}{\partial n} ds = i_l, & \forall e_l, \\ u(x, \omega) + z_l \frac{\partial u}{\partial n} = v_l, & \forall e_l, \\ \sum_{l=1}^L i_l = 0, \\ \sum_{l=1}^L v_l = 0, \end{array} \right. \quad (3.6)$$

Despite being non-linear, a number of methods can be used to solve the forward problem. Finite difference method (FDM) uses a regular grid to discretize the domain and approximates the partial differential equations (PDE) with a system of difference equations. Its close relative, finite element method (FEM) approximates the space with arbitrary sized finite elements (usually, triangles in 2D or tetrahedrons in 3D), which gives a lot more flexibility in describing curved or smooth boundaries and domains (see Figure 3.2). Boundary element method (BEM) discretizes only surfaces of regions and employs analytical expression for

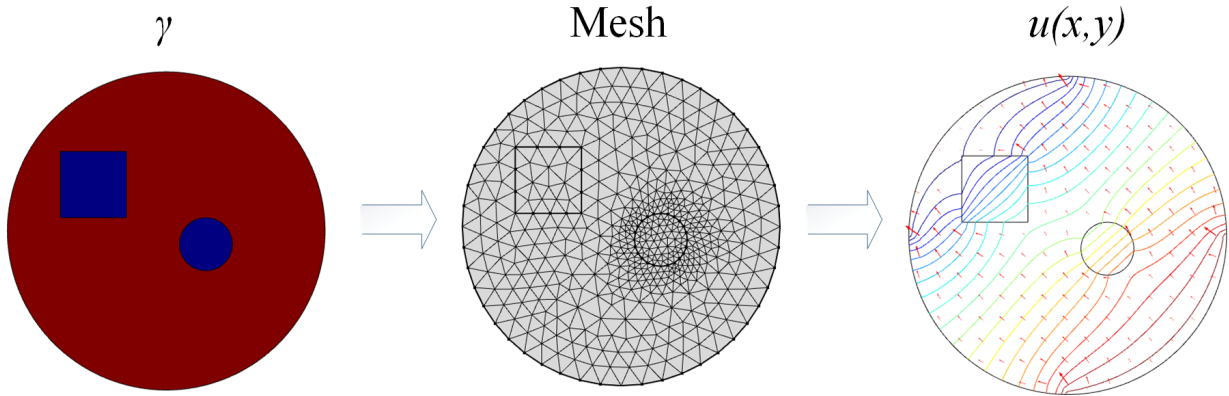


Figure 3.2: A solution to the forward problem based on FEM: admittivity distribution, space discretization using finite elements of adaptive size, response due to an excitation

the Green's function within enclosed volumes that are assumed to be homogeneous. BEM is computationally more efficient and is useful for EIT forward modelling when piece-wise constant electrical properties are assumed. In contrast to FEM and FDM, BEM results in a dense linear system and its computational advantage quickly diminishes with increase in degrees of freedom (DOF). BEM, however, has the advantage of being able to represent unbounded domains and may be superior in some applications. For example, a hybrid method where some regions assumed homogeneous and are represented by BEM demonstrated efficacy [100]. It is important to note, that the forward problem is usually well-posed and has guarantees for numerical convergence to a unique solution. As these numerical methods are not the primary matter for this work, we will further continue our discussion. More detailed introduction to FDM, FEM, and BEM can be found in the relevant literature such as [101, 102, 103, 104].

The second component of EIT problem, inverse mapping F^{-1} , corresponds to the reconstruction of γ given the stimulations I and the voltage measurements V at the boundary. Theoretically, infinitely many boundary measurements can be mapped to a unique γ , but practically the number of the measurements is usually limited, which makes this non-linear problem ill-posed and particularly difficult. Therefore the problem is frequently solved

through use of regularization. Tikhonov regularization, named for Andrey Tikhonov and also known as ridge regression, is a popular approach used in EIT and other ill-posed problems. In general, this method provides improved efficiency in parameter estimation problems in exchange for a tolerable amount of bias (loss in image resolution in EIT problem).

Let us consider a simple case where for a know A and b we want to find x that would satisfy:

$$Ax = b \tag{3.7}$$

When A is full-rank, a unique solution can be found using ordinary least squares $x_{OLS} = (A^T A)^{-1} A^T b$. However, most real-world forward mappings have the property of a low-pass filter which leads to loss of information and ill-posedness of the inverse problem. Therefore, several solutions may exist that satisfy 3.7. In order to give preference to a particular solution with desirable properties, a regularization term is added to the original least squares:

$$x_{Tikhonov} = \arg \min \|Ax - b\|^2 + \|Lx\|^2, \tag{3.8}$$

where L is Tikhonov matrix. Frequently this matrix is chosen as a multiple of the identity matrix, giving preference to solutions with smaller norm. In other cases, high-pass operators (e.g., a weighted Fourier operator or Laplace kernel) may be used to enforce smoothness of x . Tikhonov regularization improves the conditioning of the problem, thus enabling a direct numerical solution:

$$x_{Tikhonov} = (A^T A + L^T L)^{-1} A^T b. \tag{3.9}$$

A quantitative measure of ill-posedness can be measured with condition number:

$$k(A) = \|A\| \cdot \|A^{-1}\|, \tag{3.10}$$

where $\|\cdot\|$ for a matrix is defined as:

$$\|A\| = \max_{x \neq 0} \frac{\|Ax\|}{\|x\|} \tag{3.11}$$

Assuming that A is invertible and known accurately, $k(A)$ measures the amplification of relative error in the solution, or the worst case error bound:

$$\frac{\|\delta x\|}{\|x\|} \leq k(A) \frac{\|\delta b\|}{\|b\|} \tag{3.12}$$

A probabilistic view on image reconstruction problem gives another justification to Tikhonov regularization. According to Bayes theorem, the posterior probability is defined as:

$$P(x|b) = \frac{P(b|x)P(x)}{P(b)} \quad (3.13)$$

We can find optimal x by maximizing the posterior probability, which is called maximum *a posteriori* estimate (MAP). To achieve that, x is assumed to be Gaussian with mean x_0 and $\epsilon = Ax - b$ is also Gaussian with zero mean. Assuming independence of x and ϵ so that $P(b|x) = P(\epsilon)$ we can show that the posterior $P(x|b)$ is maximized as follows:

$$P(x|b) \propto \exp \left[- \|Ax - b\|^2 \right] \exp \left[- \|x - x_0\|^2 \right] \quad (3.14)$$

$$x_{MAP} = \arg \min \|Ax - b\|^2 + \|x - x_0\|^2.$$

3.2 Image reconstruction

A number algorithms for the inverse EIT problem have been proposed, including early approaches that assumed linear changes in γ such as backprojection [43] and variational [105] methods, and iterative non-linear methods such as modified Newton-Raphson algorithm [106], one-step Gauss-Newton (NOSER) [44], and MAP approach [107]. To improve the numerical stability of the inverse EIT problem, a variety of regularization strategies have been introduced. In particular, Tikhonov regularization [108] and the total variation (TV) [109, 110] methods became an integral part of the major EIT reconstruction methods. Further research efforts brought alternative methods with their own advantages and disadvantages. They include Kalman filter-based approach [111], Markov chain Monte Carlo (MCMC) optimization [112, 113], direct solver [114], and the D-bar algorithm [115]. A graphical example comparing different families of these algorithms is shown in Figure 3.3.

Approaching the problem with a non-linear iterative optimization is, perhaps, the most accepted method. In this case, the solution to the inverse problem is found by minimizing the square of the difference between the measured voltages V and the solutions to the forward problem $U = F(\gamma)$. Given that the problem may have multiple local minima the

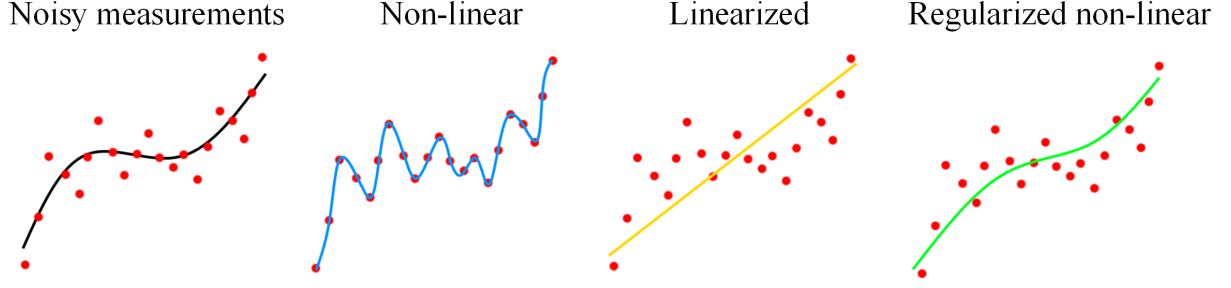


Figure 3.3: An illustration of how non-linear, linear, and regularized non-linear methods differ in a simplest case of fitting a function based on noisy samples

loss functional is usually extended with a regularization term as shown below:

$$\begin{aligned} \gamma &= \arg \min \mathcal{F}(V, U) \\ &= \arg \min \left[\|V - U\|^2 + \alpha \|L(\gamma_{prior} - \gamma)\|^2 \right] \end{aligned} \quad (3.15)$$

where α is a regularization coefficient, L is a matrix approximation of a smoothing operator, such as Laplace or Gaussian, γ_{prior} is the prior (reference) image.

The loss functional $\mathcal{F}(V, U)$ is then minimized through iterative updates:

$$\begin{aligned} \gamma_{t+1} &= \gamma_t - \delta\gamma \\ &= \gamma_t - \eta (J_t^T J_t + \alpha L^T L)^{-1} \cdot \\ &\quad \left[J_t^T (V - U) + \alpha L^T L (\gamma_{prior} - \gamma) \right] \end{aligned} \quad (3.16)$$

where J_t is the Jacobian matrix of the forward model estimated at step t , and η is the update step size. Additional damping factor yields Levenberg-Marquardt algorithm (also known as damped least squares) 3.17:

$$\begin{aligned} \gamma_{t+1} &= \gamma_t - \delta\gamma \\ &= \gamma_t - \eta (J_t^T J_t + \alpha L^T L + \lambda D)^{-1} \cdot \\ &\quad \left[J_t^T (V - U) + \alpha L^T L (\gamma_{prior} - \gamma) \right] \end{aligned} \quad (3.17)$$

where D is a diagonal matrix and is often chosen to be $D = \text{diag}(J_t^T J_t)$ to make the solution scale-invariant, and λ is the damping factor that decays to zero as the solution converges $\lambda_{t+1} = \arg \min_{\{\lambda_t, \lambda_t/\beta, \lambda_t \cdot \beta\}} \mathcal{F}(V, U)$ for an arbitrary scalar β .

A simplified version of the problem can be obtained through linearization:

$$F(\gamma_{t+1}) = F(\gamma_t) + J_t \cdot \delta\gamma \quad (3.18)$$

By replacing $\delta V = V - F(\gamma_t)$, the update becomes:

$$\delta\gamma = \eta(J_t^\top J_t + \alpha L^\top L)^{-1} [J_t^\top \delta V + \alpha L^\top L(\gamma_{prior} - \gamma_t)] \quad (3.19)$$

While there are many other forms of regularization possible for a linear ill-conditioned problem, this generalized Tikhonov regularization has the benefit that the *a priori* information it incorporates is made explicit and that under Gaussian assumptions it is the statistically defensible MAP estimate. If only a linearized solution is to be used with a fixed initial estimate γ_0 , the Jacobian J and a factorization of $J_t^\top J_t + \alpha L^\top L$ can be pre-calculated off-line. The efficiency of this calculation is then immaterial and the regularized solution can be calculated using the factorization with complexity $O(N^2)$ for N degrees of freedom in the conductivity (which should be smaller than the number of independent measurements) [116]. A popular image reconstruction algorithm, NOSER, that uses this scheme with a single update step is often used due to its efficiency.

Another way to mitigate numerical instability is regularization by total variation (TV). TV functional plays an important role in the regularization of inverse problems belonging to many disciplines. The use of such a functional as a regularization penalty term allows the reconstruction of discontinuous profiles. As this is a desirable property, the method gained popularity [116].

For a differentiable function of several variables on a domain Ω TV measures the total amplitude of the oscillations of the function:

$$TV(u) = \int_{\Omega} |\nabla u(x)| dx \quad (3.20)$$

In case when u is non-differentiable, TV is defined as:

$$TV(u) = \sup_{v \in \mathcal{V}} \int_{\Omega} u \operatorname{div} v \quad (3.21)$$

where \mathcal{V} is the space of continuously differentiable vector-valued functions that vanish on $\delta\Omega$ and $\|v\|_{\Omega} \leq 1$.

As the TV functional measures the variations of a function over its domain, it can be understood to be effective at reducing oscillations in the inverted profile, if used as a penalty term. The same properties apply, however, to L_2 regularization functionals. The important difference is that the class of functions with bounded total variation also includes discontinuous functions, which makes the TV particularly attractive for the regularization of non-smooth profiles [116].

3.3 Applications

As we mentioned before EIT is suitable for monitoring human thorax and particularly lungs because its tissue resistivity is five times higher than other soft tissues in the thorax. In addition, lung resistivity increases and decreases to a few orders of magnitudes during breathing. This also led to the most promising clinical application of EIT in monitoring of ventilated patients. The feasibility of EIT for lung imaging was first demonstrated in 1990 with the development of ultra-fast NOSER algorithm [44]. Time difference EIT was shown capable of visualization of the changes in the lung volumes and assistance in protective ventilation to patients in intensive care units. Absolute EIT is also a potential solution to clinical lung imaging, as this approach can help to distinguish between medical conditions which result in lower resistivity (*e.g.* hemothorax) and those with higher resistivity (*e.g.* pneumothorax). Besides applications in intensive care EIT can be combined with other imaging modalities. For instance, overlaying functional EIT images with morphological patient data (*e.g.* CT images) may be used in analysis of lung pathophysiology, which might be useful for patients suffering from obstructive lung diseases. Moreover, high temporal resolution of EIT allows assessment of common dynamic parameters used in pulmonary function testing. Recently, Dräger released PulmoVista 500, an EIT-based system aimed to support decision making processes on the treatment of patients with acute respiratory distress syndrome.

Another promising EIT application is imaging of breast cancer as an alternative or complementary technique to mammography and magnetic resonance imaging (MRI). Fundamentally, breast cancer detection is enabled by electrical properties of normal and malignant

breast tissue that differ due to changes in physical density and capacity of the tissues to conduct electric current. Another factor in favor of EIT is low specificity of the conventional methods a relatively high false positive rate that cause wrong medical decisions. Moreover, non-invasiveness of EIT would be particularly important to support health of the patients.

EIT has been also suggested to be used in brain imaging to detect and monitor cerebral ischemia, haemorrhage, and other morphological changes associated with neuronal cell swelling. While EIT has significantly lower resolution compared to cerebral CT or MRI, its temporal resolution is much higher, which makes EIT suitable for monitoring normal brain function and neural activity in intensive care units. Moreover, quick imaging of temporal changes in electrical properties at around 100 Hz might lead to novel EIT applications such as human-computer interfaces and robotic arm haptic sensors.

CHAPTER 4

Cell imaging with electrical impedance tomography

Cellular imaging is the primary engine in microbiology and one of the central problems in biomedical engineering. Despite recent advances in the field, the conventional fluorescent microscopy remains the most frequently practiced imaging technique. It is a repeatable, reliable, and commonly accepted method in cell studies, but it has several flaws arising from the need for optical excitation and use of fluorescent dyes. High-power ultraviolet (UV) and infrared (IR) light can damage DNA, raise cellular temperatures, and cause other photo-toxic effects [31, 32], while fluorescent dyes are frequently cytotoxic and can interfere with the results [33, 34]. A number of advanced optical techniques have been developed including coherence tomography [35] and projection tomography [36], but they suffer from poor penetration depth, high cost, and are difficult to scale down to a cell level. Micro-scale magnetic resonance imaging (MRI) on the other hand, requires very strong permanent magnets or additional injection of potentially toxic particles into the cells [37]. As a result long-term studies with live cells are hardly feasible with the conventional methods.

Several non-invasive methods based on electrical stimulation and sensing have been shown to be suitable for real-time and long-term applications. With a single pair of electrodes Givner and Keese developed electrical cell-substrate sensing [38], a robust *in vitro* technique that found applications in drug discovery, toxicity, phenotyping, and other studies [39, 40]. With additional pairs of electrodes, a more sophisticated analysis can be done. Proposed by Webster [41] and practically realized by Barber and Brown [42], electrical impedance tomography (EIT) deals with the reconstruction of the spatial distribution of electrical admittivity or conductivity. Assuming that different biological materials can be identified and characterized by their electrical properties, EIT delivers high penetration imaging for medical

and biological applications. On the other hand, the reconstruction is a hard ill-posed problem that requires additional assumptions and simplifications. From its inception researchers struggled with the development of reliable and inexpensive reconstruction algorithms. For instance, the commonly accepted approaches such as backprojection method [43] and Gauss-Newton algorithm [44] fail to deliver high resolution and may suffer from undesirable artifacts in the images, despite the strong assumptions such as linearity of the problem. Nonetheless, EIT has found applications in imaging of human thorax, brain, gastrointestinal tract, as well as, breast cancer screening [117, 118, 119, 120, 116].

Later, EIT was scaled down to *ex vivo* tissue electroporation imaging [45], cell culture imaging [46, 47], and single cell studies [48, 49, 51, 50]. In this chapter, we significantly extend EIT by tailoring it for cellular imaging. We first adjust measurement methodology. The traditional circular electrode array was originally developed for imaging of the human body and requires placement on the outer boundary of the object. This approach suffers from particularly low resolution at the center of the array caused by the absence of the interior electrodes and is practically infeasible at the scale of biological cells. We, therefore, propose an equally-spaced microelectrode array (MEA) along with the entire measurement system working at a wide range of frequencies. It is designed to enhance sensitivity for the cell imaging and takes advantage of the modern micro-fabrication technology. We then argue that a culture medium with cells is characteristically similar to a conductive domain with non-conductive inclusions. Hence, shape optimization methods could be applied to the problem. For example, image reconstruction was previously formulated as a shape identification task and shown to give stable numerical results [121]. By employing the notion of topological derivative [122, 123, 124] and level-set functions [125] researchers achieved more reliable and higher quality results in image reconstruction. Finally, we further modify the shape optimization method and include the *a priori* knowledge about the shape and unique electrical response of the cells, which drastically improves the algorithm’s stability and image quality. This makes the reconstruction algorithm tolerant to natural diversity among different cell types and enables high-contrast imaging by facilitating numerical convergence.

We validate the proposed methodology on a single-cell imaging of HeLa cell line. The

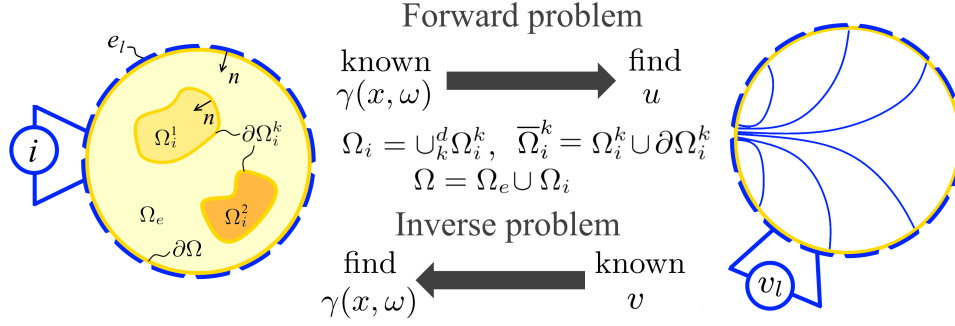


Figure 4.1: Electrical Impedance Tomography: forward and inverse problems

results promise real-time and long-term cellular imaging with an unprecedented image resolution. To compare the equally-spaced MEA design against the conventional circular MEA we estimated their performance on a set of simulated data that was designed to be numerically equivalent to each other. The results clearly demonstrate beneficial impact on the image quality. Then, we extensively benchmarked the proposed image reconstruction algorithm’s performance with a large-scale 3D simulated dataset and directly compared the results against the most commonly used alternatives. We report a high resolution single-cell EIT, a possible solution to one of the fundamental problems in microbiology and biomedical engineering.

4.1 Problem statement

EIT is a low-cost, non-invasive, and label-free imaging technique that employs difference in material properties to identify, localize, and reconstruct the objects. To get a reconstructed image, one needs to apply a sequence of electric current (or voltage) stimulations I between the electrodes placed around the region of interest Ω (see Figure 4.1). The image reconstruction involves measurement of electric potentials (or currents) V at the electrodes during the stimulations and solving a numerical optimization problem. The resulting image represents spatial distribution of the admittivity γ .

EIT has two distinct parts: the forward problem and the inverse problem. A solution to the former one is a potential distribution u for a given complex admittivity $\gamma = \sigma + i\omega\epsilon$ and

a stimulation i . It is well-defined and has a unique solution that can be found numerically with finite-element method (FEM). Mathematically, the forward problem is described by Laplace's equation that assumes no sources in Ω as shown below 4.1.

$$\left\{ \begin{array}{ll} \nabla \cdot \gamma(x, \omega) \nabla u = 0, & \text{in } \Omega, \\ \gamma(x, \omega) \frac{\partial u}{\partial n} = j, & \text{on electrodes } e_1 \dots e_L, \\ \gamma(x, \omega) \frac{\partial u}{\partial n} = 0, & \text{between electrodes,} \\ \int_{e_l} \gamma(x, \omega) \frac{\partial u}{\partial n} ds = i_l, & \forall e_l, \\ u(x, \omega) + z_l \frac{\partial u}{\partial n} = v_l, & \forall e_l, \\ \sum_{l=1}^L i_l = 0, \\ \sum_{l=1}^L v_l = 0, \end{array} \right. \quad (4.1)$$

where \vec{n} is an inwards unit normal, \vec{j} is an inwards current density, and z_l , i_l and v_l are the contact impedance (introduced to take into account the electrochemical effects at the electrode surface), current, and voltage at an electrode l .

The inverse problem corresponds to the reconstruction of γ given the stimulations I and the voltage measurements V at the boundary. Theoretically, infinitely many boundary measurements can be mapped to a unique γ , but practically the number of the measurements is usually limited, which makes this non-linear problem ill-posed and particularly difficult. To overcome these limitations, numerous algorithms have been proposed, including the early approaches that assumed linear changes in γ such as backprojection [43] and variational [105] methods, and iterative non-linear methods such as modified Newton-Raphson algorithm [106], one-step Gauss-Newton [44], and a maximum a posteriori (MAP) approach [107]. To improve the numerical stability of the inverse EIT problem, a variety of regularization strategies have been introduced. In particular, Tikhonov regularization [108] and the total variation (TV) [109, 110] methods became an integral part of the major EIT reconstruction methods. Further research efforts brought alternative methods with their own advantages and disadvantages. They include Kalman filter-based approach [111], Markov chain Monte Carlo (MCMC) optimization [112, 113], direct solver [114], and the D-bar algorithm [115].

4.2 Image reconstruction

The solution to the inverse problem is found by minimizing the square of the difference between the measured voltages V and the solutions to the forward problem U . Given that the problem may have multiple local minima the loss functional is usually extended with a regularization term as shown in 4.2:

$$\begin{aligned}\gamma &= \arg \min \mathcal{F}(V, U) \\ &= \arg \min \left[\|V - U\|^2 + \alpha \|L(\gamma_{prior} - \gamma)\|^2 \right]\end{aligned}\tag{4.2}$$

where α is Tikhonov regularization coefficient, L is a matrix approximation of a smoothing operator, such as Laplace or Gaussian, γ_{prior} is the prior (reference) image, and $\|\cdot\|$ is the vector norm operator.

The loss functional $\mathcal{F}(V, U)$ is often minimized through the iterative optimization:

$$\begin{aligned}\gamma_{t+1} &= \gamma_t - \delta\gamma \\ &= \gamma_t - \eta (J_t^T J_t + \alpha L^T L + \lambda D)^{-1} \\ &\quad \left[J_t^T (V - U) + \alpha L^T L (\gamma_{prior} - \gamma) \right]\end{aligned}\tag{4.3}$$

where J_t is the Jacobian matrix of the forward model estimated at step t , D is a diagonal matrix, η is the update step size, and λ is the damping factor which usually decays to zero as the solution converges. The optimization stops when the difference $V - U$ becomes smaller than the measurement error of the empirical measurements V . Note that when λ is large, 4.3 is equivalent to the Levenberg-Marquardt algorithm, while as $\lambda \rightarrow 0$ it becomes the Gauss-Newton method with Tikhonov regularization. We use the original strategy of scaling λ :

$$\lambda_{t+1} = \arg \min_{\{\lambda_t, \lambda_t/\beta, \lambda_t \cdot \beta\}} \mathcal{F}(V, U)\tag{4.4}$$

for $0 < \beta < 1$. In addition, to facilitate the convergence and make the solution scale-invariant we take $D = \text{diag}(J_t^T J_t)$.

4.2.1 *A priori* electrical cellular properties

As was previously reported [62], electrical properties of the culture medium, cell membrane, and cytoplasm can be represented with simple parametric models shown in Chapter 2. A naive approach to include the proper prior information about γ is to replace $\gamma_{prior} - \gamma$ with $1 - f_{prior}(\gamma)$ in 4.2, where f_{prior} is the appropriate parametric probability density function (PDF). Assuming linearity of the PDF for small $\delta\gamma$, this would yield another iterative algorithm 4.5:

$$\begin{aligned} \delta\gamma = \eta & \left(J_t^T J_t + \alpha g_{prior}^T L^T L g_{prior} + \lambda D \right)^{-1} \cdot \\ & \left[J_t^T (V - U) + \alpha g_{prior}^T L^T L (1 - f_{prior}(\gamma_t)) \right] \end{aligned} \quad (4.5)$$

where g_{prior} is the derivative of the f_{prior} estimated at γ_t . Similarly, if we take out the quadratic power from the regularization term, $\delta\gamma$ becomes:

$$\delta\gamma = \eta \left(J_t^T J_t + \lambda D \right)^{-1} \cdot \left[J_t^T (V - U) + \frac{\alpha}{2} L g_{prior} \right] \quad (4.6)$$

4.2.2 Maximum *a posteriori* estimation

Bayesian view on the image reconstruction suggests maximization of the posterior probability $p(\gamma|V)$ given by 4.7.

$$p(\gamma | V) \propto p(V | \gamma) \cdot p(\gamma) \quad (4.7)$$

Where the likelihood $p(V|\gamma)$ is determined by the forward model $F : \gamma \mapsto U$ and the measurement error. By estimating the error in measurements V , we can build the commonly accepted model that assumes additive Gaussian noise $V = F(\gamma) + \mathcal{N}(0, R_n)$ and linearity $F(\gamma + \delta\gamma) \approx F(\gamma) + J \cdot \delta\gamma$. If the prior $p(\gamma)$ is also assumed to follow $\mathcal{N}(\mu_\gamma, R_\gamma)$ [107] one can apply the iterative optimization 4.8:

$$\begin{aligned} \gamma_{t+1} = \gamma_{t+1} - \eta & \left(J_t^T R_n^{-1} J_t + \alpha R_\gamma^{-1} \right)^{-1} \cdot \\ & \left[J_t^T R_n^{-1} (V - U) + \alpha R_\gamma^{-1} (\mu_\gamma - \gamma_t) \right] \end{aligned} \quad (4.8)$$

We extend the MAP approach by bringing a more realistic $p(\gamma)$. As has been shown previously [62], cellular components can be described with a mixture of parametric models such as gamma, log-normal, uniform, and Gaussian. Following a similar derivation procedure

and using $\log(\gamma + \delta\gamma) \approx \log(\gamma) + \delta\gamma$ as $\delta\gamma \rightarrow 0$, we can show that for log-normally distributed γ with parameters μ_γ and R_γ the update $\delta\gamma$ is given by:

$$\begin{aligned} \delta\gamma &= \eta \left(J_t^\top R_n^{-1} J_t + \alpha R_n^{-1} \right)^{-1} \cdot \\ &\quad \left[J_t^\top R_n^{-1} (V - U) + \alpha R_\gamma^{-1} (\mu_\gamma - \log(\gamma_t)) - \alpha \right] \end{aligned} \quad (4.9)$$

Similarly, gamma-distributed γ with shape s_γ and rate r_γ yields 4.10, while, the uniform prior defined for $a_\gamma \leq \gamma \leq b_\gamma$ simply suggests maximization of the likelihood $p(V|a_\gamma \leq \gamma \leq b_\gamma)$.

$$\delta\gamma = \eta \left(J_t^\top R_n^{-1} J_t \right)^{-1} \left[J_t^\top R_n^{-1} (V - U) + \alpha (s_\gamma - r_\gamma - 1) \right] \quad (4.10)$$

4.2.3 Shape optimization

A simplified model of a cell is a cytoplasm enclosed by a thin membrane made of a lipid bilayer with embedded proteins. The cytoplasm additionally contains membrane-enclosed organelles that are involved in separate living activities. Cell membrane has regularly distributed ion channels - the pumps that maintain high ionic concentration inside the cell to support the internal biochemical processes. Cell membrane is, therefore, frequently modelled as a leaky capacitor. Hence, an individual cell differs significantly from the conductive culture medium and could be represented as an inclusion Ω_i^k with admittivity γ_i^k , while the surrounding medium can be described by $\Omega_e = \Omega \setminus \bar{\Omega}_i^k$. This extends the forward problem by 4.11:

$$\begin{cases} \gamma(x, \omega) = \gamma_i^k, & \text{in } \Omega_i^k, \forall k, \\ \gamma(x, \omega) = \gamma_e, & \text{in } \Omega_e, \\ u^- - u^+ = 0, & \text{on } \partial\Omega_i^k, \forall k, \\ \gamma_i(x, \omega) \frac{\partial u^-}{\partial n} - \gamma_e(x, \omega) \frac{\partial u^+}{\partial n} = 0, & \text{on } \partial\Omega_i. \end{cases} \quad (4.11)$$

Shape optimization methods have been previously considered to be used in EIT. In particular, a concept of topological derivative was proposed for reconstructing inclusions Ω_i [124]. By combining it with Gauss-Newton iterative optimization a more general image reconstruction case was demonstrated in [126, 122]. Second order shape optimization methods have been proposed to improve the numerical stability and further enhance image recon-

struction [127, 128, 123]. Similarly, level-set method was reported as another alternative to involve shape optimization into EIT [125].

The topological derivative $D_T(x, \Psi)$ of a loss functional $\mathcal{G}(\Psi)$ on a domain $\Psi \subset \Omega$ measures its sensitivity to a removal of an infinitesimal hole χ_ε of radius ε at location $x \in \Psi$:

$$D_T(x, \Psi) = \lim_{\varepsilon \rightarrow 0} \frac{\mathcal{G}(\Psi \setminus \bar{\chi}_\varepsilon) - \mathcal{G}(\Psi)}{Q(\chi_\varepsilon)} \quad (4.12)$$

where $\bar{\chi}_\varepsilon = \chi_\varepsilon \cup \partial\chi_\varepsilon$ and $Q(\chi_\varepsilon)$ is a positive function that decreases to 0 as $\varepsilon \rightarrow 0$. For instance, we can take $Q(\chi_\varepsilon) = \pi\varepsilon^2$ for two-dimensional reconstruction. For a small ε this yields:

$$\mathcal{G}(\Psi \setminus \bar{\chi}_\varepsilon) \approx \mathcal{G}(\Psi) + Q(\chi_\varepsilon) \cdot D_T(x, \Psi) \quad (4.13)$$

As was shown earlier [122], for the loss functional defined in 4.14 the topological derivative can be estimated with 4.15:

$$\mathcal{G}(\Psi, \gamma) = \int_{\partial\Omega} |V - U|^2 dl \quad (4.14)$$

$$D_T(x) = \begin{cases} \Re\left(\frac{4\gamma_i(x)(\gamma_i(x) - \gamma_e(x))}{\gamma_i(x) + \gamma_e(x)} \nabla u \nabla \bar{p}\right), & x \in \Omega_i \\ \Re\left(\frac{4\gamma_e(x)(\gamma_i(x) - \gamma_e(x))}{\gamma_i(x) + \gamma_e(x)} \nabla u \nabla \bar{p}\right), & x \in \Omega_e \end{cases} \quad (4.15)$$

where u is the solution to the extended forward problem 4.11 and p is the solution to the adjoint problem 4.16.

$$\left\{ \begin{array}{ll} \nabla \cdot \bar{\gamma}_e(x, \omega) \nabla p = 0, & \text{in } \Omega_e, \\ \nabla \cdot \bar{\gamma}_i(x, \omega) \nabla p = 0, & \text{in } \Omega_i, \\ \bar{\gamma}_e(x, \omega) \frac{\partial p}{\partial n} = V(x) - U(x), & \text{on electrodes } e_1 \dots e_L, \\ \bar{\gamma}_e(x, \omega) \frac{\partial p}{\partial n} = 0, & \text{between electrodes,} \\ \bar{\gamma}_i(x, \omega) \frac{\partial p^-}{\partial n} = \bar{\gamma}_e(x, \omega) \frac{\partial p^+}{\partial n}, & \text{on } \partial\Omega_i \\ p^- = p^+, & \text{on } \partial\Omega_i. \end{array} \right. \quad (4.16)$$

4.2.4 Cellular EIT reconstruction

Introduction of the inclusions Ω_i enables mixture modelling of the prior distribution $f_{prior}(\gamma_i) = \sum_j [\pi_{ij} f_{prior_j}(\gamma_i)]$, where π_i is an indicator vector that assigns each element γ_i to the cor-

responding components $\{f_{prior_j}\}$ such that $\sum_j \pi_{ij} = 1$. The simplest case of the cellular imaging contains two mixture components including culture medium Ω_e and the cells Ω_i . More sophisticated models can be constructed using prior distributions for the internal cell organelles, combinations of different cell types, and phases of the cell cycle.

We combine the shape optimization and the iterative algorithm into a two-step procedure: at any time-step t we first minimize $\mathcal{F}(\gamma)$ and then update Ω_i and π to minimize $\mathcal{G}(\gamma)$. Since $Q(\chi_\varepsilon) \geq 0$ in 4.13, adding inclusions at the locations $\{x_{add} : D_T(x_{add}, \Omega_e) < -C\}$ or removing inclusions at the locations $\{x_{remove} : D_T(x_{remove}, \Omega_i) > C\}$ for a positive real threshold C will lead to the decrease of $\mathcal{G}(\gamma)$, which is the original strategy proposed in [122]. Note that $\mathcal{G}(\gamma) \leq \mathcal{F}(\gamma), \forall \gamma$ and $\lim_{\alpha \rightarrow 0} \frac{\arg \min_\gamma \mathcal{G}}{\arg \min_\gamma \mathcal{F}} = 1$. Hence, the proposed reconstruction procedure belongs to the class of Majorization-Minimization (MM) algorithms and guarantees the convergence [129]. Empirically, we found that step-wise exponentially decreasing the threshold C enhances the numerical stability and convergence to the global minimum. Note, that the minimization of $\mathcal{F}(\gamma)$ can be achieved using any of the previously mentioned iterative optimization algorithms, but we empirically found that particularly stable results are achieved when we employ Laplace smoothing L (4.5 or 4.6) as well as MAP with the appropriate prior (4.8, 4.9, 4.10).

4.2.5 Complex admittivity

Usually EIT is used to reconstruct the real part of admittivity distribution $\sigma = \Re(\gamma)$ by applying DC current at the electrodes. However, cellular membrane that separates cell interior from the outer medium is distinguishable in both conductivity and permittivity, which makes complex EIT reconstruction more meaningful. Due to significant noise level and screening properties of the electrochemical interface at the microelectrodes, however, complex-valued measurements are prone to errors. On the other hand, the majority of impedimetric equipment perform measurements on a wide range of frequencies f . Having independent reconstructions $[|\tilde{\gamma}_1|, \dots, |\tilde{\gamma}_p|]$ based on absolute values of $[V_1, \dots, V_p]$ for a set of angular frequencies $[\omega_1, \dots, \omega_p]$ we can construct a set of linear equations 4.17. Note that we

assume negligible dependence of σ and ϵ on frequency ω , which is a reasonable assumption when the measurements are performed within a narrow band in between known dielectric dispersion frequencies [62].

$$\begin{cases} |\tilde{\gamma}_1|^2 = \tilde{\sigma}^2 + \omega_1^2 \tilde{\epsilon}^2 \\ \dots \\ |\tilde{\gamma}_p|^2 = \tilde{\sigma}^2 + \omega_p^2 \tilde{\epsilon}^2 \end{cases} \Leftrightarrow \begin{bmatrix} |\tilde{\gamma}_1|^2 \\ \dots \\ |\tilde{\gamma}_p|^2 \end{bmatrix} = \begin{bmatrix} 1 & \omega_1^2 \\ \dots & \dots \\ 1 & \omega_p^2 \end{bmatrix} \begin{bmatrix} \tilde{\sigma}^2 \\ \tilde{\epsilon}^2 \end{bmatrix} \quad (4.17)$$

Finally we can estimate σ and ϵ that minimize the sum of the squared discrepancies in $|\tilde{\gamma}_n|^2$ as shown below:

$$A = \begin{bmatrix} 1 & \omega_1^2 \\ \dots & \dots \\ 1 & \omega_p^2 \end{bmatrix} \quad (4.18)$$

$$\begin{bmatrix} \tilde{\sigma}^2 \\ \tilde{\epsilon}^2 \end{bmatrix} = [A^T A]^{-1} A^T \begin{bmatrix} |\tilde{\gamma}_1|^2 \\ \dots \\ |\tilde{\gamma}_p|^2 \end{bmatrix} \quad (4.19)$$

4.2.6 Equally-spaced microelectrode array

The commonly used circularly-arranged electrode array has several restrictions that make it inapplicable to the cell imaging. First, it has the fundamental resolution limit particularly restraining image quality at the center of the array [130]. Second, it is practically infeasible to bound a micrometer-scale domain containing cells. In order to overcome the aforementioned limitations and tailor EIT to the cellular imaging applications, we designed an equally spaced planar microelectrode array (MEA). Introduction of the internal electrodes mitigates resolution constraints at the center of the MEA [131, 102] while a regular pitch improves device sensitivity as it enables uniform probing of the electric potential changes due to presence of the cells. In general, planar electrodes require solving the unbounded (open) EIT problem [132], however, due to dominant horizontal current flow underneath the cells distant conductivity changes have negligible impact on the measured electrode voltages V_l [62] and we can still employ the original problem statement 4.1 while allowing electrodes placed inside Ω .

From a practical perspective, the planar MEA takes advantage of the latest developments in micro-fabrication and can be further scaled to a greater number of electrodes and integrated with solid state electronic devices to enable massive parallel *in vitro* assays.

4.3 Numerical evaluation

4.3.1 Evaluation of the proposed MEA design

To evaluate the proposed MEA design of equally-spaced planar electrodes we generated 1000 samples using 2D FEM that mimic adherent cells on the electrode arrays. Each sample was simulated on the circular arrangement (8 and 12 electrodes) and the equally-spaced arrangement (8 and 12 electrodes). A cell was approximated by an ellipse or union of two ellipses of varying sizes (6 - 20 μm) and conductivity of 0.3 mSm/m randomly placed between electrodes and surrounded by a conductive medium of 1 Sm/m (see Figure 4.2 A). For each sample, we kept the same size and the total number of the mesh elements to compare different electrode arrangements. As a reconstruction algorithms we employed 1-step Gauss-Newton difference method (NOSER) [44] and to measure the fidelity of the reconstruction, we used mean squared error (MSE) and multi-scale structural dissimilarity index (MS-DSSIM), which estimates perceived difference in the structure information of two images. To calculate MS-DSSIM, we normalized each ground truth image (difference against the background) and the reconstructed image to range of [0, 1], then, we found $(1 - MS-SSIM)/2$, where MS-SSIM is the multi-scale structural similarity index [133] between the ground truth and the reconstructed images. We discovered that the proposed MEA design benefit the image reconstruction both in MSE and MS-DSSIM (see Table 4.1). As was expected, with greater number of electrodes we obtained better reconstruction results.

4.3.2 Simulated cellular impedance tomography

To conduct a comprehensive comparison between different EIT algorithms, we collected a dataset of EIT measurements of adherent cells on an equally-spaced MEA. Each sample was

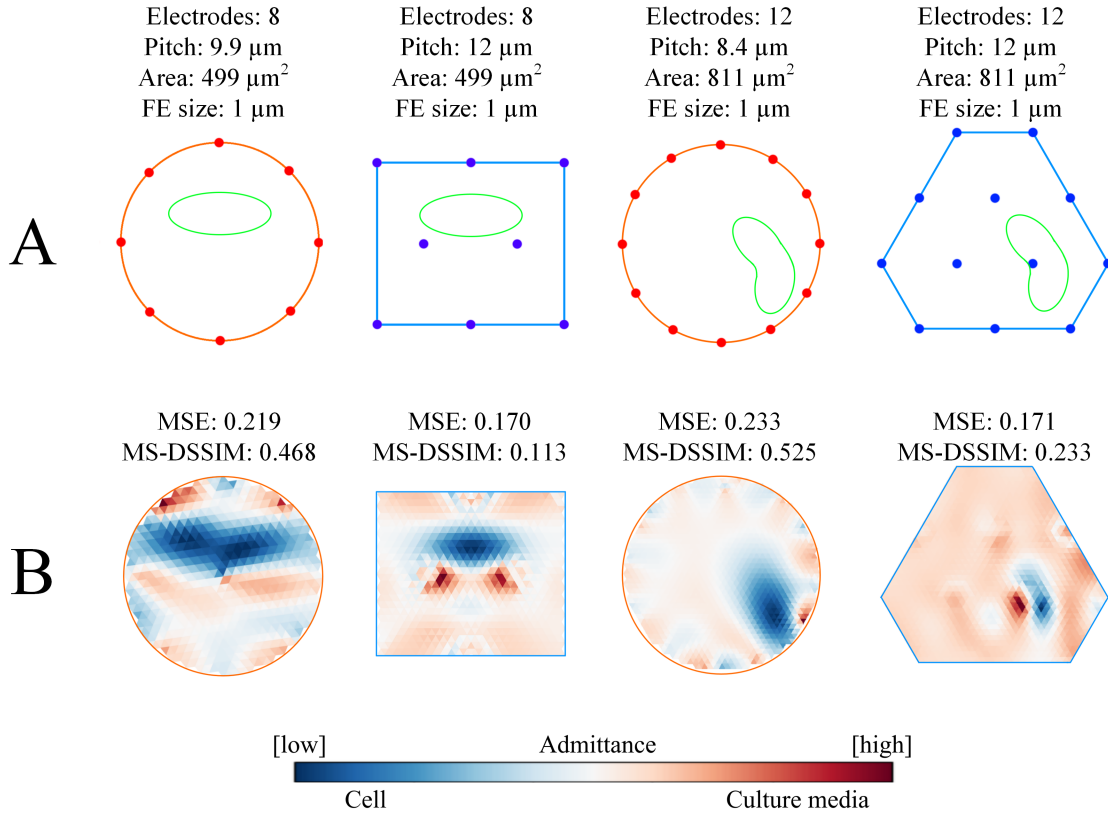


Figure 4.2: Sample of the MEA evaluation scheme: (A) simulated single cell (outlined with green) placed on equally-spaced 8- and 12-electrode MEAs (blue) and equivalent circular MEAs (red); (B) the corresponding reconstruction results

Table 4.1: Image reconstruction error (mean \pm std) for different MEA arrangements

MEA arrangement	MSE	MS-DSSIM
Circular (8-MEA)	0.1776 \pm 0.0898	0.0983 \pm 0.0911
Equally-spaced (8-MEA)	0.1368 \pm 0.0654	0.0751 \pm 0.0817
Circular (12-MEA)	0.1289 \pm 0.0908	0.0714 \pm 0.0580
Equally-spaced (12-MEA)	0.1035 \pm 0.0613	0.0535 \pm 0.0428

Table 4.2: Electrical properties of cell components used in the dataset generation

Property	Family	Parameters
Membrane capacitance, $\mu F/cm^2$	Mixture log-normal $\pi = \{0.6249, 0.3751\}$	$\mu_{log} = \{0.9430, -0.3745\}$ $\sigma_{log} = \{0.3713, 0.1833\}$
Membrane conductance, Sm/cm^2	Gamma	$shape = 0.1641$ $rate = 2.8960$
Cytoplasm permittivity	Log-normal	$\mu_{log} = 3.9857$ $\sigma_{log} = 0.3790$
Cytoplasm conductivity, Sm/m	Gamma	$shape = 4.0489$ $rate = 10.0158$
Nuclear envelope capacitance, $\mu F/cm^2$	Log-normal	$\mu_{log} = 0.0969$ $\sigma_{log} = 0.4330$
Nuclear envelope conductance, Sm/cm^2	Gamma	$shape = 1.5337$ $rate = 0.1180$
Nucleoplasm permittivity	Log-normal	$\mu_{log} = 4.1114$ $\sigma_{log} = 0.3756$
Nucleoplasm conductivity, Sm/m	Gamma	$shape = 2.3099$ $rate = 1.3536$
Medium permittivity	Normal	$\mu_{log} = 4.1114$ $\sigma_{log} = 0.3756$
Medium conductivity, Sm/m	Uniform	$shape = 2.3099$ $rate = 1.3536$

created with 3D finite-element simulations as was previously proposed [62]. In particular, we randomly generated realistic cell geometries at different adhesion stages. We used 50 geometries, each comprising of 1 - 4 cells (see examples in Figure 4.3 A). Random translations and rotations were introduced to augment the dataset. We used mean, 97.5th and 2.5th percentile values of the material properties distributed accordingly to the parametric models for adherent cells (see Table 4.2). We carefully evaluated FEM mesh in each simulation to ensure numerical convergence and data quality. In total, the dataset contained 10,000 unique samples for 8-electrode MEA and 10,000 unique samples for 12-electrode MEA.

We compared the proposed reconstruction algorithms, with a few conventional EIT methods including NOSER [44], MAP with Gaussian prior [107], Gauss-Newton method with the edge-preserving Laplace prior [134], Tikhonov regularization [108], and Primal Dual - Interior Point Method (PD-IPM) with TV regularization [110]. We employed EIDORS [135, 136],

Table 4.3: Image reconstruction error (mean \pm std) with 12 equally-spaced MEA and noiseless data

Algorithm	MSE	MS-DSSIM
NOSER [44]	0.1723 ± 0.0833	0.3045 ± 0.0416
MAP [107]	0.1462 ± 0.0693	0.3015 ± 0.0511
Tikhonov [108]	0.1399 ± 0.0635	0.2947 ± 0.0580
Laplace [134]	0.1187 ± 0.0436	0.2872 ± 0.0497
TV PD-IPM [110]	0.0868 ± 0.0174	0.2883 ± 0.0359
<i>MAP + Prior</i>	0.1217 ± 0.0592	0.2898 ± 0.0452
<i>Laplace + Prior L1</i>	0.1138 ± 0.0429	0.2789 ± 0.0497
<i>Laplace + Prior L2</i>	0.0977 ± 0.0333	0.2566 ± 0.0455
<i>TD + MAP + Prior</i>	0.0970 ± 0.0410	0.2352 ± 0.0184
<i>TD + Laplace + Prior L1</i>	0.0938 ± 0.0393	0.2455 ± 0.0261
<i>TD + Laplace + Prior L2</i>	0.0738 ± 0.0308	0.2171 ± 0.0079

a popular software toolkit that has the commonly accepted implementations of the aforementioned algorithms. A set of three-dimensional (3D) finite-element (FEM) simulations of EIT measurements with planar equally-spaced 12-electrode MEA underneath adherent cells was used to create a testing dataset for further estimation of the reconstruction performance. Note that the dataset was generated using realistic 3D cell geometries (see Figure 4.3 A) with dielectric properties that precisely mimic biological diversity from the previously proposed model in Chapter 2. The simulations particularly targeted a practical scenario of a virtually unbounded region with the cells cultured over the planar MEA. From each 3D simulated sample we extracted a 2D image that was depicting the cell shape from top down view similarly to observation in traditional microscopy. We found that reconstructing 2D images from the 3D simulated data is more challenging and generally ends in a bigger error, which is the reason of higher MS-DSSIM compared to the 2D simulated data that we used to evaluate different MEA arrangements. Interestingly, MSE did not show sensitivity to this challenge and was almost the same.

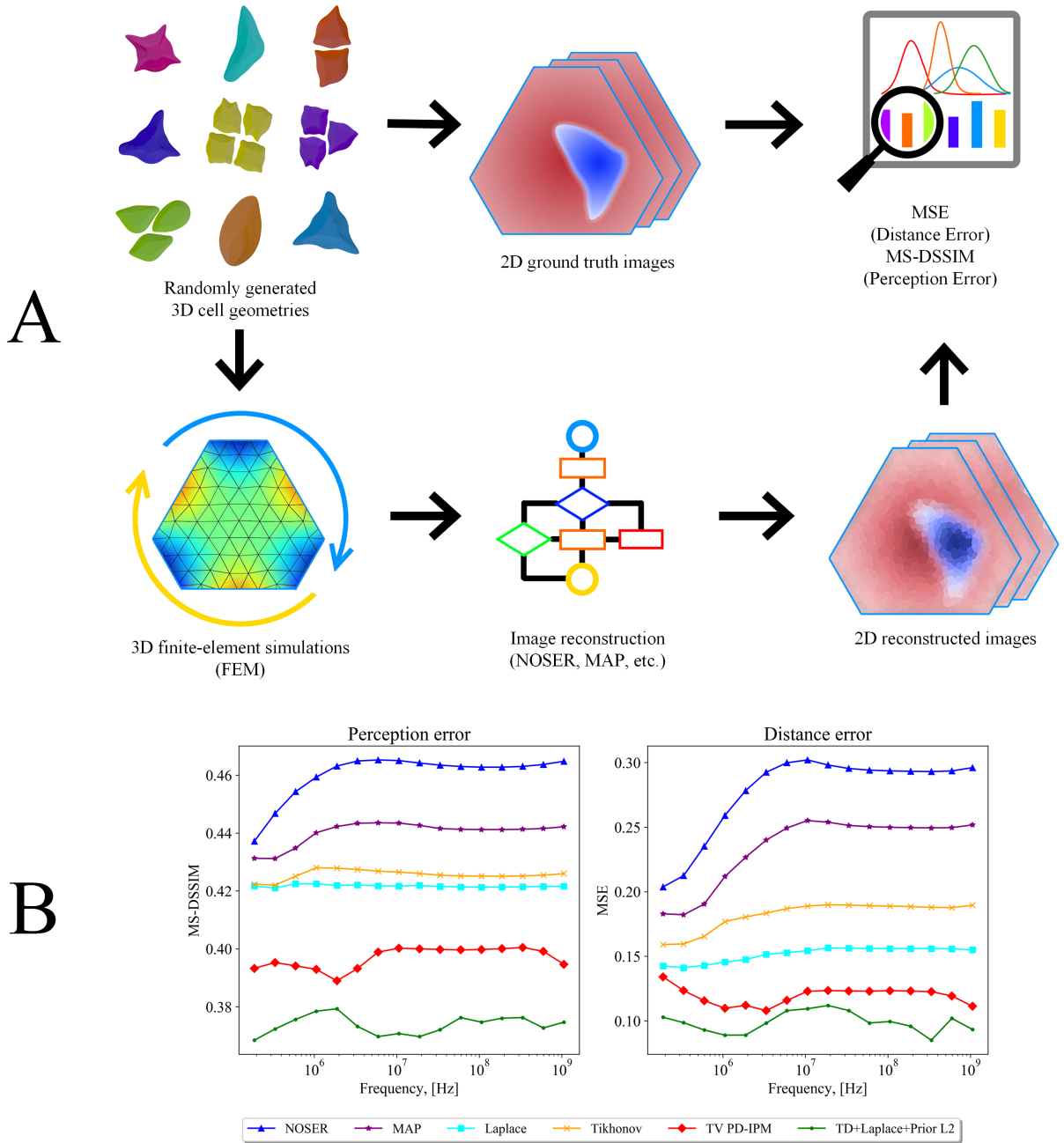


Figure 4.3: Evaluation of the proposed reconstruction algorithm on simulated data: (A) data generation and performance estimation; (B) reconstruction metrics at individual frequencies

Table 4.4: Image reconstruction error (mean \pm std) with 12 equally-spaced MEA and 20 dB data

Algorithm	MSE	MS-DSSIM
NOSER [44]	0.1698 ± 0.0806	0.3080 ± 0.0409
MAP [107]	0.1452 ± 0.0681	0.3016 ± 0.0519
Tikhonov [108]	0.1382 ± 0.0595	0.3049 ± 0.0556
Laplace [134]	0.1186 ± 0.0436	0.2872 ± 0.0499
TV PD-IPM [110]	0.1168 ± 0.0251	0.3089 ± 0.0380
<i>MAP + Prior</i>	0.1208 ± 0.0589	0.2899 ± 0.0455
<i>Laplace + Prior L1</i>	0.1137 ± 0.0429	0.2789 ± 0.0500
<i>Laplace + Prior L2</i>	0.0976 ± 0.0331	0.2566 ± 0.0470
<i>TD + MAP + Prior</i>	0.0964 ± 0.0407	0.2353 ± 0.0198
<i>TD + Laplace + Prior L1</i>	0.0937 ± 0.0384	0.2455 ± 0.0286
<i>TD + Laplace + Prior L2</i>	0.0787 ± 0.0309	0.2240 ± 0.0082

In Table 4.3 we report the mean and standard deviation of MSE and MS-DSSIM. The data show superior performance of the proposed reconstruction algorithms in both metrics. On the other hand, the reconstruction algorithms struggle to generate a perfectly reconstructed image. This could be caused by the differences between the simulated unbounded 3D geometries and bounded 2D reconstruction region, which also clearly shows the complexity of the inverse problem. To further improve the realism of the testing and evaluate the algorithms stability we mixed the simulated measurements with additive Gaussian noise assuming pessimistic 20 dB signal-to-noise ratio (SNR). As Table 4.4 suggests, the proposed algorithms demonstrate insignificant degradation, while TV PD-IPM becomes substantially worse in both MSE and MS-DSSIM. Interestingly, that other methods withstand the noise well and produce results similar to the noiseless case. When we took a closer look at the reconstruction performance at each stimulation frequency (see Figure 4.3 B), we discovered that the proposed algorithm (TD + Laplace + Prior L2) consistently outperforms the others. On the other hand it has noticeable fluctuations along the frequencies, which could be

caused by inconsistent topological derivative estimation that sometimes fails to find new candidates for the inclusions and hints for future optimization of the parameters of the proposed algorithm.

4.4 Experimental verification

We designed MEA of eight golden and transparent electrodes with pitch of $12\ \mu\text{m}$. MEAs were fabricated at Nanoelectronics Research Facility at UCLA. To make golden electrodes, layers of $20\ \text{nm}$ of Ti and $100\ \text{nm}$ of Au were vacuum-evaporated on fused silica wafers ($100\ \text{mm}$ in diameter) and the electrodes were patterned with the conventional lift-off process. To make transparent electrodes, a layer of $120\ \text{nm}$ of indium tin oxide (ITO) was sputter-deposited on fused silica wafers ($100\ \text{mm}$ in diameter) and the electrodes were patterned with reactive-ion etching. On top of the electrodes we deposited a passivation layer of $500\ \text{nm}$ of silicon dioxide with plasma-enhanced chemical vapor deposition (PECVD). To pattern the passivation layer, we employed deep reactive ion etching. We made circular openings of $4\ \mu\text{m}$ in diameter at the center of the MEA and square contact pads of $5\ \text{mm}$ at the edges. The wafer was diced into 25-by-25 mm square dies and each of them was cleaned in ultrasonic bath of acetone with subsequent deionized water wash, nitrogen blow and thermal dehydration. On top of the MEAs we designed 500 microliter (μL) wells of polydimethylsiloxane (PDMS) to allow long-term cell culturing. In addition, MEAs were connected to the intermediate printed-circuit board (PCB) with conductive silver epoxy adhesive (MG Chemicals). The intermediate PCB was connected to switching PCB that contained analog multiplexers and interfaces for vector network analyzer (VNA, HP 8753ES) and a computer. The computer was used to control stimulation power of the VNA, switch between the electrodes, and fetch data via General-Purpose Interface Bus (GPIB, Agilent 82357B).

To empirically verify the integrity of the proposed cellular EIT we conducted several experimental measurements of human cervical carcinoma (HeLa) cells. Cells (HeLa AC-free, Sigma-Aldrich) were grown at $37\ ^\circ\text{C}$ in Dulbecco's Modified Eagle's Medium (DMEM) supplemented with 10% fetal bovine serum (FBS) and $100\ \text{units}/\text{mL}$ penicillin, and $100\ \mu\text{g}/\text{mL}$

streptomycin (PS). Cells were regularly passaged to maintain exponential growth. Twenty-four hours before staining and electrical measurements, we trypsinized HeLa cells, diluted them 1 : 5 with fresh DMEM medium without antibiotics, centrifuged, and suspended into fresh DMEM with 10% FBS and 1% PS. Then, we transferred 10 μL of the cell suspension ($2 \cdot 10^5$ *cells/mL* concentration) to the MEA device with the attached PDMS well (500 μL). To enable the long-term incubation we added 390 μL of fresh DMEM medium with 10% FBS and 1% PS and left the cells in the incubator for 24 hours at 37 °C and 5% CO₂. The cells appeared healthy and attached thereafter. During the incubation, the entire assembly of MEA, PDMS well, and the intermediate PCB was enclosed in a small vented Petri dish. After the incubation, the well was gently desiccated and washed with DMEM medium. To stain the cell nuclei, we added 20 μL of 2 $\mu g/ml$ Hoechst 33342 (Invitrogen) solution and incubated the cells for 25 minutes at 37 °C. We then gently desiccated the well and washed it with DMEM medium. To stain the cell membrane, 20 μl of 5 $\mu g/ml$ of WGA Alexa Fluor®488 conjugate (Invitrogen) solution were added, and cells were incubated for another 10 minutes at 37 °C. After the last incubation, the well was gently desiccated, washed, and filled with a fresh DMEM medium with 10% FBS and 1% PS. We imaged the cells with fluorescent microscopy before and after the electrical measurements and observed no visible changes in structure, shape, and location caused by the electrical measurements.

4.4.1 Single-cell imaging of HeLa cell line

To empirically verify the integrity of the proposed cellular EIT we conducted several experimental measurements of human cervical carcinoma (HeLa) cells. We designed a measurement system that can handle arrays up to 16 microelectrodes, although for this experimental study we used 8-MEA with 12 μm pitch between the electrodes. On top of the device, we built a 500 microliter (μL) well of polydimethylsiloxane (PDMS), which is sufficient for the majority of long-term studies with adherent cells (see Figure 4.4 A). The electrodes are covered by a thin passivation layer with small openings at the tips of the electrodes. The device is connected to printed-circuit boards (PCB) that are dynamically routed to a vector network analyzer (VNA). Transparent substrate of the device allows light to go through and gives

flexibility to easily integrate with inverted microscopes.

We confirmed successful reconstruction with transparent (Figure 4.5 A, B) and non-transparent (Figure 4.5 C) 8-electrode MEA. We qualitatively compared the reconstructed results against the fluorescent images (shown in white on the grayscale images) of the cell membranes, that correspond to the outer boundaries of the cells. The reconstructed images depict spatial distribution of absolute admittivity with high values (low impedance) represented in red and low values (high impedance) represented in blue, hence, the blue regions denote the cells.

Figure 4.5 A captures a partial coverage, where only one electrode at the edge of the 8-MEA is completely covered by the cell membrane as indicated on the fluorescent microscopy image. The blue region in the corner of the image reconstructed by the proposed algorithm (TD + Laplace + Prior L2) accurately depicts the shape, size, and the location of the cell membrane. Despite having only one electrode covered by the cell membrane, the topological optimization step of the reconstruction algorithm managed to recover the inclusion at the edge of the reconstruction domain (the outlined blue box). A closer look at the gradient of the blue region suggests an increase of the electrical impedance, which could be a measure of the strength of the cell adhesion or the thickness of the cell membrane that blocks lateral and vertical current flows. Noticeable conductivity artifacts in the center of the reconstruction domain, a well-known weakness of EIT, could be caused by the noise in the measurements and substantially large contact impedance at the central electrodes.

On the other hand, when we substituted Laplace-smoothed iterative optimization step with the maximum a posteriori (MAP) optimization, the inclusion was misidentified (TD + MAP + Prior). Detailed analysis showed that it stems from the initial guess on the admittivity distribution by the MAP step that later caused the errors in the shape optimization (TD), which escalated the problem further. The root cause is, however, the noise in the measurements that made MAP to compensate by smoothing the image at the center and moving the blue inclusion away from the edge. The conventional Gauss-Newton reconstruction with Laplace smoothing also failed in estimating of the boundaries and shape of the cell (Laplace). We found that reducing regularization hyperparameter produced smaller blue

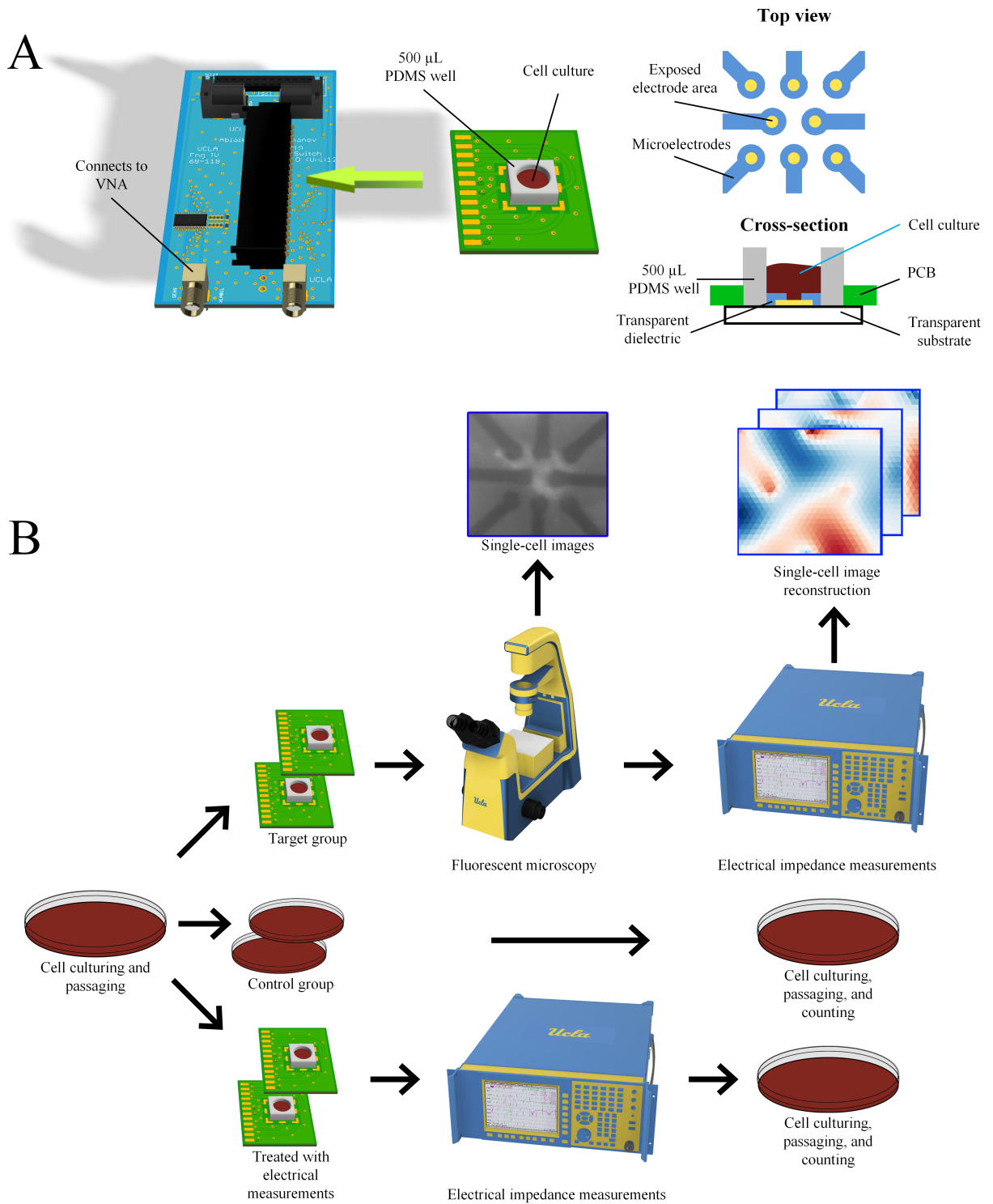


Figure 4.4: Diagrams of (A) the measurements system and (B) experimental methodology

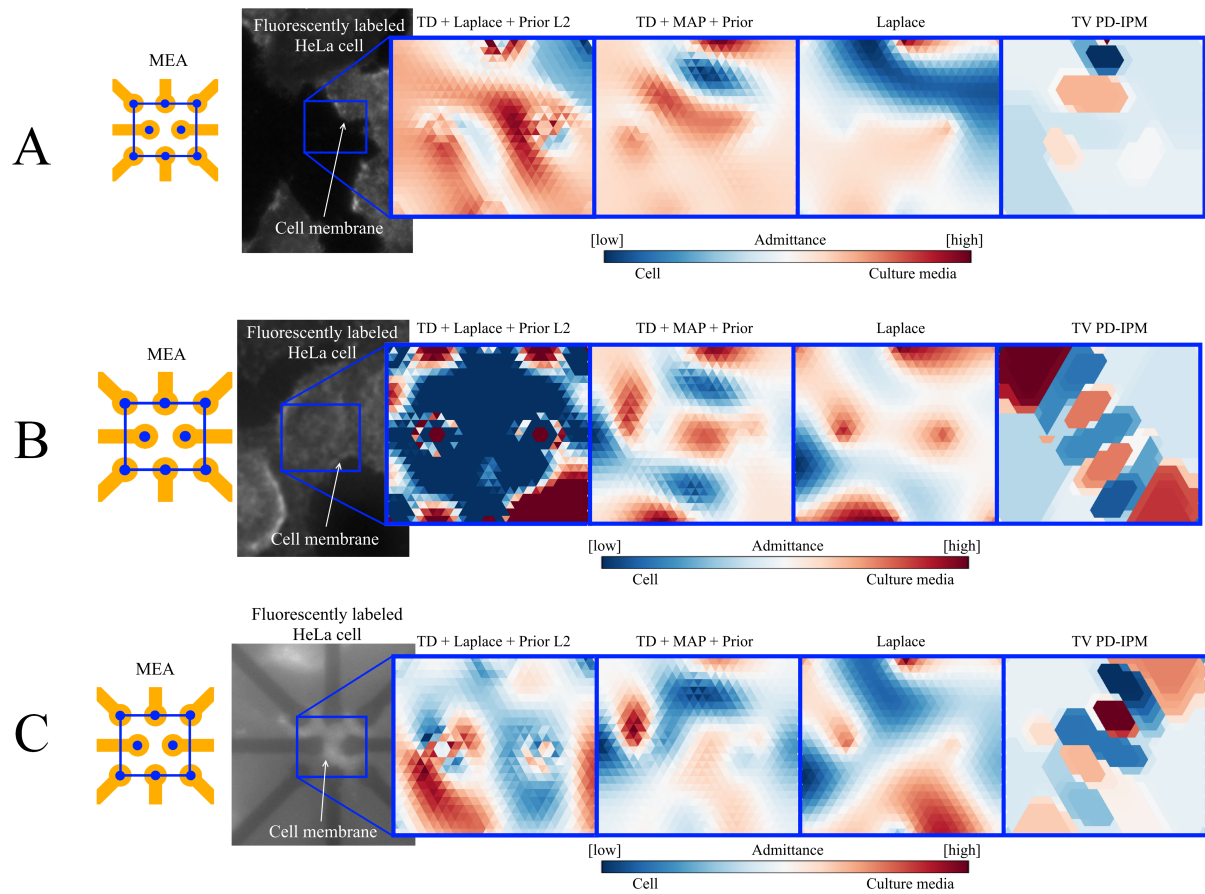


Figure 4.5: Cellular EIT of HeLa cells compared against fluorescently labeled cell membrane: (A) partial coverage, (B) almost complete coverage, and (C) gold MEA

region at the top right corner of the image, but at the same time brought large artifacts at the other corners of the image. Interestingly, that a popular EIT reconstruction algorithm based on total variation regularization (TV PD-IPM), particularly suited for high contrast imaging, similarly to the MAP approach moved the cell location away from the edge to compensate for the noise at the central electrodes.

Figure 4.5 B brings a more sophisticated situation where a single cell almost completely covered the entire MEA, which allowed us to reconstruct the image directly underneath the cell. The proposed approach (TD + Laplace + Prior L2) produced the image that appears predominantly blue as the cell blocks the current flow in all directions. Several red spots at the edges and at the center of the image could suggest spatial variance in cell adhesion driven by the cell motility and formation of the membrane protrusions. On the other hand, they could be caused by the measurement noise, presence of electric current paths outside of the reconstruction domain, and sub-optimal hyperparameter choice for the algorithm leading to the convergence to a local minimum. The right corner at the bottom of the reconstruction domain, however, is properly colored in red representing an open spot not covered by the cell. The reconstructed sample also demonstrates the ability of the proposed algorithm to recover high contrast images, which is of the utmost importance for cellular imaging and was a long-standing challenge in EIT.

Replacing the iterative optimization with the MAP estimation (TD + MAP + Prior) once again leads to the failure mode of the shape optimization step. In particular, the small blue inclusions at the center of the MEA failed to merge due to presence of the red regions of high conductivity in between. Unfortunately, further tuning of the hyperparameters of both MAP and TD steps led to emergence of additional artifacts on the image. Comparable reconstruction results were achieved through Laplace-smoothed Gauss-Newton optimization (Laplace), which stresses the need for the shape optimization and specific tuning for cellular imaging. TV PD-IPM method also suffered from large artifacts at the center and at the top left corner. Presumably, these methods are limited by the measurement noise and additional current flows outside the reconstruction domain that lead to artifacts on the images.

Another example of a single cell EIT is depicted in Figure 4.5 C. Although the microscopy

image was partially obscured by the gold 8-MEA, we could still compare the reconstructed image against the fluorescently labeled cell membrane. As these electrodes have lower contact impedance compared to the transparent ones, the cell appears in light blue, while the areas without the cell are correctly reconstructed in red. Once again, we were able to recover the shape and the location of the cell and pick up several slightly more conductive spots underneath the cell using the proposed image reconstruction algorithm (TD + Laplace + Prior L2). While few different explanations are possible, we presume that the red regions inside the blue inclusion are driven by the cell motility mechanisms that alternate cell adhesion and the electrical impedance underneath it. We also found that the gold electrodes are less prone to artifacts at the edges of the reconstruction domain.

As with the transparent MEA, MAP estimation significantly constrains the shape optimization and leads to erroneous results (TD + MAP + Prior). Once MAP gets into a locally convex region of the loss function the topological derivative is either insufficient to escape it or further worsens the problem by approaching to a local minimum. Suffering from the same issue Laplace optimization produced an image of similar topology and nature. Unfortunately, TV PD-IPM algorithm was not able to catch the cell shape, location, or size, despite a thorough hyperparameter search. Generally, we noticed that traditional EIT reconstruction methods particularly struggle with the cases where a significant portion of the reconstruction domain is covered by the cells, which can dramatically limit their applicability and shows the importance of the proposed changes that tailor EIT to cellular imaging.

To investigate how electrical stimulations induced by the measurements system affect cell proliferation and viability, we had two additional groups of cells. The first (control) group was cultured in a culture dish for one day, while the second (treated) group was cultured on the devices for one day and then was subject to the electrical stimulations (see Figure 4.4). Both groups were later cultured for two days and then transferred to a dish for hemocytometer cell counting and estimating of the doubling time. Despite being exposed to the electrical field, the treated cells looked healthy and attached all the time and were virtually indistinguishable from the control group. The average doubling time of the both groups was around 19 hours.

4.4.2 Discussion

Cellular imaging is one of the central problems in biomedical engineering. Although the conventional fluorescent microscopy remains popular in the field, it severely limits the long-term studies due to cytotoxic effects of the labeling dyes. EIT, on the other hand, is based on label-free non-invasive electrical stimulations and has been previously proposed for cellular imaging. The technique, however, was originally developed for the applications in human body imaging and has insufficient resolution for cell research. We extended EIT to single-cell imaging and designed a novel device. To enhance image quality we proposed a two-step image reconstruction algorithm that exploits the unique topology of the problem. Introduction of the *a priori* known material properties of the cells improved numerical convergence and made it resistant to noise and biological diversity.

Cellular EIT fills the gap in rapid non-invasive long-term cellular imaging. The experimental results show the first high-resolution impedance-based imaging of a single cell that captures the slightest changes underneath the cell that are unobservable in the conventional optical microscopy. As the impedance underneath the cell very sensitively responds to changes in cell thickness and cell adhesion, cellular EIT can drastically extend biomedical studies such as cytotoxicity, drug development, phenotyping, cell motility, and so on. Due to simple physical structure the proposed device could further evolve into a lab-on-a-chip platform for large-scale simultaneous single-cell assays that could be used along with optical microscopy or as a standalone imaging method.

CHAPTER 5

Deep learning in inverse problems

Homo sapiens, you and me, we are basically the same as people 10,000 years ago. The next revolution will change that

Yuval Noah Harari

Over the last few decades machine learning and, particularly, deep learning demonstrated extraordinary results across numerous tasks [137]. The list includes long-standing problems in computer vision, natural language understanding, and applied fields such as health care, self-driving cars, surveillance, and so on [138]. In this chapter we are going to quickly introduce the basic components of deep learning methods and discuss their applicability to inverse problems. A more thorough introduction to the topic can be found in [139, 140, 141].

5.1 The elements of deep learning

Deep learning belongs to a broad family of machine learning methods and is based on artificial neural networks (ANNs). ANNs are loosely inspired by biological neural networks and are built with units (sometimes called neurons) that perform simple mathematical operations on their inputs. The exact form of these operations are defined by the network architecture and the corresponding trainable parameters. Connections between the units form a directed graph, often acyclic. Units are grouped in a larger abstraction, called layer, which also serves as a standard building block in deep learning and simplifies ANN visualization. The adjective "deep" comes from cascading multiple layers in ANN that increases the depth of the graph.

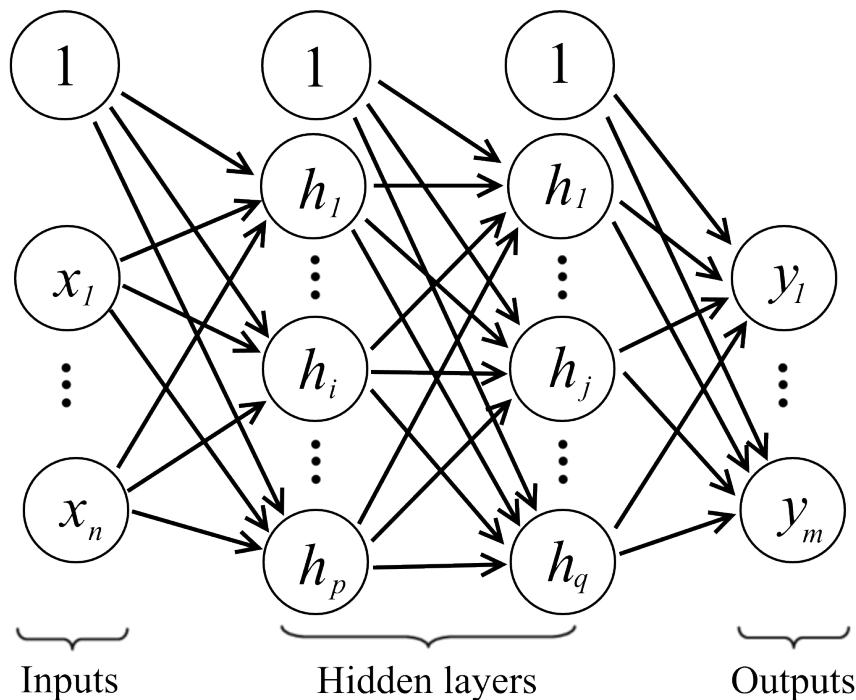


Figure 5.1: Feed-forward neural network

Adding layers leads to a higher capacity of a network, but brings difficulties during model fitting. Model fitting (often called training) is an optimization procedure that minimizes a loss functional (e.g. mean squared error, mean absolute error, binary crossentropy, and so on) using an optimization algorithm such as gradient descent. A popular choice among today is Adam algorithm [142], which is based on stochastic gradient descent with momentum.

5.1.1 Core building blocks

Deep feed-forward network (also called multi-layer perceptron or MLP), is an essential model in deep learning. It approximates an arbitrary function $f^*(x) = y$ by defining a mapping $\tilde{f}(\theta) : x \mapsto y$. Trainable parameters θ are learned to best approximate the function f^* . Intermediate (also called hidden) layers in MLP are connected to every unit from a previous layer and are parameterized by dense matrices W (see Figure 5.1), which is why these layers are commonly called dense. The parameter matrices W are trainable and simply represent the weights of the edges in the network graph.

Fundamentally, MLP could have as many hidden layers as possible. Hence, mathematically MLP represents a composition of functions $\tilde{f} = (f_r \circ \dots \circ f_k \circ \dots \circ f_1)(x)$. A dense layer k takes the inputs Z_{k-1} and linearly combines them using the weight matrix $f_k(Z_{k-1}) = W_k \cdot Z_{k-1}$. The weight matrix W_k additionally contains trainable bias terms (shown with the edges connected to constant unit nodes in Figure 5.1). Therefore, Z_{k-1} is formed by concatenation of a constant unit node 1 and the outputs of the previous layer $k - 1$.

In many practical problems the function of interest f^* is non-linear and to make ANN capable of fitting f^* a non-linear activation function is applied on top of the outputs of each unit. In early days, logistic function $\sigma(x) = \frac{e^x}{1+e^x}$, hyperbolic tangent $\tanh(x) = \frac{e^x - e^{-x}}{e^x + e^{-x}}$, softmax $s(x)_i = \frac{e^x}{\sum_k e^x}$, and linear rectifier $ReLU(x) = \max(0, x)$ were among the most popular activation functions. To avoid vanishing gradient problem and other issues appearing in deep models, however, a more robust activation functions became popular, such as parametric ReLU (PReLU), exponential linear unit (ELU), and scaled exponential linear unit (SELU):

$$\begin{aligned}
 PReLU(x) &= \begin{cases} x, & \text{if } x \geq 0, \\ ax, & \text{if } x < 0 \end{cases} \\
 ELU(x) &= \begin{cases} x, & \text{if } x \geq 0, \\ a(e^x - 1), & \text{if } x < 0 \end{cases} \\
 SELU(x) &= \begin{cases} bx, & \text{if } x \geq 0, \\ ab(e^x - 1), & \text{if } x < 0 \end{cases}
 \end{aligned} \tag{5.1}$$

Convolutional neural network (CNN) is another type of feed-forward networks, where the connections between subsequent layers are sparse. CNN were originally inspired by biological visual cortex and often used in computer vision problems. Although a fully connected neural network or MLP with a large number of neurons and a single hidden layer has the ability to approximate any function, provided our activation functions satisfy some weak assumptions, CNN is often favored in many applications. When dealing with highly structured modalities

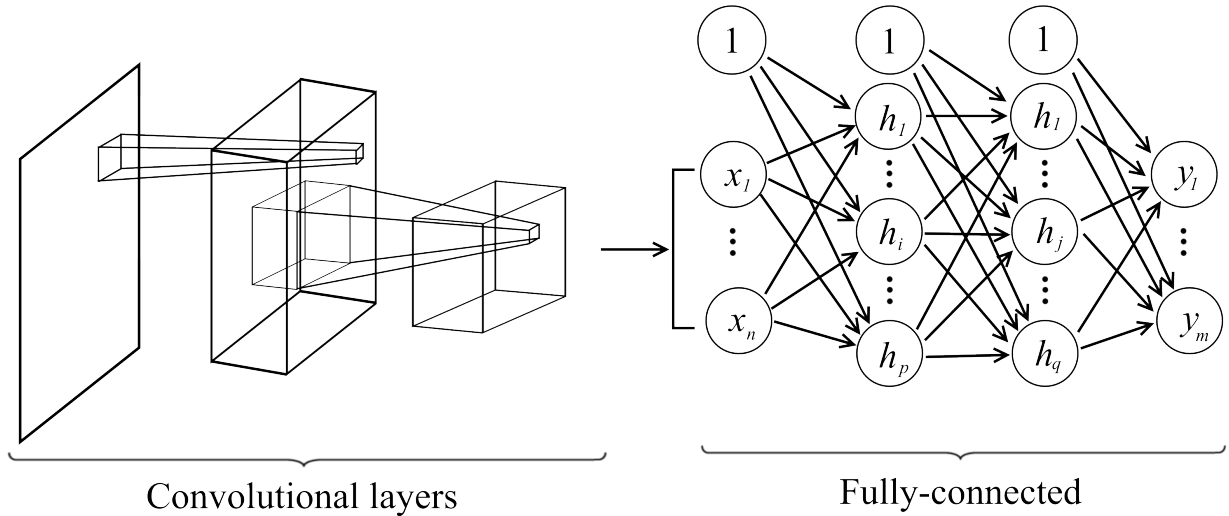


Figure 5.2: Convolutional neural network

such as images, CNN is chosen because of its inherent numerical efficacy and capacity to preserve the structure of the data while extracting meaningful statistical features.

During learning on large dataset an important question to consider is overfitting. In early days naive Lasso and Ridge regularization were often applied to MLP, but became impractical in deep models. A stochastic alternative that became extraordinarily popular due to computational efficiency and stable results was proposed in [143]. Dropout provides a computationally inexpensive, but powerful method of regularizing a broad family of models by randomly dropping activations of the units at chosen probability. To the first order approximation, dropout is a method of making bagging practical for ensembles of very large neural networks. Specifically, at each training step we randomly dropout units from the network, which yields a new model [140].

Another popular technique that is sometimes regarded as regularizing in batch normalization. Introduced in 2015 [144], it still remains popular due to numerical efficiency and benefits during training. It was initially proposed to mitigate internal covariate shift, a change in distribution of the inputs due to randomly initialized previous layers. Since training adjusts the parameters across all layers, the distribution of the inputs changes accordingly. This

problem is especially pronounced in deep neural networks, as small changes in hidden layers are amplified as they propagate through the network. Batch normalization shifts and rescales the inputs and helps to avoid changes in covariate distribution. As the training becomes more stable, larger learning rates can be used without danger of causing vanishing or exploding gradient. Several different flavors of normalization layers were recently introduced, including layer normalization. While batch normalization operates across the batch dimension and works best on large batch sizes, layer normalization [145] can be applied even when the batch size is equal to 1.

5.1.2 Importance of network architecture

Besides the core nodes, connections between them is another critical element of deep neural networks. In fact, sophisticated network architectures was among the key developments that led to the emergence of deep learning models with exceptional performance. With advanced building blocks researchers improved both computation efficiency and performance across diverse problems. Moreover, many architectures that achieve high performance on one set of problems could be applied to other problems through transfer learning, a technique for recycling pre-trained network parameters for initialization before the actual training. This gives flexibility to developers and makes the invention of novel models such as EfficientNet [146] a lot more valuable.

One famous deep neural architecture is Inception (also known as GoogLeNet), which was originally presented in 2015 [147] and further improved and combined with ResNet in 2017 [148]. Authors proposed a novel building block called inception which contained three convolutional layers of window sizes of 1, 3, 5 and a max pooling layer of size 3 all operating at the same input in parallel (see Figure 5.3 A). The outputs are then concatenated together and fed to the next inception block. To limit computational load due to exponentially growing number of concatenated features, authors inserted convolutional layers of window size 1. In addition, to reduce overfitting and excessive number of parameters, authors used global average pooling to reduce dimensionality towards the end of the network. GoogLeNet

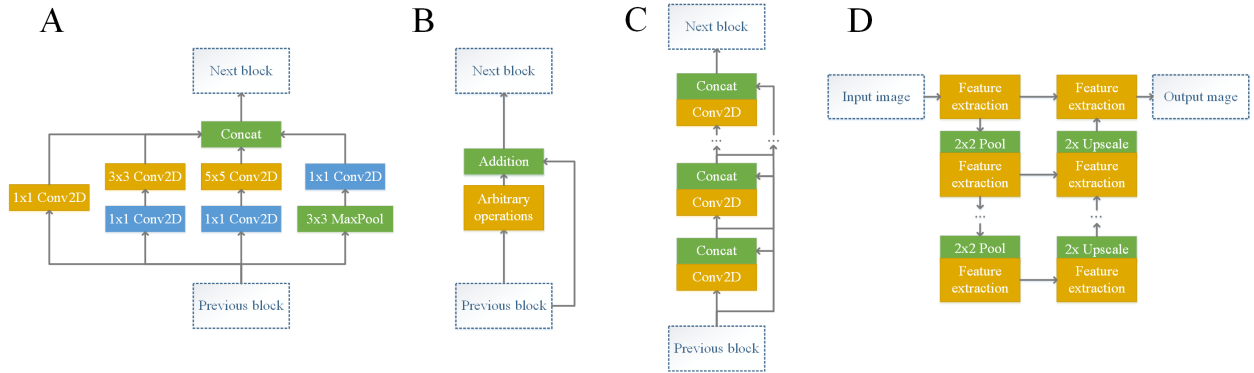


Figure 5.3: Famous computer vision building blocks: (A) inception block, (B) residual block, (C) dense block, and (D) U-Net

became one of the most popular image classification models and clearly demonstrated that going deeper with convolutional neural networks improves both performance and efficacy.

With increase of the number of layers, however, neural networks deal with a notoriously difficult problem called vanishing gradient. During back-propagation the gradients may become infinitely small due to numerous multiplication operations. This leads to performance saturation or even degradation as the number of layers increases. ResNet, a neural architecture proposed in 2016, solves this issue by introducing an identity shortcut connection, also known as a residual or skip-connection [149]. This configuration makes a block learn a residual needed to correct its input (see Figure 5.3 B). Theoretically, residual block can include any arbitrary operation depending on the problem. Authors assume that learning a residual mapping is easier than directly fitting the desired mapping and, therefore, stacking layers should not degrade the model performance. This can also be true because we could stack identity mappings instead of arbitrary operations and the resulting architecture should perform the same. This also means that deeper models should not produce a training error higher than its shallower counterparts. This simple argument made ResNet one of the most well-known architecture actively used in research and production.

Another highly successful example of use of skip-connections is dense convolutional network that introduced a dense block [150]. Motivated by the goal to increase the efficacy

of deep CNNs and, particularly, MLP-based feature extraction, authors proposed to use a novel block called dense block. Unlike ResNet, where element-wise addition is used, dense blocks employ concatenation. Each layer receives feature maps from all preceding convolutions within the same block (see Figure 5.3 C). This apparently leads to a quick growth of the number of features, which is conveniently controlled by hyperparameters such as depth of each dense block and growth rate of the parameters. Additionally, authors used convolutional layers and pooling between dense blocks to control the dimensionality. DenseNet became widely used in various computer vision problem such image classification, object detection, and image segmentation due to superior computational efficiency and quality of the learned features. Despite having dense skip-connections, it needs fewer trainable parameters than ResNet and, at the same time, allows easy gradient propagation. This allows the model learn very diverse, yet simple, features that boost its performance.

Image-to-image problems include reconstruction, segmentation, detection, and others. They are particularly important for medical imaging domain as they are often used to augment traditional methods. One of the famous examples is U-Net, a fully convolutional ANN proposed for biomedical image segmentation in 2015 [151]. The architecture consists of a contracting path and an expansive path, which gives it the U-shaped form (see Figure 5.3 D). The contracting path takes the input image and extracts features through a series of feature extraction blocks followed by a scaling down block such as a pooling layer. This is essentially a CNN that scales extracts feature and scales down the input image. The expansive path concatenates the features of the same resolution and applies addition feature extraction. The up-scaling method could be anything from a non-trainable Nearest-Neighbor algorithms to a deep CNN. Additional skip connections between individual blocks of the contracting and expansive pathways enables easier gradient propagation and more stable learning. Importantly, the symmetry between two paths and the U-shaped architectures lets the network propagate context information to higher resolution layers and achieve better results. U-net obtained popularity in numerous bio-medical application including brain MRI, CT, and ultrasound imaging. It also contributed to popularization of the end-to-end fully-convolutional networks for semantic segmentation.

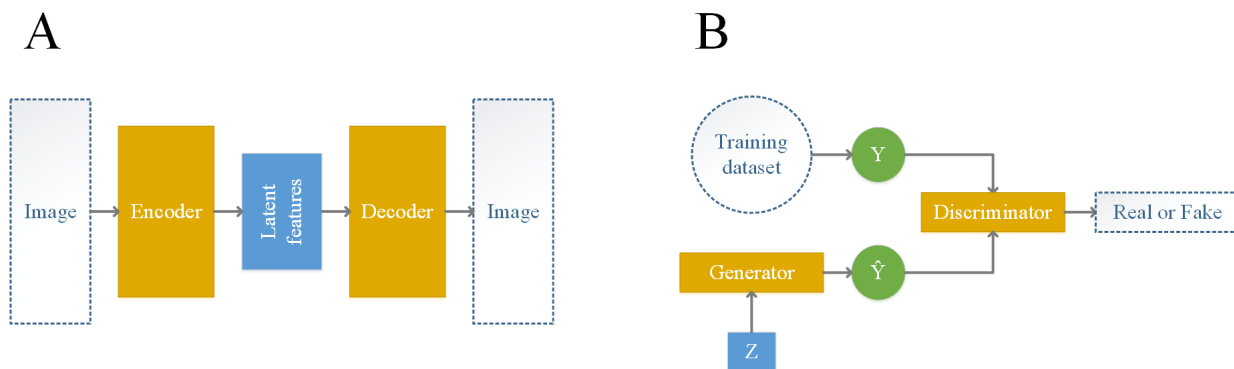


Figure 5.4: Data representation and generative modeling: (A) autoencoder and (B) generative adversarial network (GAN)

Another interesting type of image-to-image architectures is autoencoder (AE). It is often used to learn efficient data representation in an unsupervised manner. AE has two major parts connected sequentially: encoder and decoder (see Figure 5.4 A). The goal of the encoder is to learn the best mapping of the input data to a latent space. As the dimensionality of the latent space is typically much smaller than the input dimensions, AE is frequently used as a method for unsupervised dimensionality reduction. Along with the encoding part, a decoding side is learnt, where the model tries to reconstruct the input data from the reduced latent features. Several variants of AE exist including variational AE (VAE), where the latent features are used as the parameters for independent Gaussian distributions. The input to the decoder is then sampled using these parameters. VAE usually yields smooth mapping between the latent space and the data and frequently used in generative learning where changing input of the decoder continuously adjusts the output image.

A distinct approach to generative learning was proposed in 2014 [152]. Generative adversarial network (GAN) is a class of machine learning frameworks where two ANNs (called generator and discriminator) contest with each other (see Figure 5.4 B). The generator creates candidates while the discriminator tries to distinguish between the generated candidates and real images. By learning how to increase the error rate of the discriminative network, generator finds an optimal mapping from a latent space to the training data. Ideally, the

generator should learn the distribution of the training dataset. This requires a strong discriminative model, which is sometimes unavailable. Poorly performing discriminators lead to a "mode collapse" where generator fail to generalize properly. Besides generative modelling, GANs have also proven useful for semi-supervised learning and reinforcement learning.

5.1.3 Geometrical neural networks

The majority of the computer vision deep learning-based solutions assume images defined on Euclidean domains that could be represented by 2D or 3D grids. While the assumption is justified for most of the use cases, there are many fields where data is inherently non-Euclidean and takes forms of graphs, meshes, and manifolds. Geometrical neural networks extend the conventional deep learning methods to these types of structured data.

Let us consider a graph defined by the adjacency matrix A . We can define graph Laplacian $\Delta = D - A$, where D is the degree matrix. Eigendecomposition of Δ would give a matrix of eigenvectors $Q = (q_1, \dots, q_n)$. Now, for any two signals x and y defined on the original graph space their Fourier transforms can be defined as $Q^T x$ and $Q^T y$ respectively. Then, spectral convolution can be defined as the element-wise product:

$$y * x = Q(Q^T y) \odot (Q^T x) \quad (5.2)$$

Spectral convolutional neural networks employ 5.2 to define spectral convolutional layer operation as:

$$f_i(x_i) = g\left(\sum_j Q_k \Theta_{ij} Q_k^T x_i\right), \quad (5.3)$$

where Θ is a diagonal matrix representing a trainable convolutional filter (kernel), x_i is a vector of the input matrix x , Q_k contains the first k eigenvectors, and g is an arbitrary activation function. To alleviate computation burden associated with the graph Fourier transform, Chebyshev polynomials are often used to represent the spectral filters [153]. Spectral convolutions were among the first developments in geometrical deep learning that led to applications in networking, natural language processing, genomics, graphics, and many others.

An alternative to spectral methods is spatial approach. Monti and Boscaini *et al.* pro-

posed a good generalization in a form of mixture model networks (MoNet), a framework that allows designing convolutional deep architectures on non-Euclidean domains independent of the underlying manifold or graph structure [154]. For any point a in an arbitrary manifold or a node in a graph, they consider points $\{b\}$ in the neighborhood of a . Convolution of two signals defined in this space can be defined as:

$$(y * x)(a) = \sum_j g_j \sum_{\{b\}} \left[w_j[u(a, b)]f(b) \right], \quad (5.4)$$

where $u(a, b)$ is the pseudo coordinates of a chosen dimensionality and the kernel W is modelled as a trainable Gaussian mixture model of the form:

$$w_i(u) = \exp \left[-0.5(u - \mu_j)^T \Sigma_j^{-1} (u - \mu_j) \right] \quad (5.5)$$

A recent example of a practical geometrical neural network applied to mesh data is called MeshNet that was proposed for learning 3D shape representation [155]. Mesh is an efficient method of representing surfaces and volumetric objects. Having adaptive size of the elements mesh can depict objects of arbitrary local complexity, while having a sparse and compact representation. The drawback is, however, a highly diverse and sophisticated structure of the mesh that is difficult to analyze with conventional computer vision and deep learning methods. Authors, therefore, proposed two building blocks called spatial and structural descriptors for learning the initial features, and a mesh convolution block. In their approach a 3D mesh representing a surface is translated into a collection of faces (triangles) with spatial (location) and structural (connectivity and size) features. MeshNet extracts these features by combining 1D convolutions, pooling operations, Gaussian kernel correlation, and MLP. Finally, the mesh convolution block expands the receptive field of faces by aggregating spatial and structural features of the neighboring faces. The approach achieves state-of-the-art performance in 3D object classification and retrieval tasks while being relatively compact (4.25 million trainable parameters).

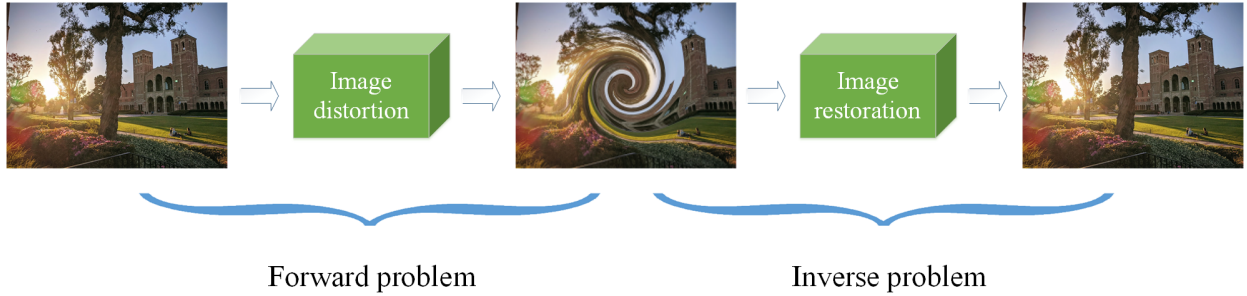


Figure 5.5: Example of a forward and the corresponding inverse problems: image distortion (F) and image restoration (F^{-1})

5.2 Inverse problems

Mathematical problems can be classified into forward and inverse types. A forward problem starts from a cause and estimates the effects, while the inverse problem estimates the cause by observing the effects. The majority of forward problems are numerically stable and have known solutions. The inverse problems, on the other hand, are often ill-posed. However, due to abundance in nature they attract attention of researchers in medical imaging, optics, signal processing, geophysics, astronomy, remote sensing, machine learning, and many other fields. Inverse problems remain active area of research in science and mathematics because they allow us to discover the properties that we cannot directly observe.

For a forward problem we can generally define a mapping $F : X \mapsto Y$. Then, for an invertible F there exists an inverse problem that we describe with the inverse mapping $F^{-1} : Y \mapsto X$. Finding the inverse mapping becomes difficult when the forward problem introduces noise or leads to loss of information. Particularly, a small perturbations in y may lead to a large changes in x , which clearly makes the problem ill-posed. Therefore, the forward model can be described as follows:

$$y = F(x) + \xi \tag{5.6}$$

where ξ models random noise. Analytical optimization methods such as minimization of the squared error $\|y - F(x)\|^2$ or maximum *a posteriori* estimation (MAP) have been exten-

sively studied for a long time. Supplemented with *a priori* information and regularization techniques, these methods were proven to be robust, but often come with poor results and significant computational costs.

An alternative approach that quickly became popular with recent advances in semiconductor processing and the rise of computational capacity is to employ machine learning. Deep neural networks were successfully applied to a variety of inverse problems [68, 67, 65, 156, 157, 158, 66, 159]. Apparently, given a sufficiently large dataset a deep ANN can be trained to solve inverse problems. We divide these approaches into three fundamentally different categories: deep prior, deep approximation, and deep representation. The majority of early works used deep prior to improve image reconstruction results by removing noise and artifacts. They train ANNs on custom dataset to learn *a priori* information, so that the model would be able to impose that prior on the reconstructed images. Deep approximation learns the inverse mapping F^{-1} by training a deep ANN $\Phi(\cdot)$, which directly finds a solution $\Phi(y) = \hat{x}$ that minimizes a loss function chosen for model training. Similarly, the forward mapping F can be learned with a deep invertible ANN $\Psi(\cdot)$ and its inversion $\Psi^{-1}(\cdot)$ can be taken as an approximation to F^{-1} . Finally, in deep representation approaches we train an ANN to estimate the loss function (or its parts) or another representation that can be used in an underlying analytical optimization method. Interestingly, that the later often results in *a priori* information being built-in in the learned parameters of the ANN.

5.2.1 Deep prior

One of the first applications of deep neural networks in inverse problem was post-processing of a solution obtained using an alternative method (see Figure 5.6). In this case, a deep learning model does not solve the inverse problems, but rather improves the solution by imposing appropriate prior information learned during training.

An inverse mapping $B : Y \mapsto X$ is first used to obtain a solution \hat{x} . Then, a neural network Φ is used to improve the solution as $\hat{x}_{OPT} = \Phi(\hat{x}) = \Phi(B(y))$. Since \hat{x} is an image (at least in some cases), powerful pre-trained models are typically employed. A model of a

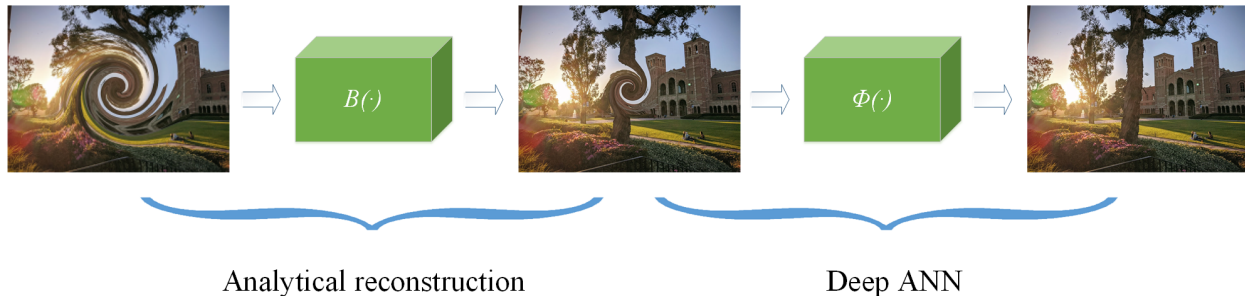


Figure 5.6: Deep prior approach

previously reported architecture is initialized with parameters trained on a common-purpose dataset and then retrained to remove artifacts and noise from images. This training scheme is called transfer learning. Note, that Φ is trained independently from B and does not know about operations applied in the forward and inverse mapping.

As an extension to deep prior approach of image denoising, Φ could be combined with another optimization procedure that minimizes a discrepancy metric similar to $\|y - F(\Phi(B(y)))\|^2$. Such iterative schemes were previously demonstrated in [160, 161, 162, 163]. Note, that training of Φ usually involves extensive use of the alternative inverse and forward solvers, so that $\Phi(\cdot) = (\Phi_n(\cdot) \circ U_n(y, \cdot) \circ \dots \circ \Phi_1(\cdot))(\hat{x})$, where U_i is a training step that updates the parameters of Φ using its estimate $\Phi_{i-1}(\hat{x})$, the forward mapping F , and the known y . Typically the updates are obtained using gradient descent. Apparently, this cascaded scheme improves data consistency and makes Φ to include more relevant prior information.

5.2.2 Deep approximation

Due to the ability of ANN to fit non-linear functions, training deep neural networks to learn a mapping from the observation y to its reconstruction x is often the favored approach in imaging field. Initially MLP was proposed to be used as a universal function approximation to learn the inverse mapping. Zhang and Salari [164] used an MLP with one hidden layer to denoise images in the wavelet domain. Burger *et al.* [165] added another hidden layer to learn end-to-end mapping from noisy and noiseless images using an MLP. Note, that these

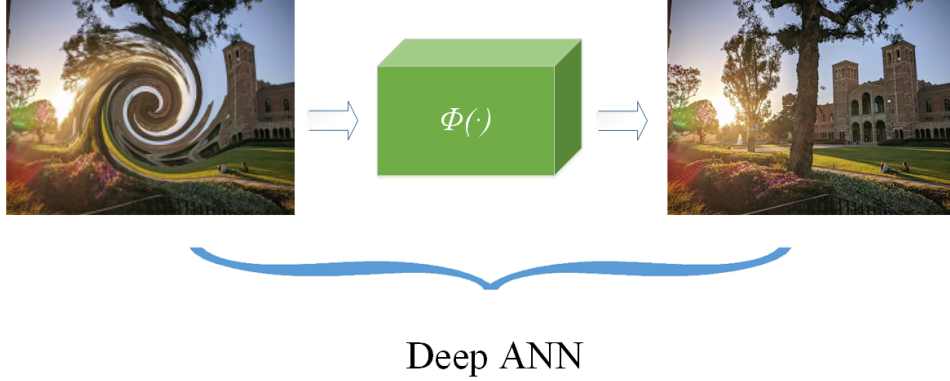


Figure 5.7: Deep approximation approach

methods could be also seen as deep priors and could be applied on reconstructed images. For instance, a denoising ANN could be used to clean the CT or MRI images reconstructed using another method.

While deep approximation was practically implemented for various applications, several theoretical works were recently published. For instance, a novel theory for deep convolutional framelets was proposed by Ye *et al.* [64]. Authors rely of classical signal processing and give specific rules and guidance on how to design convolutional neural networks. Particularly, they consider deep CNN with ReLU activation and argue that popular building blocks such as residual block, redundant filter channels, and concatenated ReLU help learning better inverse mapping, while the pooling layers should be augmented with skip-connections.

Another interesting approach is based on inverting neural networks, as was reported in [166]. Authors proposed to use invertible neural networks and particular affine coupling layer, a popular invertible building block (see Figure 5.8). In this scheme the input data is split into two parts $x = [x_1, x_2]$. The output is then obtained by concatenating the corresponding outputs $y = [y_1, y_2]$. The inverse transformation can be obtained as follows:

$$\begin{cases} y_1 = x_1 \odot e^{\Phi_3(x_2)} + \Phi_4(x_2) \\ y_2 = x_2 \odot e^{\Phi_1(x_1)} + \Phi_2(x_1) \end{cases} \iff \begin{cases} x_1 = (y_1 - \Phi_4(y_2)) \odot e^{-\Phi_3(y_2)} \\ x_2 = (y_2 - \Phi_2(y_1)) \odot e^{-\Phi_1(y_1)} \end{cases}, \quad (5.7)$$

where $\Phi_i(\cdot)$ are any arbitrary deep learning models, not necessarily invertible, but trainable through conventional back-propagation using stochastic gradient descent. Now, we can train

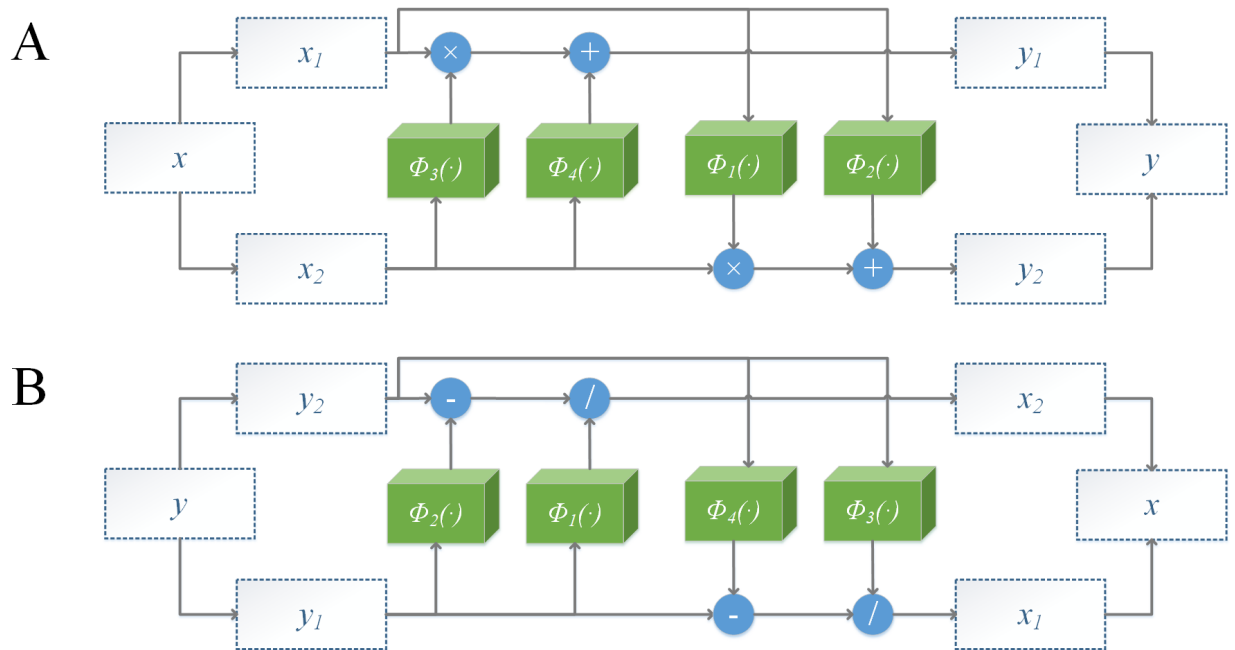


Figure 5.8: An invertible neural network built using affine coupling layer: (A) forward pass and (B) inverse pass

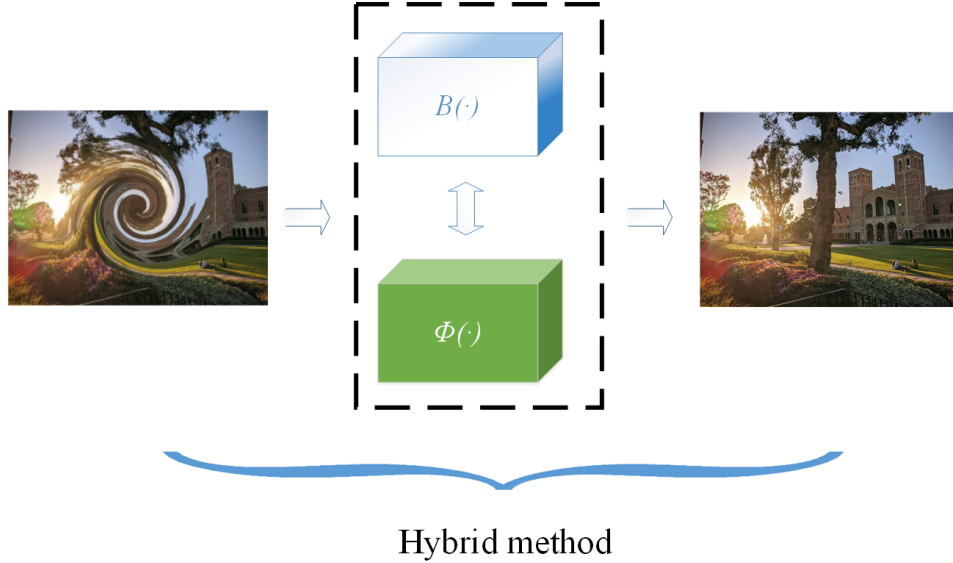


Figure 5.9: Deep representation approach

a deep ANN to fit the forward mapping $F : X \mapsto Y$ and then take its inverse to approximate the inverse mapping $F^{-1} : Y \mapsto X$. Given that forward problem is frequently more stable, learning F seems to be easier. However, a set of parameters that would satisfy the forward mapping up to a small error, might, in theory, cause much larger issues in the inverse mapping F^{-1} . Moreover, the proposed scheme requires the dimensionality of x and y to be exactly the same, although the later could be avoided by appending constant values or random noise.

5.2.3 Deep representation

Since many inverse problems are numerically unstable, they require to use regularization. A popular approach is called Tikhonov regularization that provides improved efficiency in parameter estimation in exchange for bias. In a simplest case, it adds a second norm of the parameter vector to the loss function, or more generally:

$$L(\hat{x}, \Phi) = \|F(\hat{x}) - y\|^2 + \lambda_R \cdot \psi(\Phi(\hat{x})), \quad (5.8)$$

where λ_R is regularization hyperparameter, ψ is a functional that maps to a positive scalar in $[0, \infty]$, and Φ is a function that measures how much regularization is needed (see Figure 5.9). For instance, $\psi(\cdot) = (\cdot)^2$ and $\Phi(\cdot) = \|\cdot\|$ is equivalent to L_2 regularization.

Recently, a few novel deep learning-based regularization approaches were proposed. They combined deep neural networks with Tikhonov regularization strategy and demonstrated noticeable improvement in the results. For instance, in [161] ResNet and L_2 norm were used as Φ and ψ . In [167] authors proposed the use of denoising engines instead of Φ . They used an explicit image-adaptive Laplacian-based regularization functional that is able to incorporate any denoising model, including deep CNN. A complete convergence analysis of this approach and guarantees on data consistency were recently presented in [168] where authors used a deep ANN as Φ and introduced the absolute Bregman distance as a new generalization from the convex to the non-convex setting. Another work used a regularizer that was able to distinguish the distributions of desired images and noisy images [169].

CHAPTER 6

Machine learning-enabled cellular impedance tomography

Besides describing electrical cellular response, the model that we proposed in Chapter 2 is capable of generating a large diverse dataset for training a machine learning model. In this chapter, therefore, we are going to discuss the use of deep learning models in solving the inverse problem of cellular EIT.

Previously, several machine learning-enabled EIT (ML-EIT) schemes were proposed. Most of the early works took an end-to-end deep approximation approach, where a predefined deep ANN is trained on a synthetic dataset generated using an underlying simulation model. For example, Zheng and Peng [69] proposed an autoencoder-based model to reconstruct images in electrical capacitance tomography, a close relative of EIT. The technique is commonly applied in industrial process monitoring for measurements of fluid flows in pipes. Authors generated a dataset of 40,000 samples, each consisting of capacitance measurements and the corresponding 2D permittivity distribution. To evaluate the performance they used 10-fold cross validation and added noise and experimental data to the testing dataset.

Deep approximation is still a dominant approach in ML-EIT, but more advanced neural architectures are proposed including ensemble of models [70], non-standard wavelet form of a neural network [71], and U-Net [72]. While ML-EIT demonstrated superior performance, the trade-offs of the blind end-to-end approach are yet to be discovered. Because EIT is a small niche with its own fundamental advantages and limitation we believe that a more elaborate analysis is necessary. For instance, prior knowledge on how electrical response of biological cells should not be ignored, but rather embedded in the newly developed methodologies.

Recently, a significant performance improvements in reconstructing targets with sharp corners or edges was achieved using a deep CNN and a novel iterative bases-expansion

subspace optimization method in [170]. In another work, authors improved performance of 3D image reconstruction by adding a geometrical prior in a novel structure-aware sparse Bayesian learning (SA-SBL) [171].

In this chapter we propose a deep neural architecture that inherently takes into account geometrical structure of the mesh and equi-distant electrode arrangement. Moreover, we introduce a novel network growth approach that dynamically adds new building blocks to the network graph to achieve higher imaging resolution. Finally, we introduce a hybrid loss function to make sure that the model learns physically meaningful features. Note that to be consistent with the conventional notations and unlike in the previous chapter, we use X for voltage measurements and Y for images.

6.1 Training and model selection

We generated a dataset of EIT measurements of adherent cells on equally-spaced MEA arrangement of 8 and 12 planar microelectrodes with pitch of $12 \mu m$. To mimic cellular response we used 3D FEM simulations as described in Chapter 2. More precisely, we synthesized random cell geometries at different adhesion stages: attachment, spreading, and further migration. Then, we combined several different cell geometries to mimic cell networks comprised of 2 - 4 cells. Overall, we obtained 50 diverse geometries (see a few examples in Figure 6.1). Inside the cell cytoplasm region, at the center of cell geometry, we created ellipsoidal nucleus comprised of nuclear envelope and nucleoplasm. For each geometry we applied random geometrical transformations including scaling, translation, and rotation as shown in Table 6.1. Due to inherent symmetry of the MEA structures we simulated 1/4 and 1/6 of the 8-MEA and 12-MEA respectively and then augmented the dataset by rotating the measurements, which helped us to significantly reduce computational burden. To mimic biological diversity we randomly sampled electrical material properties from parametric distributions accordingly to previously proposed models of adherent cells (see Table 4.2). Each sample was automatically converted into a tetrahedral mesh of varying size, which gave us an optimal trade-off between required computational resources and simulation accuracy. To

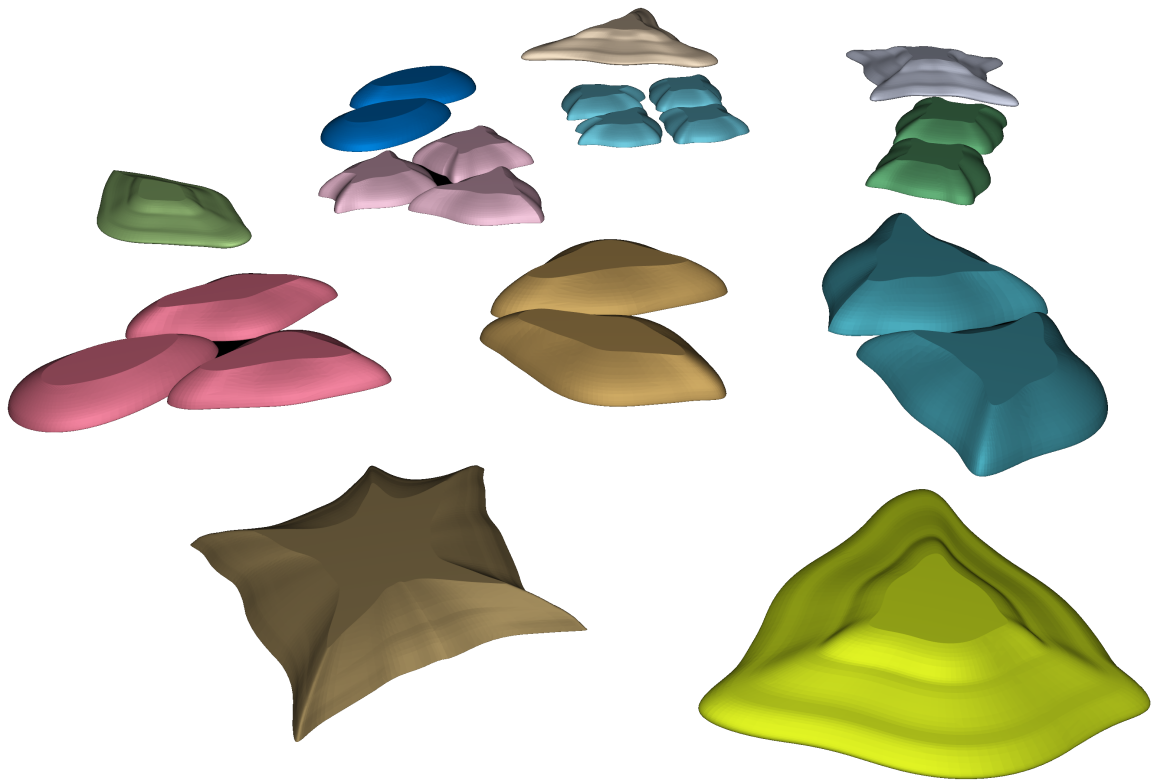


Figure 6.1: Examples of 3D cell geometries used in training dataset generation

Table 6.1: Geometrical transformations used in dataset generation

Transformation type	Range	Number of samples
Scaling	[0.5, 1.5]	8
Translation	$(x, y) \in [(-15, -15), (15, 15)]$	64
Rotation	$[-45^\circ, 45^\circ]$	16

ensure numerical convergence and data quality we carefully evaluated the generated mesh in each simulation to ensure that element skewness is at least 0.1, ratio of the element volume to its circumradius is above 0.01, and the total number of degrees of freedom to be below 10^7 . To numerically solve the corresponding PDE, we use flexible generalized minimal residual method (FGMRES), a simple and scalable FEM algorithm. After dataset augmentation, the overall size of the dataset was 26 and 39 millions of samples for 8-MEA and 12-MEA respectively.

We split the dataset into training (85 %) and testing (15 %) subsets. We then used 5-fold cross-validation by leaving one fifth of the training dataset for validation and fit the models on the remaining parts. By repeating the training steps five times, we estimate a mean of the performance metrics on the validation subsets. We use mean cross-validation performance for optimizing hyperparameters such as depth and width of the neural networks, as well as learning rates of the optimization algorithm. After training we evaluate each model on the testing dataset and report this metric as "testing" performance.

For each generated image we obtained the corresponding electrical measurements that have size of $L \times (L^2 - L) \times p$, where L is the number of electrodes and p is number of AC frequencies. Note that electrical measurements and images can be represented as mesh objects. In our case, we used a regular triangular mesh of constant element size (see Figure 6.2). To mimic realistic electrical measurements we added additive Gaussian noise layer that modelled 20 dB signal-to-noise (SNR) ratio.

We cast the image reconstruction problem as binary classification where "1" corresponds to nucleus and "0" corresponds to everything else. This allows us to train a neural network tuned for frequency response of nucleus and rule out false detection of cell membrane. In

each training we employed binary cross-entropy as a loss function and Adam optimizer, which improved stability and rate of convergence.

Our first attempt to approach the problem was to find a solution using a traditional analytical optimization method combined with deep prior network. NOSER is a good choice since it is relatively fast and results in a smooth image that can be further improved by passing through a deep neural network. It also has a nodal solver, which gives results consistent with our mesh data structure. During training, therefore, we generated an initial image using NOSER algorithm and then passed it to a subsequent neural network. We tried U-Net [151] and an autoencoder as examples of deep prior models.

In the second attempt we explored a popular regularization by denoising (RED) approach and recently proposed network Tikhonov (NETT) method. Inspired by RED, we used steepest descent optimization along with denoising AE to minimize the following loss function:

$$L(\hat{y}) = \|f(\hat{y}) - x\|^2 + \lambda \cdot \hat{y}^T (\hat{y} - \Phi(\hat{y})), \quad (6.1)$$

where \hat{y} is estimated image with NOSER, $f(\cdot)$ is the forward model (FEM), λ is a regularization hyperparameter, and $\Phi(\cdot)$ is AE.

Similarly, we employed NETT scheme to minimize loss function shown in 6.2 with incremental gradient descent. We decomposed the denoising AE that we used in RED approach as $\Phi(\cdot) = (\Psi_d \circ \Psi_e)(\cdot)$ and took the encoding part.

$$L(\hat{y}) = \|f(\hat{y}) - x\|^2 + \lambda \cdot \|\Psi_e(\hat{y})\|^2, \quad (6.2)$$

Next, we tried directly learn the inverse mapping by training a deep neural network. To be able to employ previously proposed models that are based on rectangular images, we used flat feature vectors \tilde{X} and a rectangular images \tilde{Y} obtained by resampling from mesh Y and padding it with zero valued pixels. We began with training previously proposed MLP [164] and invertible neural network (INN) [166] using Adam algorithm, a variation of stochastic gradient descent. Next, we adjusted DenseNet [150] and U-Net [151] and trained them to find a mapping $\tilde{X} \mapsto \tilde{Y}$. Finally, we introduced mesh convolution operation (see Figure 6.2) and built a corresponding U-Net architecture that we call InvUMeshNet. Additionally, we

trained InvUMeshNet in GAN settings, where the model functioned as a generator and its counterpart was used as a discriminator. As another generative approach we used conditional VAE (CVAE) model that mapped an initial image mesh reconstructed with NOSER to image mesh conditioned on the voltage measurements.

6.1.1 ENINet architecture

Given that the proposed device design results in inherently symmetric equidistant electrode arrangement we use regular spatial discretization with triangular mesh of constant element size. Moreover, to preserve spatial conformity between the measurements X and images Y , we represent Y as nodes in 2D meshes aligned with X . This enables us to use convolutions to find the mapping $X \mapsto Y$.

Therefore, the first core component we introduce here is 2D mesh convolution (see Figure 6.2). We force the kernel to have a hexagonal (honeycomb) shape, which allows us to define three sliding axes along the principal directions of the mesh. Similarly to rectangular 2D convolution, this instance is translation-invariant and preserves spatial information between the layers. Numerically, mesh convolution is also efficient as it leads to sparse connections between layers. The inverse operation, transposed 2D mesh convolution, is defined analogously to rectangular 2D convolution and has similar properties.

Next, we introduce a super-resolution block (see Figure 6.3) that we used to build the electrical nucleus imaging network (ENINet). Based on mesh convolution layers it takes voltage measurements V and an input image (mesh) of size $x \times y$, and returns a mesh of size $2x \times 2y$. The upper branch simply maps the voltage measurements to the image of a predefined size. Note, that the input voltages V are represented as mesh of a fixed size L . Since each transposed mesh convolution (shown in blue) scales up the input mesh by 2 (stride is 2), the number of these layers is equal to $\log_2\left(\frac{|out|}{L}\right)$. The bottom branch, on the other hand, takes an input image and passes it through a series of mesh convolutions and scales up the image with a transposed mesh convolution. Similarly to DenseNet, we employed several skip-connections to facilitate easier gradient propagation and faster learning, which becomes

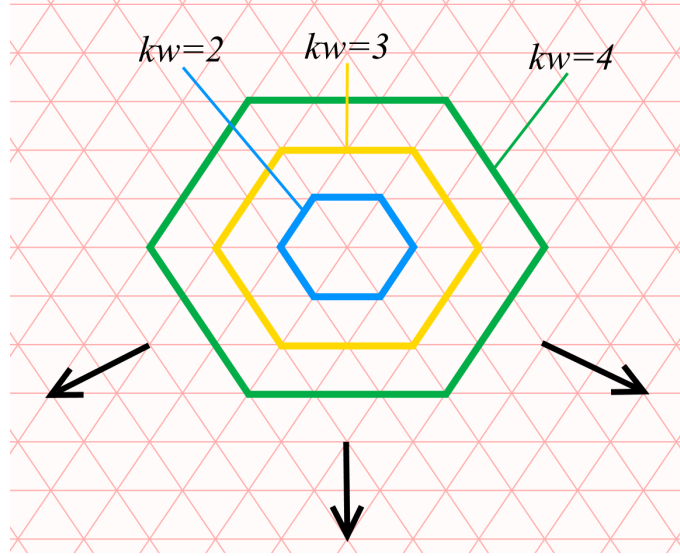


Figure 6.2: 2D mesh convolution with a few possible kernel window sizes (kw). Arrows represent sliding directions for a regular triangular mesh (shown in pink)

important for this lower branch when we stack blocks on top of each other. Outputs of the lower and upper branches are then concatenated together and passes through another mesh convolution layer of size 1 to reduce the dimensionality back. In parallel we introduce a non-parametric nearest-neighbour up-scaling layer, which simply repeats the values of the input image to magnify it. The NN-scaled image is then mixed with the output image accordingly to a weight α , which is non-trainable, but dynamically controlled. The purpose of NN-scaling is to stabilize training, which will become apparent in the next paragraph.

In Figure 6.4 A we show how we stack several super-resolution blocks dynamically during model training. We start with resolution of $12 \mu m$, which means that $|X| = |Y|$. Therefore, the first block does not have any transposed mesh convolution layers and may take any input image (e.g. constant blank mesh). In principle, the first block could also take an image reconstructed by another algorithm (e.g. NOSER). For each resolution block we train for 4 epochs: during the first 2 we linearly ramp up α from 0 to 1 (see Figure 6.3), while in the next 2 epochs we continue training to make sure each layer converges to an optimal point. When added the next block, we repeat the process, but now we use the output of the previous layer as the initial image. Introduction of gradual increase in α helps to

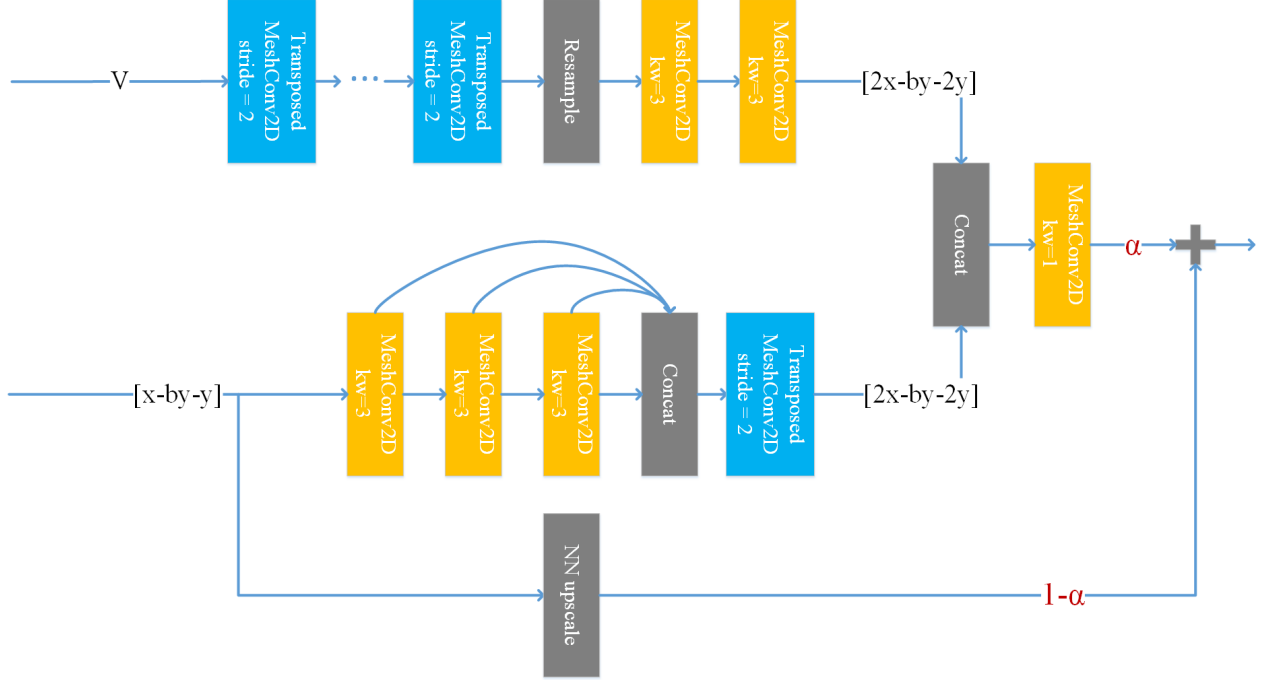


Figure 6.3: ENINet: super-resolution building block

smooth the training and lets the previous block to adjust its weights before the new block starts learning. This is particularly important for deep architectures as it promotes gradient propagation. Besides super-resolution blocks, we also have a series of tree mesh convolution layers of sizes 5, 3, and 1 that perform additional post-processing and convert the image into a binary form. In addition, we feed the result of the cascaded super-resolution blocks to FEM forward model that maps the image to voltages U and calculates auxiliary loss as $\frac{1}{|X|} \|V - U\|^2$. The overall loss that is being minimized during training contains both average binary cross-entropy (image) and MSE (voltages) (see Figure 6.4 A). The weighting factor β is a hyperparameter and we empirically found that the best cross-validation results are achieved when we scale it as $\beta = 2^{-N_{res}-2}$, where N_{res} is current number of super-resolution blocks, which implies that at lower resolution the model learns a more generalizable features if regularized by analytical forward map. As a forward mapping we employ a 2D FEM solver that solves relatively fast since the size of the mesh is small (see Figure 6.4 B). When handling multi-frequency measurements we found that if we concatenate the measurements ENINet

suffers from overfitting and struggles with real-world experimental verification. Presumably, it is caused by artificial relationship between frequency response of cell membrane and cell nucleus that are present in the simulations, but are not observed in experimental data. To avoid this we found an elegant and cheap solution - we process each frequency independently with the same model, which is practically implemented through parameter sharing. Then, we use max pooling from the results to obtain the final image. This pooling operation is performed in image reconstruction part of ENINet (before sending the image to forward model), which makes the post-processing component to learn inherent *a priori* information on how to combine multi-frequency image reconstruction results. On the other hand, this approach deprives us of the opportunity to learn how cell nucleus responds to a particular frequency.

6.2 Numerical results

Since our output is a binary image, a good metric would be the area under receiver operating characteristic curve (ROC AUC), which is commonly used in binary classification tasks. Particularly, we use average across image pixels (mesh nodes). The mean values of the metric are reported in Table 6.2 below.

As we employed out-of-sample cross-validation (CV) and meticulously optimized model hyper-parameters, we observed small deviation between CV and testing results. The proposed model, ENINet, outperformed other approaches on both 8-MEA and 12-MEA datasets. Interestingly, that larger MEA gave a little better results across almost all methods, which is probably due to a bigger field of view and higher chances of having a nucleus within the electrodes array.

Early deep prior approaches demonstrated poor performance, which was expected since the underlying NOSER algorithm cannot ignore cell membrane and cytoplasm and includes them in the reconstructed image. Subsequent neural networks, therefore, have to learn how to transform these conductivity maps into binary nucleus images, which is difficult without having access to the original measured voltages. When we added the voltage measurements

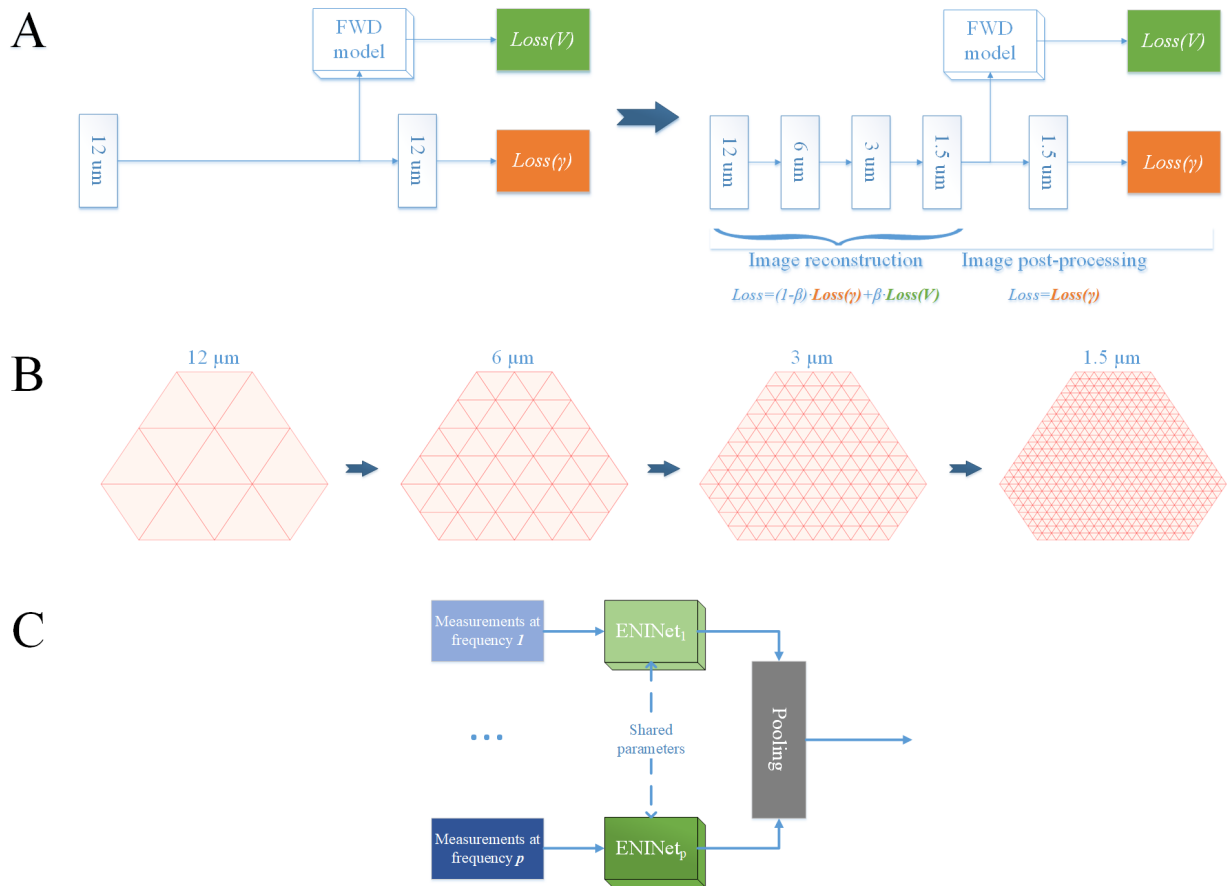


Figure 6.4: ENINet hybrid training approach: (A) growing network architecture and (B) corresponding mesh for 12-MEA, and (C) training on multi-frequency measurements data

Table 6.2: Out-of-sample mean average ROC AUC of deep learning models

Model	8-MEA		12-MEA	
	Cross-validation	Testing	Cross-validation	Testing
NOSER + U-Net ^{dp}	0.6657	0.6640	0.6823	0.6711
NOSER + AE ^{dp}	0.6788	0.6744	0.6959	0.6875
NOSER + RED ^{dr} [167]	0.7534	0.7456	0.7734	0.7668
NOSER + NETT ^{dr} [168]	0.7488	0.7345	0.7687	0.7408
MLP ^{da} [164]	0.8473	0.8303	0.8581	0.8498
INN ^{da} [166]	0.6122	0.5989	0.6170	0.6199
InvDenseNet ^{da}	0.8618	0.8539	0.8755	0.8660
InvUNet ^{da}	0.8752	0.8664	0.8902	0.8826
InvUMeshNet ^{da}	0.9289	0.9312	0.9324	0.9299
InvUMeshGAN ^h	0.8032	0.7921	0.8208	0.8058
NOSER + CVAE ^h	0.8511	0.8457	0.8567	0.8666
NOSER + ENINet ^h	0.9579	0.9471	0.9701	0.9553
ENINet^h	0.9731	0.9612	0.9897	0.9796

^{dp} deep prior, ^{dr} deep representation, ^{da} deep approximation, ^h hybrid methods

to the inputs of the deep ANN (NOSER + CVAE) as a conditional vector, we observed a noticeable jump in the performance, which clearly shows the bottleneck in deep prior approaches.

To explore deep representation models we employed RED and NETT combined with initial guess from NOSER. We found that performance of both methods are very similar, despite slight difference in the form of the regularization term and subsequent gradient optimization approaches. Although deep representation seems to be advantageous compared to deep prior, these methods still fell short compared to deep approximation. We presume that this is because the regularizing neural networks have no knowledge of the inverse problem, but rather estimate amount of noise in the image.

We discovered that deep approximation methods performed among the best. Perhaps, it is partially because these methods are trained to minimize binary cross-entropy, which directly translates to ROC AUC score. On the other hand, we observed that adding mesh convolutions significantly improved InvUNet, which shows that further efforts towards neural architectures customized for specific inverse problems may result in considerable improvements. While previously proposed MLP model demonstrated comparable performance, INN failed the benchmark. This is probably due to difficulty of learning exact forward mapping. As was mentioned in the Chapter 5, small disturbances to INN weights may lead to significant performance degradation in its inverse model due to severely ill-posed nature of EIT problem.

Finally, we explored several hybrid approaches. First, we trained InvUMeshNet using GAN framework and found it particularly difficult due to instabilities frequently emerging during training. The proposed ENINet, however, demonstrated stable and smooth convergence, although it took significantly more time to be trained due to small learning rate, dynamically growing graph, and necessity to iteratively solve the forward problem. Interestingly, that when supplied by NOSER conductivity image as the initial guess, ENINet ended up with inferior performance. Perhaps, the first super-resolution block in ENINet does not have sufficient capacity to learn mapping from NOSER's output to a binary nucleus image, which causes the degradation.

6.3 Experimental results

Besides having indisputable performance advantage deep learning is well-known for strong overfitting and poor generalization. We, therefore, tested the proposed methodology on real empirical data. First, we verified the reconstruction algorithms on single-cell and multiple-cell configurations and compared the result to fluorescent microscopy. Next, we applied ML-EIT to a popular practical case of cancer drug response and demonstrated its superior sensitivity to subtle changes in nuclear envelope permeability caused by the chemotherapy. To rule out any bias in this stage we performed model training and selection on the synthetic dataset prior to experimental verification. In this section we summarize the results.

6.3.1 Imaging cell nucleus

We conducted an experimental verification with HeLa cell line. The cells (HeLa AC-free, Sigma-Aldrich) were grown at 37 °C in Dulbecco’s Modified Eagle’s Medium (DMEM) supplemented with 10% fetal bovine serum (FBS) and 100 *units/mL* penicillin, and 100 $\mu\text{g/mL}$ streptomycin (PS). They were regularly passaged to maintain exponential growth. Twenty-four hours before staining and electrical measurements, we trypsinized HeLa cells, diluted them 1 : 5 with fresh DMEM medium without antibiotics, centrifuged, and suspended into fresh DMEM with 10% FBS and 1% PS. Then, we transferred 10 μL of the cell suspension ($2 \cdot 10^5$ *cells/mL* concentration) to the MEA devices with the attached PDMS wells (500 μL). To enable the long-term incubation we added 390 μL of fresh DMEM medium with 10% FBS and 1% PS and left the cells in the incubator for 24 hours at 37 °C and 5% CO₂. The cells appeared healthy and attached thereafter. During the incubation, the entire assembly of MEA, PDMS well, and the intermediate PCB was enclosed in a small vented Petri dish. After the incubation, the well was gently desiccated and washed with DMEM medium. To stain the cell nuclei, we added 20 μL of 2 $\mu\text{g/ml}$ Hoechst 33342 (Invitrogen) solution and incubated the cells for 25 minutes at 37 °C. We then gently desiccated the well and washed it with DMEM medium. To stain the cell membrane, 20 μL of 5 $\mu\text{g/ml}$ of WGA Alexa Fluor®488 conjugate (Invitrogen) solution were added, and cells were incubated for an-

other 10 minutes at 37 °C. After the last incubation, the well was gently desiccated, washed, and filled with a fresh DMEM medium with 10% FBS and 1% PS. We imaged the cells with fluorescent microscopy before and after the electrical measurements and observed no visible changes in structure, shape, and location caused by the electrical measurements.

For this series of experiments we used MEA of eight golden and transparent electrodes with pitch of 11 μm . MEAs were fabricated at Nanoelectronics Research Facility at UCLA. To make golden electrodes, layers of 20 nm of Ti and 100 nm of Au were vacuum-evaporated on fused silica wafers (100 mm in diameter) and the electrodes were patterned with the conventional lift-off process. To make transparent electrodes, a layer of 120 nm of indium tin oxide (ITO) was sputter-deposited on fused silica wafers (100 mm in diameter) and the electrodes were patterned with reactive-ion etching. On top of the electrodes we deposited a passivation layer of 500 nm of silicon dioxide with plasma-enhanced chemical vapor deposition (PECVD). To pattern the passivation layer, we employed deep reactive ion etching. We made circular openings of 4 μm in diameter at the center of the MEA and square contact pads of 5 mm at the edges. The wafer was diced into 25-by-25 mm square dies and each of them was cleaned in ultrasonic bath of acetone with subsequent deionized water wash, nitrogen blow and thermal dehydration. On top of the MEAs we designed 500 microliter (μL) wells of polydimethylsiloxane (PDMS) to allow long-term cell culturing. In addition, MEAs were connected to the intermediate printed-circuit board (PCB) with conductive silver epoxy adhesive (MG Chemicals). The intermediate PCB was connected to switching PCB that contained analog multiplexers and interfaces for vector network analyzer (VNA, HP 8753ES) and a computer. The computer was used to control stimulation power of the VNA, switch between the electrodes, and fetch data via General-Purpose Interface Bus (GPIB, Agilent 82357B).

In Figure 6.5 A-D we show the experimental results. We used the same 8-MEA arrangement in all four experiments with pitch of 11 μm and field of view of 420 μm^2 . Samples A, C, D had transparent ITO electrodes and sample B used gold electrode. To match with the reconstructed images, we visualized fluorescently stained nucleus in red and membrane in green on the images in the second column. Field of view of the devices is shown by white and

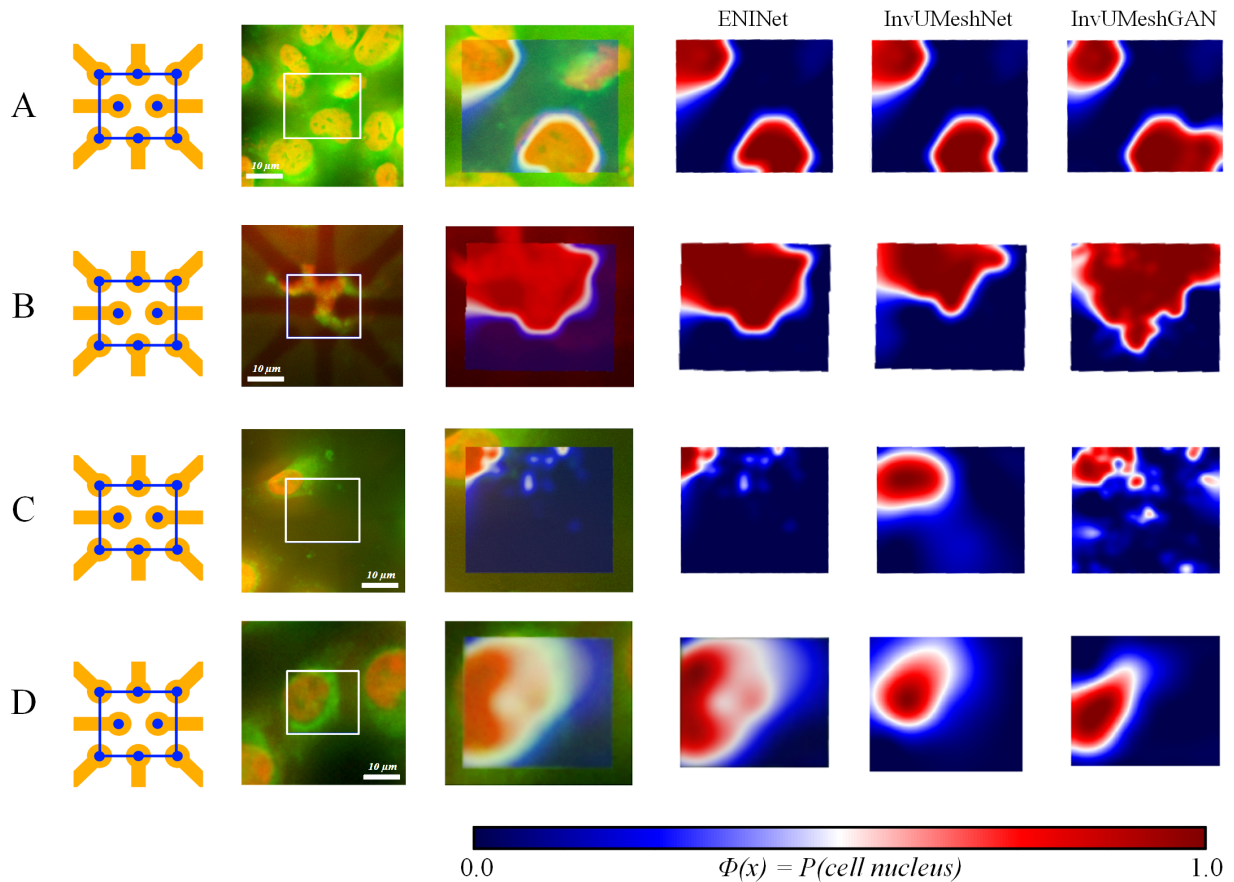


Figure 6.5: Electrically-driven imaging of cell nucleus on four samples shown in A-D. We used 8-MEA device with pitch of $11 \mu m$ (schematic arrangement is shown in the first column). To verify the reconstruction results we stained nucleus (shown in red) and membrane (shown in green). The white box represents the MEA area (field of view of the device). The third column shows an overlay of the nucleus reconstruction (ML-EIT) on top of the fluorescent images. The last three columns are the reconstructed images of the cell nucleus $\Phi(x)$. The red color represents area when the reconstruction algorithm predicts cell nucleus with greater confidence, while the blue regions are likely to have no nucleus

blue rectangles at the center of the images. An overlay of the fluorescent and reconstructed images is shown in the third column. The last three columns are the outputs of three models that demonstrated the highest performance on synthetic testing dataset.

Sample A in Figure 6.5 depicts multiple cells within the field of view of the device. Particularly, the cell in the top-left corner seems to be recently divided from the neighboring cell, but has already formed the nuclear envelope. The nucleus of the cell on bottom edge is slightly deformed and enlarged. Membrane of the cell shown that it is not fully spread, which might indicate that the cell is in prophase and is actively preparing to division by tightly condensing its chromosomes and initiating mitotic spindle formation. A cell in the top-right corner, however, was not detected by any of the reconstruction algorithms. A closer look at the image explains the reason: cell nucleus was severely deformed, which could indicate either cell death or nuclear envelope disintegration in metaphase. Either case leads to cell nucleus being invisible to electrical probing. Comparison analysis of the reconstructed images also shows that all three models successfully identified the location of cell nuclei, but had different estimation of the shape of the nucleus at the bottom edge due to noise in the measurements and perturbations coming from the cells outside the field of view of the sensor.

The second sample (B) shows a single cell captured at the center of a golden 8-MEA. Compared to the previous case, the cell was noticeably larger, but it did not confuse ENINet as it successfully identified the location and the shape of the nucleus. InvUMeshNet produced a similar estimated image, while InvUMeshGAN struggled, perhaps, due to differences in contact impedance of ITO and gold electrodes.

Figure 6.5 C captures another single-cell case where the cell barely covers the top-left corner of the device. It turned out that both InvUMeshNet and InvUMeshGAN models suffer from this type of edge cases. Apparently the location of the cell together with the measurement noise severely limit the signal and may lead to spike-like artifacts shown in InvUMeshGAN and ENINet. Intriguingly, however, some of these spikes well correlate with green fluorescent debris on the microscopy images. We presume that some of the debris may have electrical response equivalent to nuclear envelope and were misclassified by ML-EIT. InvUMeshNet generated a lot smoother image, which may be caused by stronger regulariza-

tion applied during model training. This, in fact, may be advantageous as it could lead to fewer artifacts and make the model less susceptible to edge cases.

The last sample features another single-cell imaging of a considerably large HeLa cell. While the cell covers the left half of the device, all three reconstruction algorithms successfully localized the nucleus. The difference came at the shape estimation. InvUMeshNet generated a slightly smaller nucleus, but had a roughly correct shape. InvUMeshGAN model slightly shifted the nucleus toward the bottom-left corner and produced too elongated and narrow shape. ENINet, on the other had, successfully identified both shape and orientation of the nucleus. Interestingly, that we observed a white point inside the red region. Optimistically, this implies that the nuclear envelope was compromised or had abnormally different electrical properties around that point. Another possible cause is, however, measurement noise.

6.3.2 Early detection of cancer drug response

To demonstrate another possible application of ML-EIT nucleus imaging, we studied a drug response of HeLa cells to low concentration of Doxorubicin. Doxorubicin is a popular anti-cancer (antineoplastic or cytotoxic) chemotherapy drug. It slows or stops the growth of cancer cells by blocking topoisomerase II (TOP2), an enzyme needed for cell division and growth. We specifically target low concentrations, as they typically impose difficulty evaluating drug response due to small effect observable through optical microscopy. Conventionally, a treated sample of cultured cells is imaged through fluorescent microscopy and a number of alive cells is tracked by manually counting the cells. Then, a sample is compared against the control group to evaluate an average treatment effect.

We prepared HeLa cells in a culture dish similarly to the previously described protocol. After culturing the cells, we transferred 10 μL of the cell suspension ($2 \cdot 10^5$ *cells/mL* concentration) to the MEA device with the attached PDMS well (500 μL). To enable the long-term incubation we added 240 μL of fresh DMEM medium with 10% FBS and 1% PS. In addition, we transferred 10 μL of the same cell suspension to 48 well of 96-well plate and added additionally of 240 μL of fresh DMEM medium with 10% FBS and 1% PS to

each well. We left the cells in the incubator for 24 hours at 37 °C and 5% CO₂. The cells appeared healthy and attached thereafter. During the incubation, the entire assembly of MEA, PDMS well, and the intermediate PCB was enclosed in a small vented Petri dish. After the incubation, the wells were gently desiccated and washed with DMEM medium. To stain the cell nuclei, we added 20 μL of 2 $\mu\text{g}/\text{ml}$ Hoechst 33342 (Invitrogen) solution and incubated the cells for 25 minutes at 37 °C. We then gently desiccated the wells, washed them with DMEM medium, and filled with a fresh DMEM medium with 10% FBS and 1% PS. Then, we randomly divided the 48 wells into 4 groups of 12 wells each and added Doxorubicin to three groups to achieve 0.3, 0.6, and 1.2 $\mu\text{g}/\text{mL}$ concentration of the drug respectively. The fourth control group of 12 wells was not treated. The samples on MEA devices were also treated with 0.3 $\mu\text{g}/\text{mL}$ of Doxorubicin.

We applied previously proposed ENINet for cell nucleus imaging to reconstruct nuclei at a single-cell resolution (Figure 6.6 A). At the beginning of the experiment we observe two closely located nuclei at the edge of the MEA. The small separation between the nuclei could suggest that both of them are located within a recently divided cell. After 4 hour of treatment with 0.3 $\mu\text{g}/\text{mL}$ of Doxorubicin we observe a drastic change in the topology - only one significantly shrunk nucleus is found close to the center of the MEA. As the drug is accumulated inside the nucleus and block important synthesis of essential biomolecules, nucleus, in fact, changes electrical properties of the nuclear envelope. Optically, however, this is not immediately evident as the size of the nucleus might remain the same and the cells remain attached. After another 8 hours of treatment, we imaged with ML-EIT once again and observed a further shrinkage of the nucleus. This time the nucleus did not change the location which is a strong indication that the cell was immobile. The shrinking nucleus, however, could indicate both physically decrease size of the nuclear envelope and increase in its electrical admittivity. For instance, depletion of TOP2 inside the cell could lead to partial or complete destruction of the nuclear envelope making it electrically indistinguishable from the cell cytoplasm. Later measurements showed no visible nucleus, which could also indicate a complete cell detachment caused by cell death. Visual inspection after 30 hours from treatment confirmed that the cell at the center of the MEA was floating. To quantify

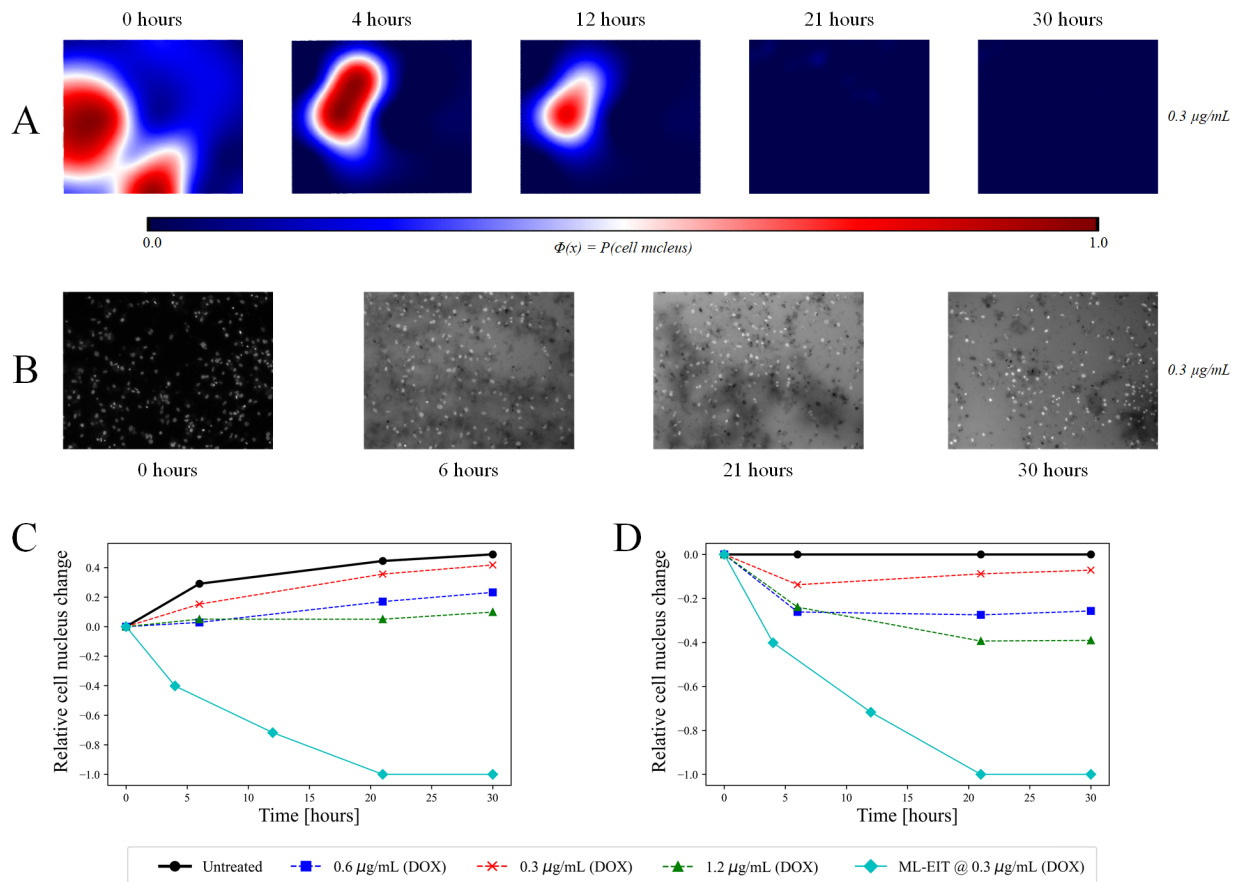


Figure 6.6: Detecting early effect of chemotherapy treatment with ML-EIT: (A) ENINet reconstruction of nuclei of a sample treated with $0.3 \mu\text{g/mL}$ of Doxorubicin; (B) fluorescent microscopy images of cells treated with $0.3 \mu\text{g/mL}$ of Doxorubicin; (C) relative changes in cell count (fluorescent microscopy) and nucleus size (ML-EIT) during the experiment; (D) relative changes in cell count compared to the baseline (control group) and nucleus size (ML-EIT). As a measure of relative cell nucleus change we used average number of visible cell nuclei on fluorescent images shown in (B) and the area of the red regions ($\Phi(x) > 0.5$) on the ML-EIT reconstructed images shown in (A)

the changes in the cell nucleus we measure the area of the red regions ($\Phi(x) > 0.5$) on the reconstructed images. We then plot a relative change of this quantity in Figure 6.6 C and D.

To compare the results of the ML-EIT imaging against a traditional method we estimated mean cell count using fluorescent microscopy. We collected fluorescent images depicting cell nuclei distributions in 48 wells. Samples of the fluorescent images are shown in Figure 6.6 B. As one can see, the cells remain viable despite nucleus staining and drug treatment, which also supports our argument on practical difficulty of measuring the effect of small drug concentrations. Note, that the background noise after treatment is caused by Doxorubicin, which is also fluorescent and overlaps with the nucleus staining. Following the imaging we manually counted the number of cell nuclei at 0, 6, 21, and 30 hours after the treatment. We took average of relative changes in cell count as a measure of nucleus changes. At any time $t = i$ we calculate the relative change of cell count CNT_i as its ratio to the cell count at time step $t = 0$: CNT_i/CNT_0 . The results are shown in Figure 6.6 C. We observed an expected suppression of cell growth caused by the treatment. Apparently the effect is more noticeable with the increase in drug concentration. Since we applied low-dose treatment cells continue to divide but at slightly lower rates. For a reference, we also estimated average doubling time of unstained cells to be 16.2 hours. In this experiment, however, we observed that the control group did not experience exponential growth due to nucleus staining. Despite being relatively non-toxic and widely used in live cell staining Hoechst 33342 molecules bind to DNA and significantly interfere with its replication during cell division, which is another example of invasiveness of fluorescent microscopy. On the other hand, nucleus staining gives simple and robust means of measuring cell proliferation. Note, that treated groups of cells were also stained with Hoechst together with the control group to be comparable and enable us distinguish an impact of subsequent drug treatment.

We take a difference in means of the average cell count to estimate the effect of Doxorubicin treatment. Results suggest (see Figure 6.6 D) 7.2 %, 25.7 %, and 39.1 % change in the relative cell count compared to the control group when treated with 0.3, 0.6, and 1.2 $\mu\text{g}/\text{mL}$ of the drug respectively. Interestingly, that at 0.3 $\mu\text{g}/\text{mL}$ the effect was diminishing with

time. Driven by cell recovery mechanisms this could eventually result in non-measurable level of treatment effect and wrong conclusions. Note that the difference in means of the fluorescently measured average treatment effect saturated after the first 20 hours, which was caused by the control group that slowed down the growth due to toxic effects of the nucleus staining.

Comparison of the curves in Figure 6.6 D reveals a significant advantage of ML-EIT. Particularly, the electrically-driven deep learning image reconstruction was able to immediately detect cell nucleus changes caused by the accumulation of the drug, while conventional method was not able to certainly distinguish the effect of treatment at $0.3 \mu\text{g}/\text{mL}$ concentration (red curve) from the control group. While detachment of an individual cell might seem to be the only reason behind the superior sensitivity of ML-EIT at 20 hours from treatment, it can not explain the apparently larger slope during the first few hours of the experiment. Moreover, ML-EIT reconstructed image before the treatment clearly showed two nuclei within the MEA and detachment of both cells is unlikely. Additionally, since we used immortal cancer cells well-known for surviving in adverse environment random detachment of a cell does not sound as a probable factor. Finally, typical cell detachment takes a short time, while in our experiment we observed a gradual shrinkage of the cell nucleus for up to 12 hours since Doxorubicin treatment.

CHAPTER 7

Concluding remarks

Everybody has a capacity for a happy life. All these talks about how difficult times we live in, that's just a clever way to justify fear and laziness. It's necessary to work now, but times might change

Lev Landau

Studying biological cells requires reliable tools and methods for imaging and sensing. In this dissertation we explored and demonstrated feasibility of all-electrical cellular tomography. Driven by exposure to AC electric field, cellular EIT gives means for non-invasive and label-free imaging that can be scaled and automated by further on-chip integration and use of microfluidic structures.

7.1 Electrical properties of biological cells

The first key result of this work is a scalable data-driven simulation framework that models how biological cells respond to an external electric field. The model is built upon empirical data collected over the last 60 years. We discovered that cell organelles have unique frequency response and may be distinguished with only a few electrical stimulations.

We found that adherent and non-adherent animal cells tend to have similar properties, while yeast cells and bacteria have thicker non-conductive membranes, but more conductive cytoplasm. Membrane capacitance and cytoplasm permittivity can be described using

log-normal distribution, which is fundamentally driven by synthesis of biomolecules and formation of lipid bilayers. On the other hand, conductance of the membranes and conductivity of the cytoplasm are driven by switching ion channels and pores that cause gamma distribution of these electrical properties. To achieve high-fidelity modelling we proposed a method to numerically generate smooth 3D shapes of adherent cells. Our approach gives an optimal trade-off between accurate geometric representation and numerical complexity of the subsequent FEM simulations. We then demonstrated the importance of cell geometry on modelling of electrical cellular response. Experimental impedance spectroscopy measurements of a single HeLa cell clearly showed how accurate the model is.

The proposed framework 1) establishes the first stochastic model of electrical properties of cells that are affected by biological diversity and underlying internal mechanisms; 2) captures cellular electrical response and shows feasibility of probing of internal organelles; 3) enables machine learning methods in sensing and imaging by providing a robust data-generation pipeline.

7.2 Cellular imaging using a few electrodes

The second key results is enhanced EIT for single-cell imaging. Because EIT was originally developed for human body imaging and suffers from insufficient resolution, we extended it by designing a novel device and image reconstruction algorithm. The proposed approach involves a two-step analytical optimization that exploits unique topology of the problem and *a priori* knowledge of dielectric properties of cells. Microscopic EIT fills the gap in rapid non-invasive imaging and is able to capture the slightest changes underneath the cell that are unobservable in the conventional optical microscopy. As electrical impedance very sensitively responds to changes in cell thickness and cell adhesion, cellular EIT can drastically extend biomedical studies such as drug response, cell phenotyping, motility, and so on.

Finally, we developed nucleus tomographic imaging by further extending the proposed device with a custom machine learning model. As cell membrane becomes electrically transparent at higher frequencies it exposes interior of the cell to electric field and enables nucleus

imaging. Driven by high-fidelity data generation pipeline, the proposed ML-EIT showed robustness on ITO and gold electrodes. Our approach provides a scalable solution for non-invasive single-cell nuclear tomography, a long-standing challenge in biology and raises a fundamental question of sensing inner cellular organelles with an electric field.

7.3 Future directions

Label-free cellular imaging will be in high demand in the future and we hope that electrically-driven methods will be extended to new exciting applications.

As one of the most promising directions that we see is a fundamental study on electrical properties of cells and the underlying microscopic mechanisms. Besides biological significance, such analysis would show the primary factors that determine how far EIT and other techniques could be extended. Despite having straight practical implications, this direction is, however, the most complex and might require extensive investments.

Another intriguing direction is device design. As electrical stimulations generate structured data they present abundant opportunities for scaling and automation. Particularly promising is the work towards on-chip integration with existing CMOS-based sensors and microfluidic devices. On the other hand, EIT is fundamentally limited by the measurement noise and novel device designs may lead to considerable improvements.

EIT reconstruction belongs to a broad family of inverse problems which is actively studied nowadays. We believe that additional efforts towards hybrid methods that combine deep learning and analytical methods could further improve the performance of the image reconstruction. For instance, with carefully analyzed network architectures emerging building blocks could be used to mimic those operations presented in analytical methods and inherently preserve the *a priori* information about the physics of the problem.

Finally, we believe that the developments in this and other works on microscopic EIT could be translated back to human body and industrial applications and may lead to novel use cases such as non-invasive point-of-care testing for early pneumonia detection, comple-

mentary sensing for robotic arms, or human-computer interfaces.

REFERENCES

- [1] H. Pauly. Electrical properties of the cytoplasmic membrane and the cytoplasm of bacteria and of protoplasts. IRE Transactions on Bio-Medical Electronics, 9(2):93–95, 1962.
- [2] Werner R. Loewenstein and Yoshinobu Kanno. Some electrical properties of the membrane of a cell nucleus. Nature, 195(4840):462–464, 1962.
- [3] Edwin L. Carstensen. Passive electrical properties of microorganisms. Biophysical Journal, 7(5):493–503, 1967.
- [4] V. K Miyamoto and T. E Thompson. Some electrical properties of lipid bilayer membranes. Journal of Colloid and Interface Science, 25(1):16–25, 1967.
- [5] Akihiko Irimajiri, Tetsuya Hanai, and Akira Inouye. Dielectric properties of synaptosomes isolated from rat brain cortex. Biophysics of structure and mechanism, 1(4):273–283, 1975.
- [6] Koji Asami, Tetsuya Hanai, and Naokazu Koizumi. Dielectric properties of yeast cells. The Journal of Membrane Biology, 28(1):169–180, 1976.
- [7] R. Pethig. Dielectric properties of biological materials: Biophysical and medical applications. IEEE Transactions on Electrical Insulation, EI-19(5):453–474, 1984.
- [8] A Surowiec, S S Stuchly, and C Izaguirre. Dielectric properties of human b and t lymphocytes at frequencies from 20 khz to 100 mhz. Physics in Medicine and Biology, 31(1):43–53, 1 1986.
- [9] A. Irimajiri, K. Asami, T. Ichinowatari, and Y. Kinoshita. Passive electrical properties of the membrane and cytoplasm of cultured rat basophil leukemia cells. ii. effects of osmotic perturbation. Biochimica et Biophysica Acta (BBA) - Biomembranes, 896(2):214–223, 1987.
- [10] Akihiko Irimajiri, Koji Asami, Takako Ichinowatari, and Yoshito Kinoshita. Passive electrical properties of the membrane and cytoplasm of cultured rat basophil leukemia cells. i. dielectric behavior of cell suspensions in 0.01-500 mhz and its simulation with a single-shell model. Biochimica et Biophysica Acta (BBA) - Biomembranes, 896(2):203–213, 1987.
- [11] K. Asami, Y. Takahashi, and S. Takashima. Dielectric properties of mouse lymphocytes and erythrocytes. Biochimica et Biophysica Acta (BBA) - Molecular Cell Research, 1010(1):49–55, 1989.
- [12] J. Gimsa, T. Muller, T. Schnelle, and G. Fuhr. Dielectric spectroscopy of single human erythrocytes at physiological ionic strength: dispersion of the cytoplasm. Biophysical Journal, 71(1):495–506, 1996.

- [13] Valerica Raicu, Georgeta Raicu, and Grigore Turcu. Dielectric properties of yeast cells as simulated by the two-shell model. Biochimica et Biophysica Acta (BBA) - Bioenergetics, 1274(3):143–148, 1996.
- [14] V. Raicu, T. Saibara, H. Enzan, and A. Irimajiri. Dielectric properties of rat liver in vivo: analysis by modeling hepatocytes in the tissue architecture. Bioelectrochemistry and Bioenergetics, 47(2):333–342, 1998.
- [15] Wei Bai, K. S. Zhao, and K. Asami. Dielectric properties of e. coli cell as simulated by the three-shell spheroidal model. Biophysical Chemistry, 122(2):136–142, 2006.
- [16] Wei Bai, Kongshuang Zhao, and Koji Asami. Effects of copper on dielectric properties of e. coli cells. Colloids and Surfaces B: Biointerfaces, 58(2):105–115, 2007.
- [17] Jutiporn Sudsiri, Derk Wachner, and Jan Gimsa. On the temperature dependence of the dielectric membrane properties of human red blood cells. Bioelectrochemistry, 70(1):134–140, 2007.
- [18] X. Ma, X. Du, N. Gholizadeh, V. Gholizadeh, H. Li, X. Cheng, and J. C. M. Hwang. One resistor and two capacitors: An electrical engineer’s simple view of a biological cell. In 2017 IEEE MTT-S International Microwave Workshop Series on Advanced Materials and Processes for RF and THz Applications (IMWS-AMP), pages 1–3. 2017 IEEE MTT-S International Microwave Workshop Series on Advanced Materials and Processes for RF and THz Applications (IMWS-AMP), 2017.
- [19] Amin Mansoorifar, Anil Koklu, Shihong Ma, Ganesh V. Raj, and Ali Beskok. Electrical impedance measurements of biological cells in response to external stimuli. Analytical Chemistry, 90(7):4320–4327, 2018.
- [20] W Jaroszynski, J Terlecki, and J Sulocki. Application of the modified pauly-schwan model to determine the passive electrical parameters of lymphocytes. Stud Biophys, 107(2):117–126, 1985.
- [21] Xun Hu, W. Michael Arnold, and Ulrich Zimmermann. Alterations in the electrical properties of t and b lymphocyte membranes induced by mitogenic stimulation. activation monitored by electro-rotation of single cells. Biochimica et Biophysica Acta (BBA) - Biomembranes, 1021(2):191–200, 1990.
- [22] Ralph Holzel and Ingolf Lamprecht. Dielectric properties of yeast cells as determined by electrorotation. Biochimica et Biophysica Acta (BBA) - Biomembranes, 1104(1):195–200, 1992.
- [23] F. Bordi, C. Cametti, A. Rosi, and A. Calcabrini. Frequency domain electrical conductivity measurements of the passive electrical properties of human lymphocytes. Biochimica et Biophysica Acta (BBA) - Biomembranes, 1153(1):77–88, 1993.
- [24] F F Becker, X B Wang, Y Huang, R Pethig, J Vykoukal, and P R Gascoyne. Separation of human breast cancer cells from blood by differential dielectric affinity. Proceedings

- of the National Academy of Sciences of the United States of America, 92(3):860–864, 1995. PMID: 7846067 PMCID: PMC42720.
- [25] Y. Huang, X. B. Wang, R. Holzel, F. F. Becker, and P. R. Gascoyne. Electrorotational studies of the cytoplasmic dielectric properties of friend murine erythroleukaemia cells. Physics in Medicine and Biology, 40(11):1789–1806, 1995. PMID: 8587932.
- [26] Yulia Plevaya, Irina Ermolina, Michael Schlesinger, Ben-Zion Ginzburg, and Yuri Feldman. Time domain dielectric spectroscopy study of human cells: Ii. normal and malignant white blood cells. Biochimica et Biophysica Acta (BBA) - Biomembranes, 1419(2):257–271, 1999.
- [27] S Kakorin and E Neumann. Ionic conductivity of electroporated lipid bilayer membranes. Bioelectrochemistry, 56(1):163–166, 2002.
- [28] Fatima H. Labeed, Helen M. Coley, and Michael P. Hughes. Differences in the biophysical properties of membrane and cytoplasm of apoptotic cells revealed using dielectrophoresis. Biochimica et Biophysica Acta (BBA) - General Subjects, 1760(6):922–929, 2006.
- [29] Song-I. Han, Young-Don Joo, and Ki-Ho Han. An electrorotation technique for measuring the dielectric properties of cells with simultaneous use of negative quadrupolar dielectrophoresis and electrorotation. Analyst, 138(5):1529–1537, 2013.
- [30] Clarissa Villinger, Martin Schauflinger, Heiko Gregorius, Christine Kranz, Katharina Höhn, Soufi Nafeey, and Paul Walther. Three-Dimensional Imaging of Adherent Cells using FIB/SEM and STEM, pages 617–638. Humana Press, Totowa, NJ, 2014.
- [31] R B Setlow, E Grist, K Thompson, and A D Woodhead. Wavelengths effective in induction of malignant melanoma. Proceedings of the National Academy of Sciences, 90(14):6666–6670, 1993.
- [32] Malgorzata Rozanowska, John Jarvis-Evans, Witold Korytowski, Mike E. Boulton, Janice M. Burke, and Tadeusz Sarna. Blue light-induced reactivity of retinal age pigment: In vitro generation of oxygen-reactive species. Journal of Biological Chemistry, 270(32):18825–18830, 1995.
- [33] Christopher D. Link, Virginia Fonte, Brian Hiester, John Yerg, Jmil Ferguson, Susan Csontos, Michael A. Silverman, and Gretchen H. Stein. Conversion of green fluorescent protein into a toxic, aggregation-prone protein by c-terminal addition of a short peptide. Journal of Biological Chemistry, 281(3):1808–1816, 2006.
- [34] Jorg Wiedenmann, Franz Oswald, and Gerd Ulrich Nienhaus. Fluorescent proteins for live cell imaging: Opportunities, limitations, and challenges. IUBMB Life, 61(11):1029–1042, 2009.
- [35] D Huang, EA Swanson, CP Lin, JS Schuman, WG Stinson, W Chang, MR Hee, T Flotte, K Gregory, CA Puliafito, and al. et. Optical coherence tomography. Science, 254(5035):1178–1181, 1991.

- [36] James Sharpe, Ulf Ahlgren, Paul Perry, Bill Hill, Allyson Ross, Jacob Hecksher-Sørensen, Richard Baldock, and Duncan Davidson. Optical projection tomography as a tool for 3d microscopy and gene expression studies. Science, 296(5567):541–545, 2002.
- [37] Erik M. Shapiro, Stanko Skrtic, Kathryn Sharer, Jonathan M. Hill, Cynthia E. Dunbar, and Alan P. Koretsky. Mri detection of single particles for cellular imaging. Proceedings of the National Academy of Sciences, 101(30):10901–10906, 2004.
- [38] Ivar Giaever and Charles R. Keese. A morphological biosensor for mammalian cells. Nature, 366(6455):591–592, 12 1993.
- [39] Charles R. Keese, Joachim Wegener, Sarah R. Walker, and Ivar Giaever. Electrical wound-healing assay for cells in vitro. Proceedings of the National Academy of Sciences, 101(6):1554–1559, 2004.
- [40] Pierre O. Bagnaninchi and Nicola Drummond. Real-time label-free monitoring of adipose-derived stem cell differentiation with electric cell-substrate impedance sensing. Proceedings of the National Academy of Sciences, 108(16):6462–6467, 2011.
- [41] R. P. Henderson and J. G. Webster. An impedance camera for spatially specific measurements of the thorax. IEEE Transactions on Biomedical Engineering, BME-25(3):250–254, 5 1978.
- [42] D C Barber and B H Brown. Applied potential tomography. Journal of Physics E: Scientific Instruments, 17(9):723–733, 9 1984.
- [43] F. Santosa and M. Vogelius. A backprojection algorithm for electrical impedance imaging. SIAM Journal on Applied Mathematics, 50(1):216–243, 1990.
- [44] M. Cheney, D. Isaacson, J. C. Newell, S. Simske, and J. Goble. Noser: An algorithm for solving the inverse conductivity problem. International Journal of Imaging Systems and Technology, 2(2):66–75, 1990.
- [45] R. V. Davalos, D. M. Otten, L. M. Mir, and B. Rubinsky. Electrical impedance tomography for imaging tissue electroporation. IEEE Transactions on Biomedical Engineering, 51(5):761–767, 5 2004.
- [46] P. Linderholm, L. Marescot, M. H. Loke, and P. Renaud. Cell culture imaging using microimpedance tomography. IEEE Transactions on Biomedical Engineering, 55(1):138–146, 1 2008.
- [47] Tao Sun, Soichiro Tsuda, Klaus-Peter Zauner, and Hywel Morgan. On-chip electrical impedance tomography for imaging biological cells. Biosensors and Bioelectronics, 25(5):1109–1115, 2010.
- [48] Sameera Dharia, Harold Ayliffe, and Richard Rabbitt. Single cell electric impedance topography: Mapping membrane capacitance. Lab on a chip, 9(23):3370–7, 12 2009.

- [49] Arie Meir and Boris Rubinsky. Electrical impedance tomographic imaging of a single cell electroporation. Biomedical Microdevices, 16(3):427–437, 6 2014.
- [50] Y. Yang, J. Jia, S. Smith, N. Jamil, W. Gamal, and P. Bagnaninchi. A miniature electrical impedance tomography sensor and 3-d image reconstruction for cell imaging. IEEE Sensors Journal, 17(2):514–523, 2017.
- [51] X. Liu, J. Yao, T. Zhao, H. Obara, Y. Cui, and M. Takei. Image reconstruction under contact impedance effect in micro electrical impedance tomography sensors. IEEE Transactions on Biomedical Circuits and Systems, 12(3):623–631, 2018.
- [52] C. Laborde, F. Pittino, H. A. Verhoeven, S. G. Lemay, L. Selmi, M. A. Jongsma, and F. P. Widdershoven. Real-time imaging of microparticles and living cells with CMOS nanocapacitor arrays. Nature Nanotechnology, 10(9):791–795, 9 2015.
- [53] V. Viswam, R. Bounik, A. Shadmani, J. Dragas, C. Urwyler, J. A. Boos, M. E. J. Obien, J. Muller, Y. Chen, and A. Hierlemann. Impedance spectroscopy and electrophysiological imaging of cells with a high-density cmos microelectrode array system. IEEE Transactions on Biomedical Circuits and Systems, 12(6):1356–1368, 2018.
- [54] H. Pauly, L. Packer, and H. P. Schwan. Electrical properties of mitochondrial membranes. The Journal of Biophysical and Biochemical Cytology, 7:589–601, 1960. PMID: 14431035 PMID: PMC2224892.
- [55] E. L. Carstensen, H. A. Cox, W. B. Mercer, and L. A. Natale. Passive electrical properties of microorganisms. Biophysical Journal, 5(3):289–300, 1965.
- [56] H. P. Schwan and K. Li. Capacity and conductivity of body tissues at ultrahigh frequencies. Proceedings of the IRE, 41(12):1735–1740, 1953.
- [57] Myo Thein, Fareid Asphahani, An Cheng, Ryan Buckmaster, Miqin Zhang, and Jian Xu. Response characteristics of single-cell impedance sensors employed with surface-modified microelectrodes. Biosensors and Bioelectronics, 25(8):1963–1969, 2010.
- [58] Thiruvallur R. Gowrishankar and James C. Weaver. An approach to electrical modeling of single and multiple cells. Proceedings of the National Academy of Sciences, 100(6):3203–3208, 2003. PMID: 12626744.
- [59] Dingkun Ren and Chi On Chui. Feasibility of tracking multiple single-cell properties with impedance spectroscopy. ACS Sensors, 3(5):1005–1015, 2018. PMID: 29737153.
- [60] Xiaoqiu Huang, Duc Nguyen, D. W. Greve, and M. M. Domach. Simulation of microelectrode impedance changes due to cell growth. IEEE Sensors Journal, 4(5):576–583, 2004.
- [61] A. Di Biasio and C. Cametti. Effect of shape on the dielectric properties of biological cell suspensions. Bioelectrochemistry, 71(2):149–156, 2007.

- [62] Ablaihan Akhazhanov and Chi On Chui. On modeling diversity in electrical cellular response: Data-driven approach. ACS Sensors, 4(9):2471–2480, 2019. PMID: 31385505.
- [63] A. Lucas, M. Iliadis, R. Molina, and A. K. Katsaggelos. Using deep neural networks for inverse problems in imaging: Beyond analytical methods. IEEE Signal Processing Magazine, 35(1):20–36, 2018.
- [64] Jong Chul Ye, Yoseob Han, and Eunju Cha. Deep convolutional framelets: A general deep learning framework for inverse problems. SIAM Journal on Imaging Sciences, 11(2):991–1048, 2018.
- [65] K. H. Jin, M. T. McCann, E. Froustey, and M. Unser. Deep convolutional neural network for inverse problems in imaging. IEEE Transactions on Image Processing, 26(9):4509–4522, 2017.
- [66] S. Wang, Z. Su, L. Ying, X. Peng, S. Zhu, F. Liang, D. Feng, and D. Liang. Accelerating magnetic resonance imaging via deep learning. In 2016 IEEE 13th International Symposium on Biomedical Imaging (ISBI), pages 514–517, 2016.
- [67] Yoseob Han, Jae Jun Yoo, and Jong Chul Ye. Deep residual learning for compressed sensing CT reconstruction via persistent homology analysis. CoRR, abs/1611.06391, 2016.
- [68] Hu Chen, Yi Zhang, Weihua Zhang, Peixi Liao, Ke Li, Jiliu Zhou, and Ge Wang. Low-dose ct via convolutional neural network. Biomed. Opt. Express, 8(2):679–694, 2017.
- [69] J. Zheng and L. Peng. An autoencoder-based image reconstruction for electrical capacitance tomography. IEEE Sensors Journal, 18(13):5464–5474, 2018.
- [70] Tomasz Rymarczyk, Grzegorz Klosowski, Edward Kozlowski, and Pawel Tchorzewski. Comparison of selected machine learning algorithms for industrial electrical tomography. Sensors, 19(7), 2019.
- [71] Yuwei Fan and Lexing Ying. Solving electrical impedance tomography with deep learning. Journal of Computational Physics, 404:109119, 2020.
- [72] S. J. Hamilton and A. Hauptmann. Deep d-bar: Real-time electrical impedance tomography imaging with deep neural networks. IEEE Transactions on Medical Imaging, 37(10):2367–2377, 2018.
- [73] Alison C. Cullen and H. Christopher Frey. Probabilistic Techniques in Exposure Assessment: A Handbook for Dealing with Variability and Uncertainty in Models and Inputs. Springer US, 1999. [Online; accessed 2018-09-26].
- [74] Tatiana Benaglia, Didier Chauveau, David R. Hunter, and Derek Young. mixtools: An r package for analyzing mixture models. Journal of Statistical Software, Articles, 32(6):1–29, 2009.

- [75] Robert Tibshirani, Guenther Walther, and Trevor Hastie. Estimating the number of clusters in a data set via the gap statistic. Journal of the Royal Statistical Society: Series B (Statistical Methodology), 63(2):411–423, 2001.
- [76] Aaron Clauset, Cosma Rohilla Shalizi, and M. E. J. Newman. Power-law distributions in empirical data. SIAM Review, 51(4):661–703, 2009. arXiv: 0706.1062.
- [77] M. Montal and P. Mueller. Formation of bimolecular membranes from lipid monolayers and a study of their electrical properties. Proceedings of the National Academy of Sciences, 69(12):3561–3566, 1972. PMID: 4509315.
- [78] H. P. Schwan. Electrical properties of tissues and cell suspensions: mechanisms and models. In Proceedings of 16th Annual International Conference of the IEEE Engineering in Medicine and Biology Society, pages A70–A71 vol.1. Proceedings of 16th Annual International Conference of the IEEE Engineering in Medicine and Biology Society, 1994.
- [79] Kenneth S. Cole. Membranes, Ions and Impulses: A Chapter of Classical Biophysics. University of California Press, 1968.
- [80] R D Stoy, K R Foster, and H P Schwan. Dielectric properties of mammalian tissues from 0.1 to 100 mhz; a summary of recent data. Physics in Medicine and Biology, 27(4):501–513, 4 1982.
- [81] W. Kuang and S. O. Nelson. Research paper insights: Low-frequency dielectric properties of biological tissues: A review with some new insights. ResearchGate, 1998. [Online; accessed 2017-04-10].
- [82] M Schaefer, W Gross, J Ackemann, and M. M Gebhard. The complex dielectric spectrum of heart tissue during ischemia. Bioelectrochemistry, 58(2):171–180, 2002.
- [83] Koji Asami. Dielectric dispersion in biological cells of complex geometry simulated by the three-dimensional finite difference method. Journal of Physics D: Applied Physics, 39(3):492–499, 1 2006.
- [84] Koji Asami. Effects of membrane disruption on dielectric properties of biological cells. Journal of Physics D: Applied Physics, 39(21):4656–4663, 10 2006.
- [85] Koji Asami. Dielectric properties of microvillous cells simulated by the three-dimensional finite-element method. Bioelectrochemistry, 81(1):28–33, 2011.
- [86] Elham Salimi. Nanosecond Pulse Electroporation of Biological Cells: The Effect of Membrane Dielectric Relaxation. PhD thesis, University of Manitoba (Canada), Canada, 2011. [Online; accessed 2017-04-10].
- [87] E. Salimi, D. J. Thomson, and G. E. Bridges. Membrane dielectric dispersion in nanosecond pulsed electroporation of biological cells. IEEE Transactions on Dielectrics and Electrical Insulation, 20(4):1256–1265, 2013.

- [88] Damien Cuvelier, Manuel Thery, Yeh-Shiu Chu, Sylvie Dufour, Jean-Paul Thiery, Michel Bornens, Pierre Nassoy, and L. Mahadevan. The universal dynamics of cell spreading. Current Biology, 17(8):694–699, 2007.
- [89] Hans-Günther Döbereiner, Benjamin Dubin-Thaler, Grégory Giannone, Harry S. Xenias, and Michael P. Sheetz. Dynamic phase transitions in cell spreading. Phys. Rev. Lett., 93:108105–1 – 108105–4, 9 2004.
- [90] E. Sackmann, E. Bausch, and L. Vonna. Physics of composite cell membrane and actin based cytoskeleton. In F. Flyvbjerg, F. Julicher, P. Ormos, and F. David, editors, Physics of bio-molecules and cells. Physique des biomolécules et des cellules, pages 237–284, Berlin, Heidelberg, 2002. Springer Berlin Heidelberg.
- [91] G. A. Dunn, D. Zicha, and P. E. Fraylich. Rapid, microtubule-dependent fluctuations of the cell margin. Journal of Cell Science, 110 (Pt 24):3091–3098, 1997. PMID: 9365279.
- [92] Benjamin J. Dubin-Thaler, Gregory Giannone, Hans-Gunther Döbereiner, and Michael P. Sheetz. Nanometer analysis of cell spreading on matrix-coated surfaces reveals two distinct cell states and steps. Biophysical Journal, 86(3):1794–1806, 2004.
- [93] S. J. Singer and Garth L. Nicolson. The fluid mosaic model of the structure of cell membranes. Science, 175(4023):720–731, 1972. PMID: 4333397.
- [94] Z. C. Tu and Z. C. Ou-Yang. Geometric theory on the elasticity of bio-membranes. Journal of Physics A: Mathematical and General, 37(47):11407–11429, 2004. arXiv: cond-mat/0403309.
- [95] Z. C. Tu and Z. C. Ou-Yang. Elastic theory of low-dimensional continua and its applications in bio- and nano-structures. arXiv:0706.0001 [cond-mat, physics:math-ph, physics:physics, q-bio], 2007. arXiv: 0706.0001.
- [96] Erich Sackmann and Robijn F. Bruinsma. Cell adhesion as wetting transition? ChemPhysChem, 3(3):262–269, 2002.
- [97] Antonio Mendez-Vilas, Ana Belen Jodar-Reyes, and Maria Luisa Gonzalez-Martin. Ultrasmall liquid droplets on solid surfaces: Production, imaging, and relevance for current wetting research. Small, 5(12):1366–1390, 2009.
- [98] Allen J. Bard and Larry R. Faulkner. Electrochemical Methods: Fundamentals and Applications. New York: John Wiley & Sons, Inc., 2nd edition, 2000.
- [99] Erkki Somersalo, Margaret Cheney, and David Isaacson. Existence and uniqueness for electrode models for electric current computed tomography. SIAM Journal on Applied Mathematics, 52(4):1023–1040, 1992.
- [100] Jan Sikora, SR Arridge, Richard Bayford, and Lior Horesh. The application of hybrid bem/fem methods to solve electrical impedance tomography’s forward problem for the human head. In XII ICEBI & V EIT Conference., Gdansk. ed, 01 2004.

- [101] Peter P. Silvester and Ronald L. Ferrari. Finite Elements for Electrical Engineers. Cambridge University Press, 3 edition, 1996.
- [102] M. Tarvainen, M. Vauhkonen, T. Savolainen, and J.P. Kaipio. Boundary element method and internal electrodes in electrical impedance tomography. International Journal for Numerical Methods in Engineering, 50(4):809–824, 2001.
- [103] John T. Katsikadelis. The Boundary Element Method for Engineers and Scientists (Second Edition). Academic Press, 2 edition, 2016.
- [104] K. W. Morton and D. F. Mayers. Numerical Solution of Partial Differential Equations: An Introduction. Cambridge University Press, 2 edition, 2005.
- [105] R V Kohn and A McKenney. Numerical implementation of a variational method for electrical impedance tomography. Inverse Problems, 6(3):389–414, 6 1990.
- [106] T. J. Yorkey, J. G. Webster, and W. J. Tompkins. Comparing reconstruction algorithms for electrical impedance tomography. IEEE Transactions on Biomedical Engineering, BME-34(11):843–852, 11 1987.
- [107] A. Adler and R. Guardo. Electrical impedance tomography: regularized imaging and contrast detection. IEEE Transactions on Medical Imaging, 15(2):170–179, 4 1996.
- [108] M. Vauhkonen, D. Vadasz, P. A. Karjalainen, E. Somersalo, and J. P. Kaipio. Tikhonov regularization and prior information in electrical impedance tomography. IEEE Transactions on Medical Imaging, 17(2):285–293, 4 1998.
- [109] D C Dobson and F Santosa. An image-enhancement technique for electrical impedance tomography. Inverse Problems, 10(2):317–334, 4 1994.
- [110] Andrea Borsic, Brad M Graham, Andy Adler, and William RB Lionheart. Total variation regularization in electrical impedance tomography. MIMS Preprint, 6 2007.
- [111] M. Vauhkonen, P. A. Karjalainen, and J. P. Kaipio. A kalman filter approach to track fast impedance changes in electrical impedance tomography. IEEE Transactions on Biomedical Engineering, 45(4):486–493, 4 1998.
- [112] Erkki Somersalo, Jari P. Kaipio, Marko J. Vauhkonen, D. Baroudi, and S. Jaer-venpaeae. Impedance imaging and markov chain monte carlo methods. In Randall Locke Barbour, Mark J. Carvlin, and Michael A. Fiddy, editors, Computational, Experimental, and Numerical Methods for Solving Ill-Posed Inverse Imaging Problems: Medical and Nonmedical Applications, volume 3171, pages 175 – 185. International Society for Optics and Photonics, SPIE, 1997.
- [113] Jari P Kaipio, Ville Kolehmainen, Erkki Somersalo, and Marko Vauhkonen. Statistical inversion and monte carlo sampling methods in electrical impedance tomography. Inverse Problems, 16(5):1487–1522, 10 2000.

- [114] J. L. Mueller, S. Siltanen, and D. Isaacson. A direct reconstruction algorithm for electrical impedance tomography. IEEE Transactions on Medical Imaging, 21(6):555–559, 6 2002.
- [115] D. Isaacson, J. L. Mueller, J. C. Newell, and S. Siltanen. Reconstructions of chest phantoms by the d-bar method for electrical impedance tomography. IEEE Transactions on Medical Imaging, 23(7):821–828, 7 2004.
- [116] David Holder. Electrical Impedance Tomography : Methods, History and Applications. CRC Press, 12 2004.
- [117] Tom Tidswell, Adam Gibson, Richard H. Bayford, and David S. Holder. Three-dimensional electrical impedance tomography of human brain activity. NeuroImage, 13(2):283–294, 2001.
- [118] M. Cheney, D. Isaacson, and J. Newell. Electrical impedance tomography. SIAM Review, 41(1):85–101, 1999.
- [119] Liliana Borcea. Electrical impedance tomography. Inverse Problems, 18(6):R99–R136, 10 2002.
- [120] BH Brown. Electrical impedance tomography (eit): a review. Journal of Medical Engineering & Technology, 27(3):97–108, 2003.
- [121] Jean Roche and Jan Sokolowski. Numerical methods for shape identification problems. Control and Cybernetics, 25, 1 1996.
- [122] A Carpio and M-L Rapún. Hybrid topological derivative and gradient-based methods for electrical impedance tomography. Inverse Problems, 28(9):095010, 8 2012.
- [123] M. Hintermuller, A. Laurain, and A. A. Novotny. Second-order topological expansion for electrical impedance tomography. Advances in Computational Mathematics, 6(2):235–265, 2 2012.
- [124] A. D. Ferreira, A. A. Novotny, and J. Sokolowski. Topological derivative method for electrical impedance tomography problems. Informatyka, Automatyka, Pomiar w Gospodarce i Ochronie Srodowiska, 2:4–8, 2016.
- [125] Eric T. Chung, Tony F. Chan, and Xue-Cheng Tai. Electrical impedance tomography using level set representation and total variational regularization. Journal of Computational Physics, 205(1):357–372, 2005.
- [126] Michael Hintermuller and Antoine Laurain. Electrical impedance tomography: from topology to shape. Control and Cybernetics, 37(4):913–933, 2008.
- [127] Karsten Eppler and Helmut Harbrecht. A regularized newton method in electrical impedance tomography using shape hessian information. Control and Cybernetics, 34(1):203–225, 2005.

- [128] L. Afraites, M. Dambrine, and D. Kateb. On second order shape optimization methods for electrical impedance tomography. SIAM Journal on Control and Optimization, 47(3):1556–1590, 2008.
- [129] David R Hunter and Kenneth Lange. A tutorial on mm algorithms. The American Statistician, 58(1):30–37, 2004.
- [130] A D Seagar, D C Barber, and B H Brown. Theoretical limits to sensitivity and resolution in impedance imaging. Clinical Physics and Physiological Measurement, 8(4A):13–31, 11 1987.
- [131] L M Heikkinen, M Vauhkonen, T Savolainen, and J P Kaipio. Modelling of internal structures and electrodes in electrical process tomography. Measurement Science and Technology, 12(8):1012–1019, 7 2001.
- [132] Michael Lukaschewitsch, Peter Maass, and Michael Pidcock. Tikhonov regularization for electrical impedance tomography on unbounded domains. Inverse Problems, 19(3):585–610, 4 2003.
- [133] Zhou Wang, A. C. Bovik, H. R. Sheikh, and E. P. Simoncelli. Image quality assessment: from error visibility to structural similarity. IEEE Transactions on Image Processing, 13(4):600–612, 2004.
- [134] Vidya Sarode, Sneha Patkar, and Alice N Cheeran. Comparison of 2-d algorithms in elt based image reconstruction. International Journal of Computer Applications, 69(8), 2013.
- [135] M Vauhkonen, W R B Lionheart, L M Heikkinen, P J Vauhkonen, and J P Kaipio. A MATLAB package for the EIDORS project to reconstruct two-dimensional EIT images. Physiological Measurement, 22(1):107–111, 2 2001.
- [136] Andy Adler and William R B Lionheart. Uses and abuses of EIDORS: an extensible software base for EIT. Physiological Measurement, 27(5):S25–S42, 4 2006.
- [137] Yann LeCun, Yoshua Bengio, and Geoffrey Hinton. Deep learning. Nature, 521(7553):436–444, 5 2015.
- [138] G. Wang. A perspective on deep imaging. IEEE Access, 4:8914–8924, 2016.
- [139] Trevor Hastie, Robert Tibshirani, and Jerome Friedman. The Elements of Statistical Learning. Springer International Publishing, 2 edition, 2016.
- [140] Ian Goodfellow, Yoshua Bengio, and Aaron Courville. Deep Learning. MIT Press, 2016.
- [141] Victor Isakov. Inverse Problems for Partial Differential Equations. Springer International Publishing, 3 edition, 2017.

- [142] Diederik P. Kingma and Jimmy Ba. Adam: A method for stochastic optimization. In Yoshua Bengio and Yann LeCun, editors, 3rd International Conference on Learning Representations, ICLR 2015, San Diego, CA, USA, May 7-9, 2015, Conference Track Proceedings, 2015.
- [143] Nitish Srivastava, Geoffrey Hinton, Alex Krizhevsky, Ilya Sutskever, and Ruslan Salakhutdinov. Dropout: A simple way to prevent neural networks from overfitting. Journal of Machine Learning Research, 15(56):1929–1958, 2014.
- [144] Sergey Ioffe and Christian Szegedy. Batch normalization: Accelerating deep network training by reducing internal covariate shift. In Proceedings of the 32nd International Conference on International Conference on Machine Learning - Volume 37, ICML 15, pages 448–456. JMLR.org, 2015.
- [145] Jimmy Lei Ba, Jamie Ryan Kiros, and Geoffrey E Hinton. Layer normalization. arXiv preprint arXiv:1607.06450, 2016.
- [146] Mingxing Tan and Quoc V. Le. Efficientnet: Rethinking model scaling for convolutional neural networks. In Kamalika Chaudhuri and Ruslan Salakhutdinov, editors, Proceedings of the 36th International Conference on Machine Learning, ICML 2019, 9-15 June 2019, Long Beach, California, USA, volume 97 of Proceedings of Machine Learning Research, pages 6105–6114. PMLR, 2019.
- [147] C. Szegedy, Wei Liu, Yangqing Jia, P. Sermanet, S. Reed, D. Anguelov, D. Erhan, V. Vanhoucke, and A. Rabinovich. Going deeper with convolutions. In 2015 IEEE Conference on Computer Vision and Pattern Recognition (CVPR), pages 1–9, 2015.
- [148] Christian Szegedy, Sergey Ioffe, Vincent Vanhoucke, and Alexander A. Alemi. Inception-v4, inception-resnet and the impact of residual connections on learning. In Proceedings of the Thirty-First AAAI Conference on Artificial Intelligence, AAAI 17, pages 4278–4284. AAAI Press, 2017.
- [149] Kaiming He, Xiangyu Zhang, Shaoqing Ren, and Jian Sun. Deep residual learning for image recognition. In The IEEE Conference on Computer Vision and Pattern Recognition (CVPR), 6 2016.
- [150] G. Huang, Z. Liu, L. Van Der Maaten, and K. Q. Weinberger. Densely connected convolutional networks. In 2017 IEEE Conference on Computer Vision and Pattern Recognition (CVPR), pages 2261–2269, 2017.
- [151] Olaf Ronneberger, Philipp Fischer, and Thomas Brox. U-net: Convolutional networks for biomedical image segmentation. In Nassir Navab, Joachim Hornegger, William M. Wells, and Alejandro F. Frangi, editors, Medical Image Computing and Computer-Assisted Intervention – MICCAI 2015, pages 234–241, Cham, 2015. Springer International Publishing.
- [152] Ian Goodfellow, Jean Pouget-Abadie, Mehdi Mirza, Bing Xu, David Warde-Farley, Sherjil Ozair, Aaron Courville, and Yoshua Bengio. Generative adversarial nets. In

- Z. Ghahramani, M. Welling, C. Cortes, N. D. Lawrence, and K. Q. Weinberger, editors, Advances in Neural Information Processing Systems 27, pages 2672–2680. Curran Associates, Inc., 2014.
- [153] Thomas N. Kipf and Max Welling. Semi-supervised classification with graph convolutional networks. In 5th International Conference on Learning Representations, ICLR 2017, Toulon, France, April 24-26, 2017, Conference Track Proceedings. OpenReview.net, 2017.
- [154] Federico Monti, Davide Boscaini, Jonathan Masci, Emanuele Rodolà, Jan Svoboda, and Michael M. Bronstein. Geometric deep learning on graphs and manifolds using mixture model cnns. In 2017 IEEE Conference on Computer Vision and Pattern Recognition, CVPR 2017, Honolulu, HI, USA, July 21-26, 2017, pages 5425–5434. IEEE Computer Society, 2017.
- [155] Yutong Feng, Yifan Feng, Haoxuan You, Xibin Zhao, and Yue Gao. Meshnet: Mesh neural network for 3d shape representation. In The Thirty-Third AAAI Conference on Artificial Intelligence, AAAI 2019, The Thirty-First Innovative Applications of Artificial Intelligence Conference, IAAI 2019, The Ninth AAAI Symposium on Educational Advances in Artificial Intelligence, EAAI 2019, Honolulu, Hawaii, USA, January 27 - February 1, 2019, pages 8279–8286. AAAI Press, 2019.
- [156] Brendan Kelly, Thomas P. Matthews, and Mark A. Anastasio. Deep learning-guided image reconstruction from incomplete data. CoRR, abs/1709.00584, 2017.
- [157] Andreas Kofler, Markus Haltmeier, Christoph Kolbitsch, Marc Kachelrieß, and Marc Dewey. A u-nets cascade for sparse view computed tomography. In Florian Knoll, Andreas Maier, and Daniel Rueckert, editors, Machine Learning for Medical Image Reconstruction, pages 91–99. Springer International Publishing, 2018.
- [158] J. Schlemper, J. Caballero, J. V. Hajnal, A. N. Price, and D. Rueckert. A deep cascade of convolutional neural networks for dynamic mr image reconstruction. IEEE Transactions on Medical Imaging, 37(2):491–503, 2018.
- [159] Neda Davoudi, Xose Luis Dean-Ben, and Daniel Razansky. Deep learning optoacoustic tomography with sparse data. Nature Machine Intelligence, 1(10):453–460, 10 2019.
- [160] Jonas Adler and Ozan Oktun. Solving ill-posed inverse problems using iterative deep neural networks. Inverse Problems, 33(12):124007, 11 2017.
- [161] H. K. Aggarwal, M. P. Mani, and M. Jacob. Modl: Model-based deep learning architecture for inverse problems. IEEE Transactions on Medical Imaging, 38(2):394–405, 2019.
- [162] J. H. R. Chang, C. Li, B. Póczos, B. V. K. Vijaya Kumar, and A. C. Sankaranarayanan. One network to solve them all - solving linear inverse problems using deep projection models. In 2017 IEEE International Conference on Computer Vision (ICCV), pages 5889–5898, 2017.

- [163] Kerstin Hammernik, Teresa Klatzer, Erich Kobler, Michael P. Recht, Daniel K. Sodickson, Thomas Pock, and Florian Knoll. Learning a variational network for reconstruction of accelerated mri data. Magnetic Resonance in Medicine, 79(6):3055–3071, 2018.
- [164] S. Zhang and E. Salari. Image denoising using a neural network based non-linear filter in wavelet domain. In Proceedings. (ICASSP '05). IEEE International Conference on Acoustics, Speech, and Signal Processing, 2005., volume 2, pages ii/989–ii/992 Vol. 2, 2005.
- [165] H. C. Burger, C. J. Schuler, and S. Harmeling. Image denoising: Can plain neural networks compete with bm3d? In 2012 IEEE Conference on Computer Vision and Pattern Recognition, pages 2392–2399, 2012.
- [166] Lynton Ardizzone, Jakob Kruse, Carsten Rother, and Ullrich Kothe. Analyzing inverse problems with invertible neural networks. In International Conference on Learning Representations, 2019.
- [167] Yaniv Romano, Michael Elad, and Peyman Milanfar. The little engine that could: Regularization by denoising (red). SIAM Journal on Imaging Sciences, 10(4):1804–1844, 2017.
- [168] Housen Li, Johannes Schwab, Stephan Antholzer, and Markus Haltmeier. Nett: Solving inverse problems with deep neural networks. Inverse Problems, 2020.
- [169] Sebastian Lunz, Ozan Öktem, and Carola-Bibiane Schönlieb. Adversarial regularizers in inverse problems. In Proceedings of the 32nd International Conference on Neural Information Processing Systems, NIPS'18, pages 8516–8525, Red Hook, NY, USA, 2018. Curran Associates Inc.
- [170] Z. Wei, D. Liu, and X. Chen. Dominant-current deep learning scheme for electrical impedance tomography. IEEE Transactions on Biomedical Engineering, 66(9):2546–2555, 2019.
- [171] S. Liu, H. Wu, Y. Huang, Y. Yang, and J. Jia. Accelerated structure-aware sparse bayesian learning for three-dimensional electrical impedance tomography. IEEE Transactions on Industrial Informatics, 15(9):5033–5041, 2019.